

# Quantification tools in Structural Geology, based in field examples from Namibia.

Dissertation zur Erlangung des Grades  
“Doktor der Naturwissenschaften”

am Fachbereich Chemie, Pharmazie und Geowissenschaften  
der Johannes Gutenberg-Universität Mainz

Sara Simões dos Santos Coelho  
geboren in Lissabon

Mainz, Mai 2007

## Erklärung

Ich versichere hiermit, die vorliegende Arbeit selbständig und nur unter Verwendung der angegebenen Quellen und Hilfsmittel verfasst zu haben.

Mainz, Mai 2007

# Abstract

Chapter I presents a system for description of flanking structures, based on geometric parameters and independent of kinematic frame. The description can be made using two levels of accuracy. A qualitative method is described using four geometric features: tilt, slip, lift and roll. The method is suggested for practical use in the field, since it does not involve measurements or complicated procedures. In parallel, a quantitative approach is also presented, based on analytical modelling of Bézier curves. The method requires measurement of geometric features and involves mathematical treatment, but allows comparison between different flanking structures.

Chapter II studies two types of asymmetric quartz veins occurring in wall rocks of a crustal scale sinistral ductile shear zone in Namibia, the Purros Mylonite Zone. Bedding surfaces contain sigmoidal quartz veins with limited thickness along their symmetry axes that can be classified as tension gashes. A second type of veins consists of a striated central fault vein separating pennant-type quartz filled terminations. The tips of these “pennant veins” have a different orientation to those of the tension gashes. Analogue experiments were carried out using a sheet of silicone powder suspended on a slab of poly-dimethyl-siloxane (PDMS), both deformed in simple shear. These experiments produced open fractures very similar to the pennant veins that form by intersection of R and R' Riedel shear fractures. These fractures rotate and slip during progressive deformation, opening pennant shaped gaps. The natural pennant veins are interpreted to form by the same mechanism of R and R' shear fracture initiation, and subsequent rotation and opening. Since this mechanism differs from that of previously described vein types such as wing cracks, tension gashes and swordtail or fishmouth termination veins, which mainly open as tension veins, pennant veins are a new independent class of asymmetric mineral-filled veins.

Chapter III introduces Mohr-cyclides: the graphical representation of second-rank tensors in three-dimensional Mohr-space. Mohr-cyclides are also the 3D equivalent of the popular Mohr-circles. The concept is discussed for three tensors used frequently in Structural Geology: Stress, Flow and Deformation. This chapter also includes the definition of Mohr-cyclides for unspecified tensors and a proof that these surfaces can indeed be interpreted as Mohr-diagrams.

## Zusammenfassung

In Kapitel I wird eine Methodik zur Beschreibung von Flanking Structures beschrieben, basierend auf gegebenen geometrischen Parametern und unabhängig von der Kinematik. Die Beschreibung involviert zwei unterschiedlich akkurate Herangehensweisen: Eine qualitative Methode involviert die Parameter tilt, lift, slip und roll. Dieser Ansatz zielt auf den praktischen Einsatz während der Feldarbeit ab, da es ohne Messungen und komplizierte Verfahren auskommt. Parallel dazu wird ein quantitativer Ansatz vorgestellt, der auf der analytischen Modellierung von Bezierkurven basiert. Diese Methodik involviert die Messung geometrischer Eigenschaften und verlangt mathematische Behandlung, erlaubt aber den Vergleich verschiedener Flanking Structures.

Kapitel II befasst sich mit zwei Arten asymmetrischer Quarz-Adern, die im Nebengestein einer sinistralen duktilen Scherzone in krustalen Maßstab in Namibia, der Purros Mylonite Zone, auftreten. Schichtoberflächen enthalten sigmodale Quarz-Adern mit geringer Mächtigkeit entlang ihrer Symmetrieachsen, die als tension gashes klassifiziert werden können. Ein weiterer Typ Ader besteht aus Quarzadern mit pennant-förmigen Enden. Die Enden dieser pennant veins sind anders orientiert als die tension gashes. Es wurden Analog-Experimenten durchgeführt, bei denen Silikonpulver auf einer Polydimethylsiloxan (PDMS) Platte aufgetragen wurde, und in einfacher Scherung deformiert wurde. Das Resultat dieser Experimente waren Brüche, die den pennant veins ähneln, welche sich im Schnittpunkt von  $R$  und  $R'$  Riedel-Scherflächen bilden. Diese Brüche rotieren und gleiten während der progressiven Deformation, wodurch sich pennant-artige Klüfte bilden. Natürliche pennant veins werden daher durch einen identischen Mechanismus erklärt: durch initiale  $R$  und  $R'$  Scherbruch-Bildung anderer Ader-Typen, wie z.B. wing cracks, tension gashes, und swordtail oder fishmouth terminierte Adern, welche sich in erster Linie durch Extension bilden, unterscheidet, sind "pennant veins" eine neue Klasse asymmetrischer Mineraladern.

Kapitel III befasst sich mit der graphischen Darstellung von Tensoren zweite Stufe im dreidimensionalen Mohr-Raum, den Mohr-Zykliden. Insbesondere sind Mohr-Zyklide das räumliche Äquivalent des bekannten Mohr-Kreises. Das Konzept wird anhand dreier Arten von Tensoren diskutiert, die eine wichtige Rolle innerhalb der Strukturgeologie spielen: Spannung, Fluss und Verformung. Des Weiteren enthält das Kapitel die Definition von Mohr-Zykliden für beliebige Tensoren zweiter Stufe sowie einen Beweis, dass diese Zyklidoberflächen tatsächlich als Mohr-Diagramme interpretiert werden können.

## Preface

The motivation for my PhD dissertation was to study structures associated with the Puros Shear Zone (PSZ), a part of the Kaoko Belt of Namibia. The PSZ is a large, subvertical, crustal scale shear zone, which spans for over 400 km, from the border with Angola to the southern region of the Ugab Valley. Due to the very dry climate along the West coast of Namibia, exposure is very high and the quality of the outcrops allows continuous structural work over large areas. In the last few years, I did several seasons of field work, which included regional geology and mesoscopic scale structural analysis. The regional geology parts will be published at a later stage in co-authorship with the Mainz and Rio de Janeiro research groups on Namibia geology. This PhD dissertation focuses in the small scale structures, namely flanking structures in the House of the German (HoG) Limestone near Twyfelfontein and the quartz veins of the Central Kaoko Zone (CKZ) of the Orupembe region in the North.

The idea for the first chapter formed when I was confronted with multiple geometries of flanking folds in the HoG Limestone and realised that there was no classification system available that would encompass all of the observed structures. I then worked out a geometric classification for flanking structures, based on qualitative and quantitative parameters, which can be used for comparison and analysis of all types of flanking structures. This work is presented in Chapter I.

During a mapping season in Orupembe, I noticed two families of quartz veins coexisting in the foliation surface of a metasedimentary unit in the CKZ. The first type of veins could be described as classical tension gash geometry. The second type of quartz veins had a distinct shape, which could not be assigned to any of the published vein geometries. I called them pennant-veins, due to their characteristic triangular shape. Moreover, the peculiar structural setting of both families in the foliation plane, not normal to it, was puzzling. To explain these problems I set up a series of analogue experiments using PDMS and silica powder. The results were very enlightening and allowed me to conclude that pennant-vein development was controlled by the Riedel - Anti-riedel fracture system. This work is presented in Chapter II.

Throughout the pennant-vein work, I read papers about fractures and opening of veins which made extensive use of Mohr-circles. I then noticed that all of these graphical representations were two-dimensional and began wondering if it would be possible to devise a Mohr-diagram in three-dimensional space. After some (in fact, quite a lot of) work, I found a three-dimensional construction with all the

properties of a Mohr-diagram. The 3D graphs turned out to be members of the cyclide family, first described by Dupin in the early nineteenth century. I called them Mohr-cyclides, after the German engineer Otto Mohr, and presented them in Chapter III.

This PhD comprises three very different topics and there is more work behind this dissertation than is published here. However, I decided to present as a thesis only what was really my own work and ideas.

## Published Parts

**Chapter I** : Coelho, S., Passchier, C.W., Grasemann, B., 2005. Geometric description of flanking structures. *Journal of Structural Geology* 27, 597–606

**Chapter II** : Coelho, S., Passchier, C.W., Marques, F.O., 2006. Riedel-shear control on the development of pennant-veins: field example and analogue modelling. *Journal of Structural Geology* 28, 1658-1669.

Chapter III will be submitted as two separate papers in the near future.

# Chapter I - Geometric description of flanking structures.

## *1. Introduction*

Since the beginning of underground mining, people have felt the need to classify geological structures such as faults according to orientation and displacement direction (e.g. Playfair, 1802). At first sight, the geometry of faults crosscutting layering in rocks seemed to be simple enough to warrant further thought. Empirical experience set up a simple scheme of normal faults, which were the most common in mining areas set in extensional basins, and reverse (or thrust) faults. Further detail was added by Suess (1885) and de Magerie and Heim (1888) who introduced the concept of fault drag, the deflection of layers in the vicinity of the fault. Later, fault drag was subdivided in normal and reverse by the work of Hamblin (1965). In combination with the terms footwall and hanging wall, the system seems unambiguous. However, in the sedimentary basins where this fault nomenclature was mainly defined, fault drag usually involves little deflection of layering or foliation towards the faults. In metamorphic, highly deformed rocks, or in more complex systems of faults, geometries produced by fault drag can be more complex. A simple example can describe the kind of ambiguity that can arise in certain cases. The structure depicted in Fig.1 can be described both as a normal fault or a thrust in the existing classification. An observer on the scale of the smaller box observes a displacement in the marker typical of normal faults. If the structure is observed only in the far-field (bigger box) one might interpret it as a thrust. This example shows the need of describing accurately the fabric of fault drag in order to make correct interpretations.

Passchier (2001) and Grasemann and Stüwe (2001) expanded the concept of fault drag and defined flanking structures, developed where a host element (HE) is deflected in the vicinity of a cross-cutting element CE (Fig.2). The host element is a planar feature in the fabric of the rock, either bedding, a metamorphic foliation or a compositional layering. The cross-cutting element is the central part of the flanking structure and can be a fault, a joint, a filled vein, a patch of melt or even a rigid object in the rock (such as a mineral or a boudin) (Passchier, 2001). Flanking structures were initially envisaged as sub-meter scale structures, but geometrically they can include features such as fault drag, fault bend folds, and any fold developed around an object in a matrix, such as metadolerite dykes (Gayer et al., 1978) and crevasses in ice (Hudleston, 1989). The concept can also include folds developed due to rotation of a rigid object in a matrix, such as the drag folds modelled and described analytically by Ghosh (1975).

Grasemann and Stüwe (2001) and Grasemann et al. (2003) investigated the development of flanking structures adjacent to a cross cutting element, by simulation of flow around a slip surface in a viscous medium under general shear, by means of finite element modelling. Part of this work was a first attempt to classify flanking structures in three main categories: a-, s- and n-type flanking structures, which can be subdivided in 11 sub-types named A-K (cf. Passchier, 2001; Grasemann et al., 2003).

Although this genetic classification, which presumes a known kinematic frame, has been used in forward modelling studies (Exner et al., 2004.; Wiesmayr & Grasemann, 2005), field studies have shown that this geometric classification is imprecise and ambiguous when describing natural flanking folds.

Here, a non-genetic uniform classification system for all types of flanking structures is proposed, based solely on geometric criteria in order to avoid up-stream interpretation errors. This can be done with two levels of accuracy. A qualitative method is proposed as a descriptive tool to use in the field, while a quantitative method, based on analytical modelling, is also introduced where greater accuracy is needed, such as for comparison of flanking structures.

## 2. Qualitative classification

The geometry of faults, objects or veins and associated flanking structures can be described by a host element HE and a cross-cutting element CE (Fig.2). The HE can be subdivided into an external unfolded part, parallel on both sides of the CE (far-field component), and an internal part where the HE can be folded in a complex way. Here we restrict ourselves to simple fold geometries, which are enough to fully describe and classify most flanking structures.

A flanking structure, on one side of the CE, can be described using four parameters, defined according to the geometric relations between the HE and the CE, in a fixed reference frame (Fig.3). The origin of a Cartesian coordinate system is set at the intersection of the CE and HE. The x-axis is oriented

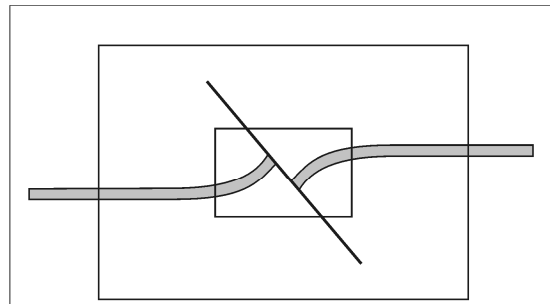


Fig. 1 - Ambiguity of fault nomenclature. Considering the arrangement of layering (bigger box), the structure may be classified as a thrust. However, considering the displacement close to the fault (small box), the structure would be interpreted as a normal fault.

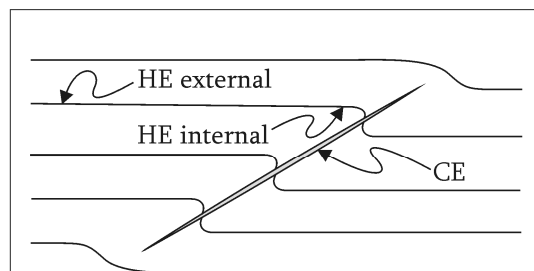


Fig. 2 - Schematic flanking structure. HE - host element; external, far-field component, unaffected by flanking structure; internal, part of the host element folded by the flanking structure. CE - cross cutting element.

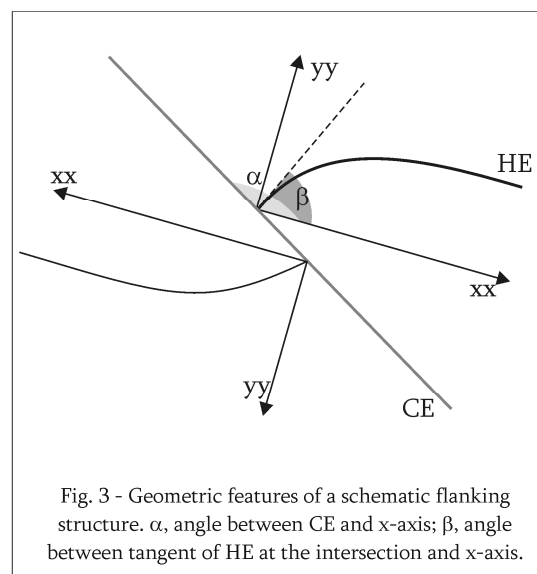
to be parallel with the far-field HE, with its positive half according to the dip of CE. In the following, hanging wall positions above the CE are described, although the method equally applies to flanking structures in the footwall. In strike slip, this corresponds to the wall away from the observer. This means that the positive y-axis is always in the same block as the positive x-axis. Notice that by defining the origin in the HE-CE intersection, only the geometry of one side of the CE is described, and that two separate coordinate systems have to be drawn for each side of the CE. This may seem an unnecessary complication but is useful, since flanking folds in the same layer commonly have a different shape on both sides of the CE.

The four different parameters, describing a flanking structure, are defined according to the geometric relations between the host element HE with the cross cutting element CE represented in Fig.2. These parameters are tilt, slip, lift and roll, explained in Figs. 4 and 5.

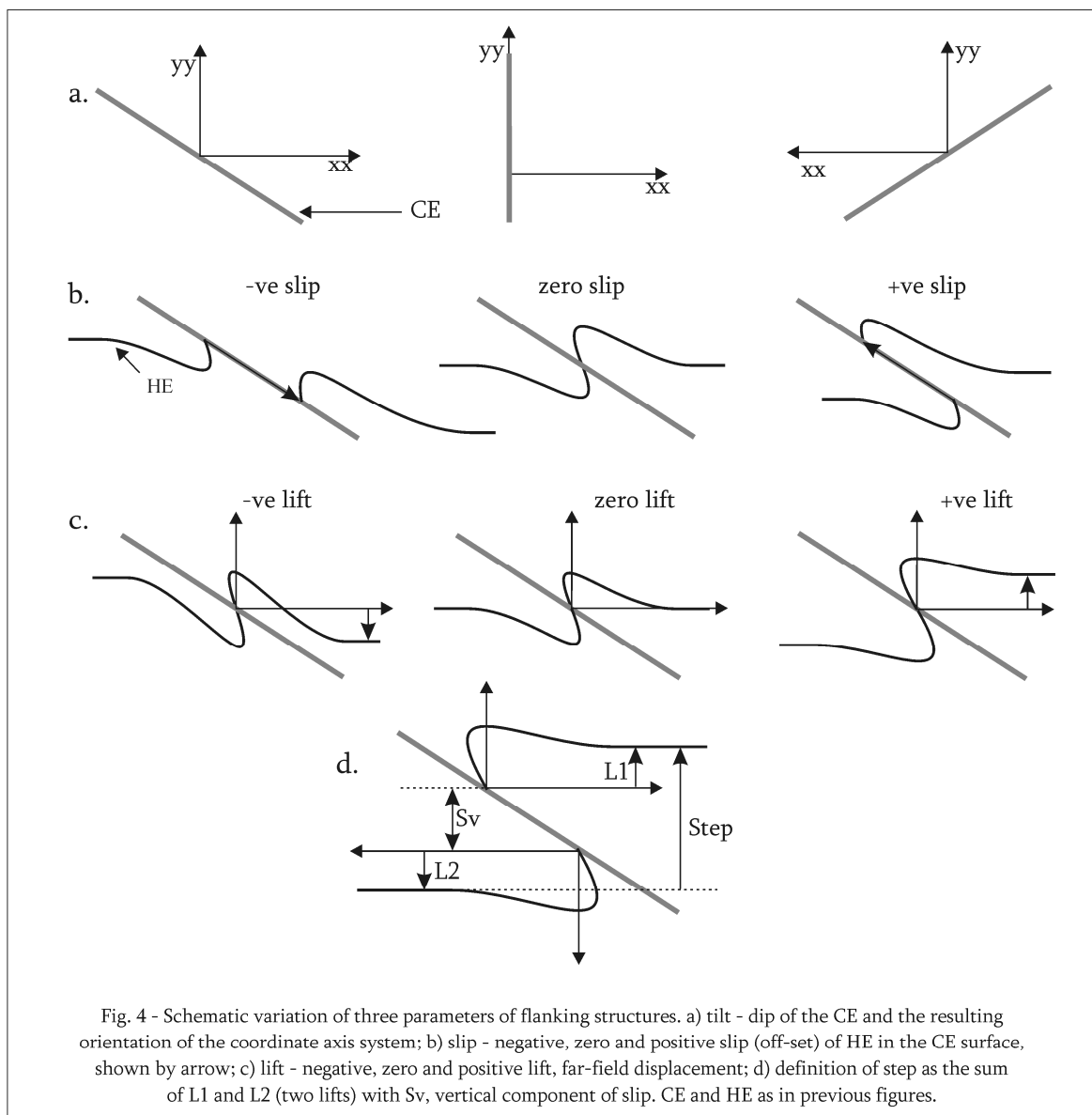
**Tilt** (angle  $\alpha$ ) is defined as the dip of the CE (Fig.4a). The Cartesian coordinate axes are drawn to represent a positive x-axis in the sense of the dip. Due to this, tilt is given by an angular value  $\alpha$ , measured between the x-axis and the CE, ranging between 90-180°. This convention is advantageous because it does not allow double geometries of mirror-image structures.

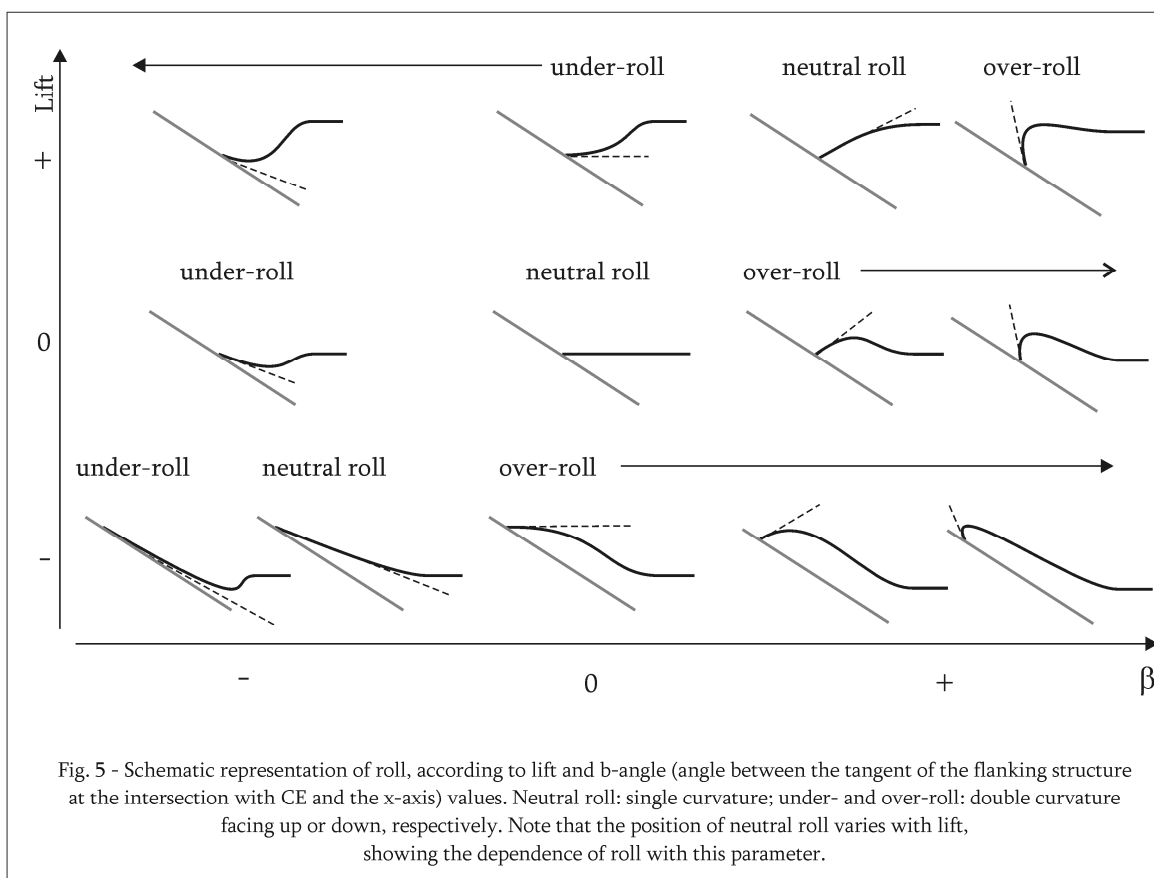
**Slip** is the displacement (off-set) of the HE observed on the CE surface (Fig.4b). Slip is also a completely independent parameter, since its value depends not on the geometry of the flanking structure itself, but on the relationship with the other half of the structure. This is fortunate for description purposes because the absence of clear markers makes slip sometimes difficult to observe in the field. As an independent parameter, slip can be conventionally defined as being positive if against the sense of dip of the CE (tilt), negative if according to dip and neutral if inexistent. When other independent shear criteria are present, slip description can be refined using the nomenclature of Grasemann and Stüwe (2001): co-shear slip, if in the same sense of the regional shear zone; and counter-shear slip, if opposite.

**Lift** is the far field displacement of the external HE measured with respect to the x-axis (Fig.4c). It is a parameter independent of tilt and slip. Lift is considered positive when the HE is above the x-axis and negative in the opposite situation. Notice that this definition only includes one side of the flanking structure. This is useful because correlation between layers on both sides of the CE is sometimes difficult. Moreover, it allows definition of lift when a counterpart is absent, such as in the case of flanking

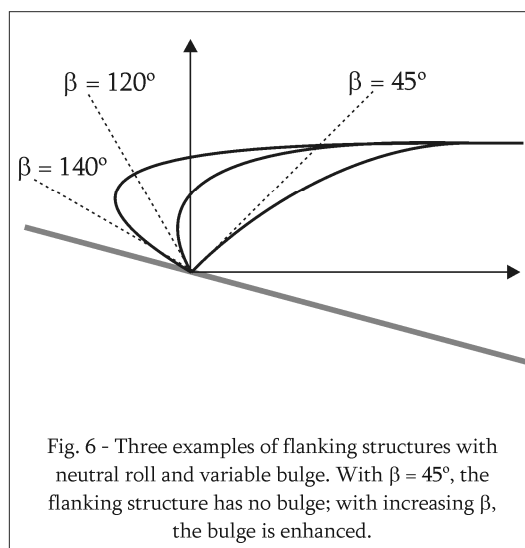


structures around rigid objects. If a correlation of layers can be established across the CE, we can define a parameter *step* as the orthogonal distance between the HE of the hanging and footwall in the far field. This means that, if the layering is horizontal, *step* is equal to *throw*, a term which is frequently used in petroleum geology (Tearpock and Bischke, 2003) (Fig.4d). Step is the sum of the lift of corresponding parts of a HE on both sides of a CE, plus the vertical component of slip. This parameter, although useful for description purposes of symmetric flanking structures, will not be used in the following classification.





Lift, slip and tilt are not enough to describe the geometry of flanking structures. An additional factor is needed to describe the curvature of the structure. **Roll** describes the magnitude and sense of the curvature observed in the flanking structure (Fig.5). Roll differs from the other parameters in that it is dependent on lift. In the simplest case, the curvature is a single open fold and roll is described as neutral. When lift is zero and roll neutral, the flanking structure is a straight layer that ends in a cross-cutting element. Neutral roll flanking structures



can be enhanced with bulge (Fig.6). When the curvature is composite, that is, when it has an inflexion point, roll is not neutral. If the curvature faces down, the flanking structure has over-roll; if the curvature faces up, the flanking structure has under-roll (Fig.5). Due to the nature of double curvatures, all under- and over-roll flanking structures have bulge by default.

Although not an essential parameter, the angle  $\beta$ , measured between the x-axis and the tangent of the flanking structure at the intersection with the CE, can be useful to refine the geometric description.  $\beta$  is mainly responsible for the presence or absence of bulge in neutral roll flanking structures (cf. Fig.6). This angle ranges, in theory, between  $-180^\circ$  and  $180^\circ$ , but in practise is limited by the amount of tilt, since a realistic flanking structure never crosses its own cross-cutting element ( $\beta < \alpha$ ).

Excluding tilt, which is not directly related to the geometry of the flanking structure itself the combinations of slip, lift and roll define a set of 27 theoretically possible geometries (Fig.7).

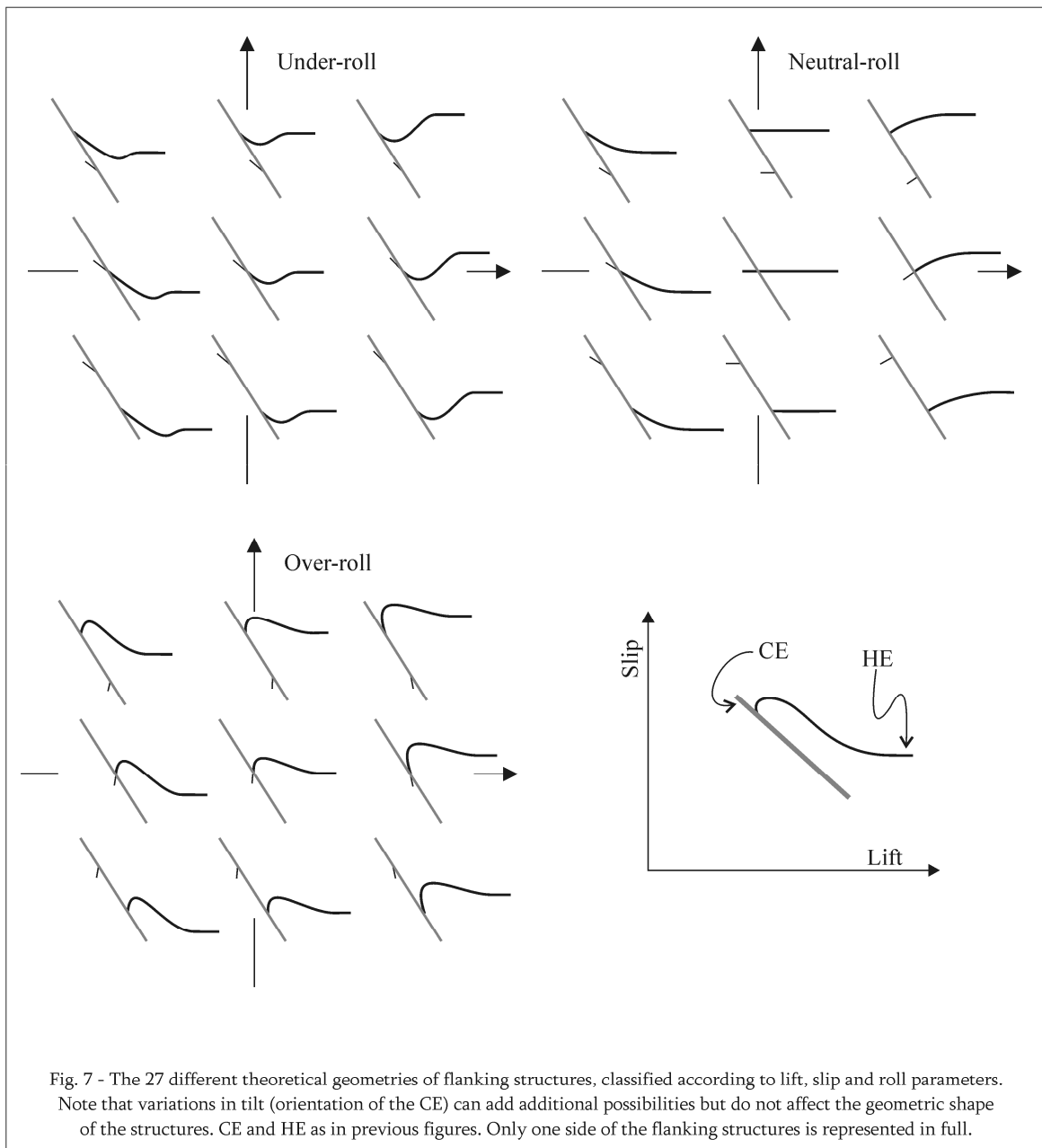
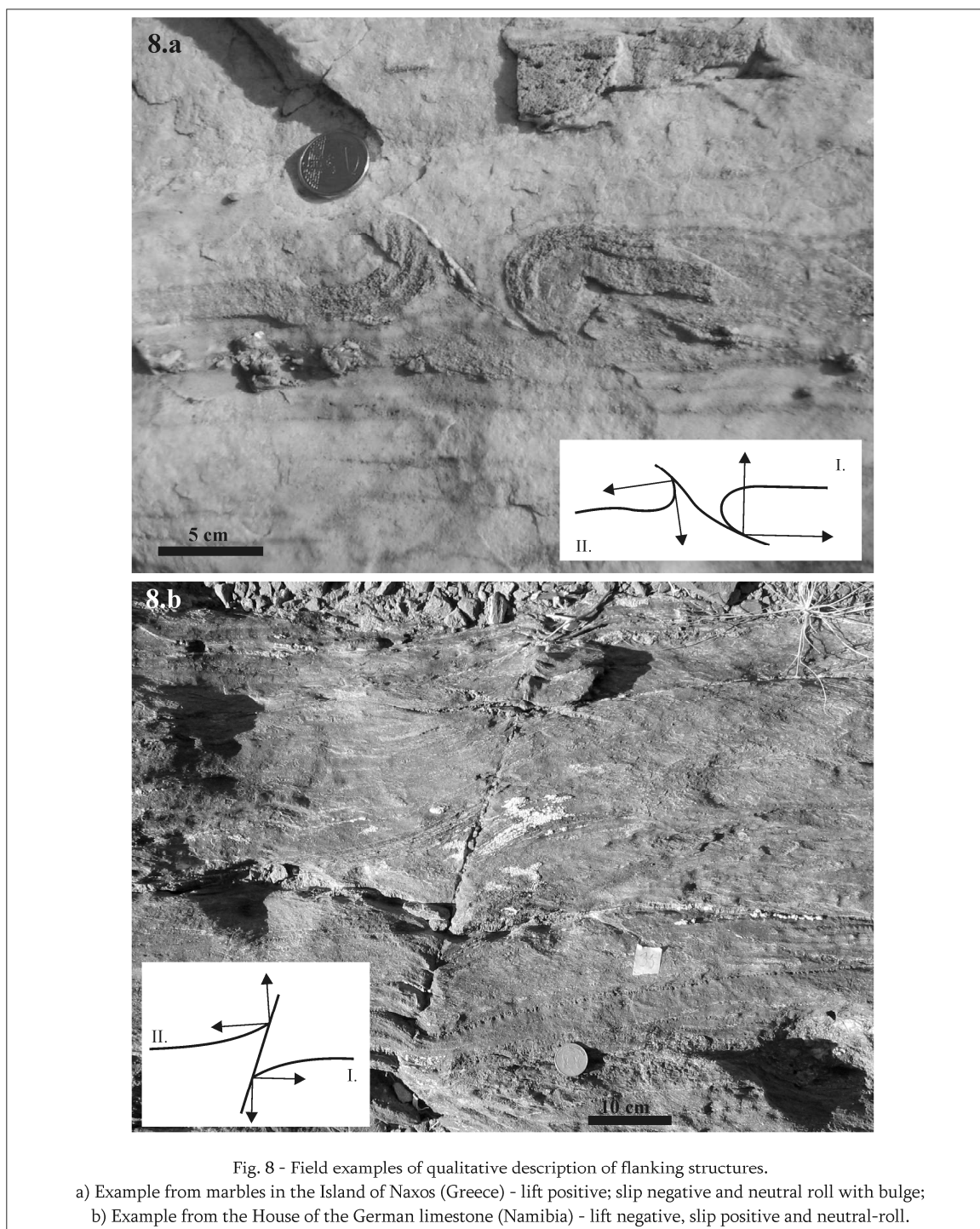


Fig. 7 - The 27 different theoretical geometries of flanking structures, classified according to lift, slip and roll parameters. Note that variations in tilt (orientation of the CE) can add additional possibilities but do not affect the geometric shape of the structures. CE and HE as in previous figures. Only one side of the flanking structures is represented in full.



## 2.1 Example

Fig.8a gives an example of a flanking structure developed in marbles from Naxos Island (Greece) around a quartz vein. Drawing the appropriate coordinate systems (Fig.8a, inbox) and using the parameters outlined above, the flanking structure can be described as: lift positive; slip negative and neutral roll with bulge. This classification applies to both sides of the flanking structure, despite that in

this natural example, they are not absolutely equal in shape: the curve in (I) has a more enhanced bulge than (II), although they are both neutral roll examples. In practice there can be gradients in the parameters from layer to layer along a CE.

Fig.8b is an example of flanking structures around a quartz vein in marbles, this one from a marble unit in Namibia. The flanking structure in the central layer is described as lift negative, slip positive and neutral-roll. In this example, shear sense is sinistral according to independent criteria (not shown in picture) and thus slip may be further classified as counter-shear slip.

Qualitative description of flanking structures is suggested for use as a field tool, since it is based on parameters that are easy to recognise and does not involve measurements or a detailed analysis. However, this qualitative description does not allow an accurate comparison between outcrops, or even flanking structures within a single occurrence. The quantitative description outlined below is based on analytical modelling of Bézier curves and quantifiable parameters and is more adequate for detailed studies.

### 3. Quantitative description

The use of Bézier curves as a tool to describe curvatures and surfaces was introduced by French engineers of the automobile industry, in particular Bézier (1966 and 1967). More recently, the concept was recognised as useful in geological description (De Paor, 1996) and used as a tool for fold shape analysis (Srivastava and Lisle, 2004). The concept will now be applied to flanking structures.

A general cubic Bézier curve (Fig.9a) is described by its node-points *a*, *b*, *c*, and *d* and the two governing parametric equations,

$$\begin{aligned} x(t) &= (1-t)^3 x_a + 3t(1-t)^2 x_b + 3t^2(1-t)x_c + t^3 x_d \\ y(t) &= (1-t)^3 y_a + 3t(1-t)^2 y_b + 3t^2(1-t)y_c + t^3 y_d \end{aligned} \quad (\text{Eq. 1})$$

which can be adapted to flanking fold geometry (Fig.9b). Node-point *a* can be defined as the intersection between the flanking structure and the

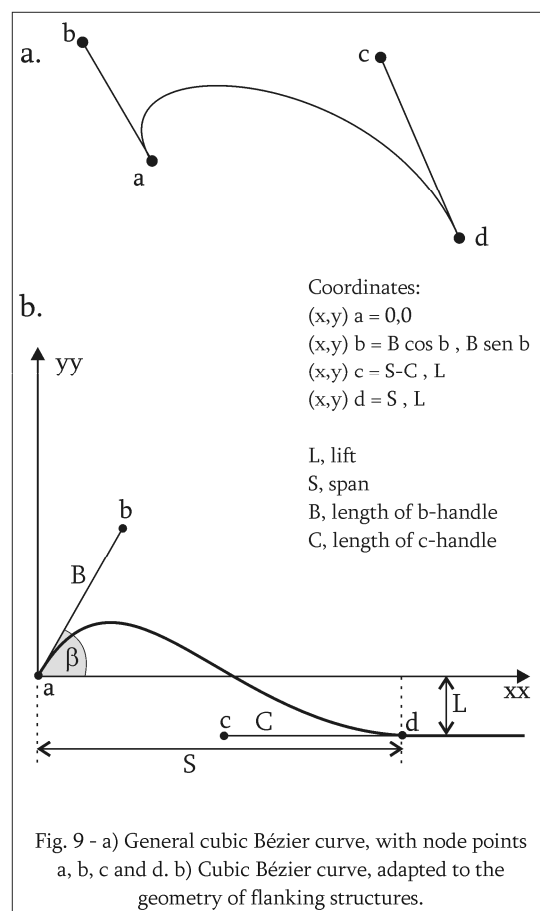


Fig. 9 - a) General cubic Bézier curve, with node points *a*, *b*, *c* and *d*. b) Cubic Bézier curve, adapted to the geometry of flanking structures.

cross-cutting element and  $d$  as the first deflection of the host-element attributed to the flanking structure effect.  $b$  and  $c$  are Bézier nodes with no geological equivalent. Thus,  $a$  is the origin of the coordinate system,  $x_d$  is always positive and  $y_c = y_d$ . The later assumption prevents curves with sharp bends where a flanking structure grades into the far-field layer geometry. Although such sharp bends are possible as abstract geometries, they are geologically unrealistic.

With these assumptions the general parametric Eq.1 can be rewritten as:

$$\begin{aligned} x(t) &= t(3x_b) + t^2(-6x_b + 3x_c) + t^3(3x_b - 3x_c + x_d) \\ y(t) &= t(3y_b) + t^2(-6y_b + 3y_c) + t^3(3y_b - 2y_d) \end{aligned} \quad (\text{Eq.2})$$

Some of these parameters can be determined by detailed field analysis of the flanking structures (Fig.9b).  $y_d$  is the mathematical equivalent of the **Lift** ( $L$ ) parameter discussed previous in this work.  $x_d$  can be defined as the **Span** ( $S$ ) of the flanking structure.  $x_b$  and  $y_b$  can be described as polar coordinates using angle  $\beta$  (which can be directly measured from field examples) and  $B$ , the length of the Bézier handle  $b$ . After the appropriate substitutions and simplifications, Eq.2 becomes:

$$\begin{aligned} x(t) &= t(3B \cos \beta) + t^2(-6B \cos \beta + 3S - 3C) + t^3(3B \cos \beta - 2S + 3C) \\ y(t) &= t(3B \sin \beta) + t^2(-6B \sin \beta + 3L) + t^3(3B \sin \beta - 2L) \end{aligned} \quad (\text{Eq.3})$$

To allow comparison between studied examples, it's useful to normalise these equations and transform its parameters into dimensionless numbers. The chosen normalization parameter is the Span,  $S$ . Eq.3 can thus be rewritten as:

$$\begin{cases} \bar{x}(t) = (3\bar{B} \cdot \cos \beta) \cdot t + (-6\bar{B} \cdot \cos \beta + 3 - 3\bar{C}) \cdot t^2 + (3\bar{B} \cdot \cos \beta - 2 + 3\bar{C}) \cdot t^3 \\ \bar{y}(t) = (3\bar{B} \cdot \sin \beta) \cdot t + (-6\bar{B} \cdot \sin \beta + 3\bar{L}) \cdot t^2 + (3\bar{B} \cdot \sin \beta - 2\bar{L}) \cdot t^3 \end{cases} \quad (\text{Eq.4})$$

Where

$$\begin{aligned} \bar{x} &= x/S; \bar{y} = y/S \\ \bar{B} &= B/S; \bar{C} = C/S \\ \bar{L} &= L/S \end{aligned}$$

Parameters  $S$  and  $\bar{L}$  can be obtained from field examples.  $\bar{B}$  and  $\bar{C}$ , the lengths of the Bézier-handles (Fig.9b), can be estimated using a simple spreadsheet and a graphic in conjunction with Eq.4. In a Bézier curve, these two handles determine the shape of the geometric curve and it is important to understand their behaviour before attempt estimation.

The length of the **B**-handle controls, with respect to the coordinate system, the vertical shape of the flanking structure (Fig. 10). Relatively big  $\bar{B}$  values are expected when over- or under-roll occur. On the other hand, the **C**-handle is responsible for the horizontal (again with respect to the coordinate axis)

extension of the structure. Large  $\bar{C}$  values will make the curvature sharper, whilst open gentle curves are expected when  $\bar{C}$  is low.

The analytical modelling presented above considers cubic Bézier curves, based on third degree Bernstein polynomials. It is possible to increase accuracy in the definition of the flanking structures by increasing the degree of the Bézier curve itself. This procedure, however, leads to equations of the fourth or fifth degree. The extra detail accomplished does not warrant the unpractical increasing complexity of classification.

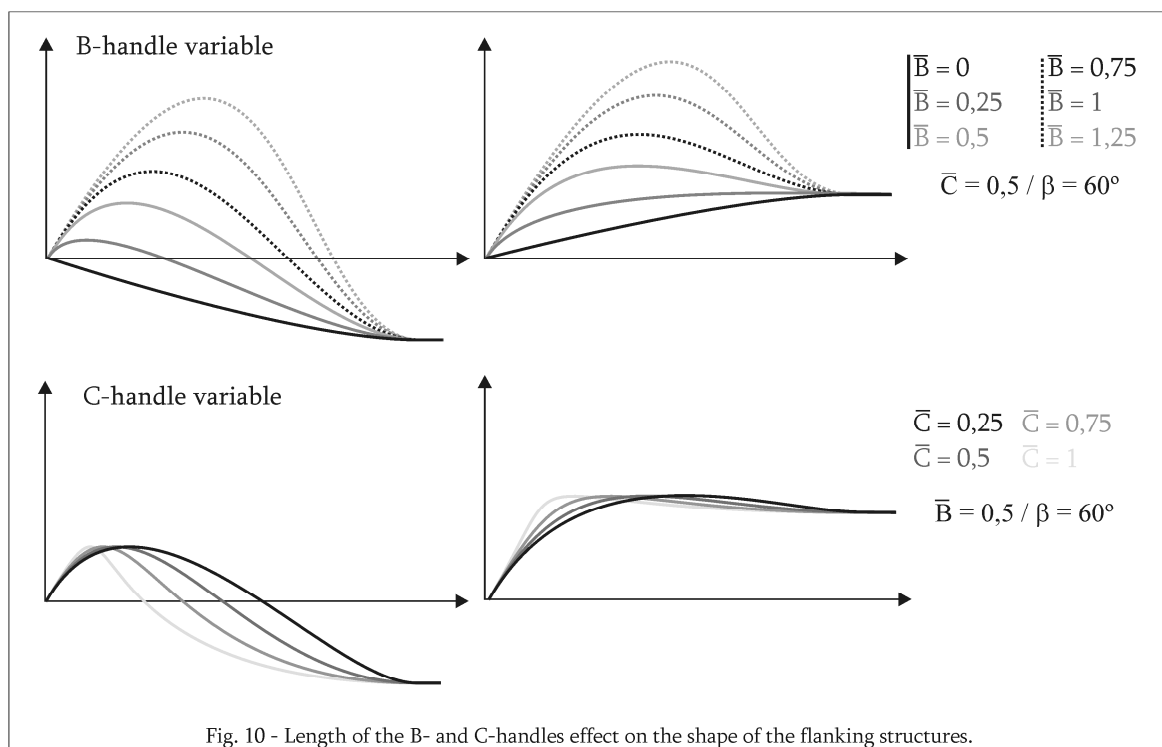


Fig. 10 - Length of the B- and C-handles effect on the shape of the flanking structures.

### 3.1 Example

A set of flanking structures developed around a fault in a marble unit in Namibia (Fig.11a) was chosen to exemplify the quantitative method here presented. This is an example of flanking structure where detailed quantitative data is needed to compare different CE and associated gradients of flanking structures. Such data can be used to draw conclusions about possible rotation or lateral growth of this type of feature. The chosen set of flanking structures is highly variable in shape from layer to layer along the CE (Table 1, qualitative description line), although parameter slip is positive throughout the fault. The first step to compare the flanking structures in different layers is to sketch the whole structure. Then, the parameters  $\mathcal{S}$ ,  $\mathcal{L}$  angle  $\beta$  are measured in all selected points (Table 1). Since the equations

consider normalised non-dimensional parameters, the measuring unit is not relevant. Also, due to the normalization of the span, it's possible and more practical to choose a common span value for all structures since, in most natural examples, it's difficult to determine with precision the first inflexion of the flanking structure (Fig.9b). Using a spread sheet program and Eq.4 outlined above, parameters  $\bar{B}$  and  $\bar{C}$  can be estimated with the construction of a graphic (Fig.11c) which helps to visualise the best fit. To test the validity of this estimation, the actual length of the B and C handles was measured for each flanking structure, using the Bézier function of a drawing program. The estimated parameters, as well as the read values, are listed in the table of Fig.11. Despite some punctual differences, the values show that the estimated and are very close to the actual values (Table 1). Moreover, applying the correct values to Eq.4 returns a graphic very similar to the obtained with estimated parameters. Although estimation introduces error, overall results show that this error will have only a minor implications.

The quantitative parameters  $\bar{B}$  and  $\bar{C}$ , both estimated and exact, as well as  $S$  and  $L$  were projected in the graphic shown on Fig.11d. This allows visualization of the gradient of the referred parameters across layers along the fault. In this particular example, the quantifying method permits the following conclusions:

- 1) *Lift* steadily decreases from the top to the bottom of the structure;
- 2)  $B$  (Fig.9b) remains fairly constant throughout the set;
- 3)  $C$  is variable and, together with lift and angle  $\beta$ , the main responsible for the variable geometries observed;
- 4) The flanking structures, although geometrically different, reflect a consistent evolution of parameters along the cross cutting element.

Parameters	Point 1	Point 2	Point 3	Point 4	Point 5	Point 6
$\beta$	85°	81°	-13°	-29°	-32°	-31°
L	0.14	0.02	-0.10	-0.29	-0.29	-0.32
$\bar{B}$ (estim.)	0.21	0.19	0.22	0.16	0.20	0.16
$\bar{C}$ (estim.)	0.26	0.73	0.67	0.61	0.64	0.63
$\bar{B}$ (read)	0.21	0.20	0.13	0.14	0.14	0.14
$\bar{C}$ (read)	0.53	0.79	0.72	0.39	0.62	0.57
Qualitative description	L+	L+	L-	L-	L-	L-
	Nroll	Oroll	Nroll	Nroll	Nroll +b	Nroll -b

Table 1 - Quantitative parameters of the set of flanking structures shown in figure 11a and drawn in figure 11b. Sn, normalized span; Ln, normalized lift; Bn and Cn, normalized length of handle B and C; est, estimated with parametric equations; read, real value of the normalized length of handle B and C; L+/L-, positive / negative lift; Nroll, neutral roll; Oroll, over-roll; +b, with bulge.

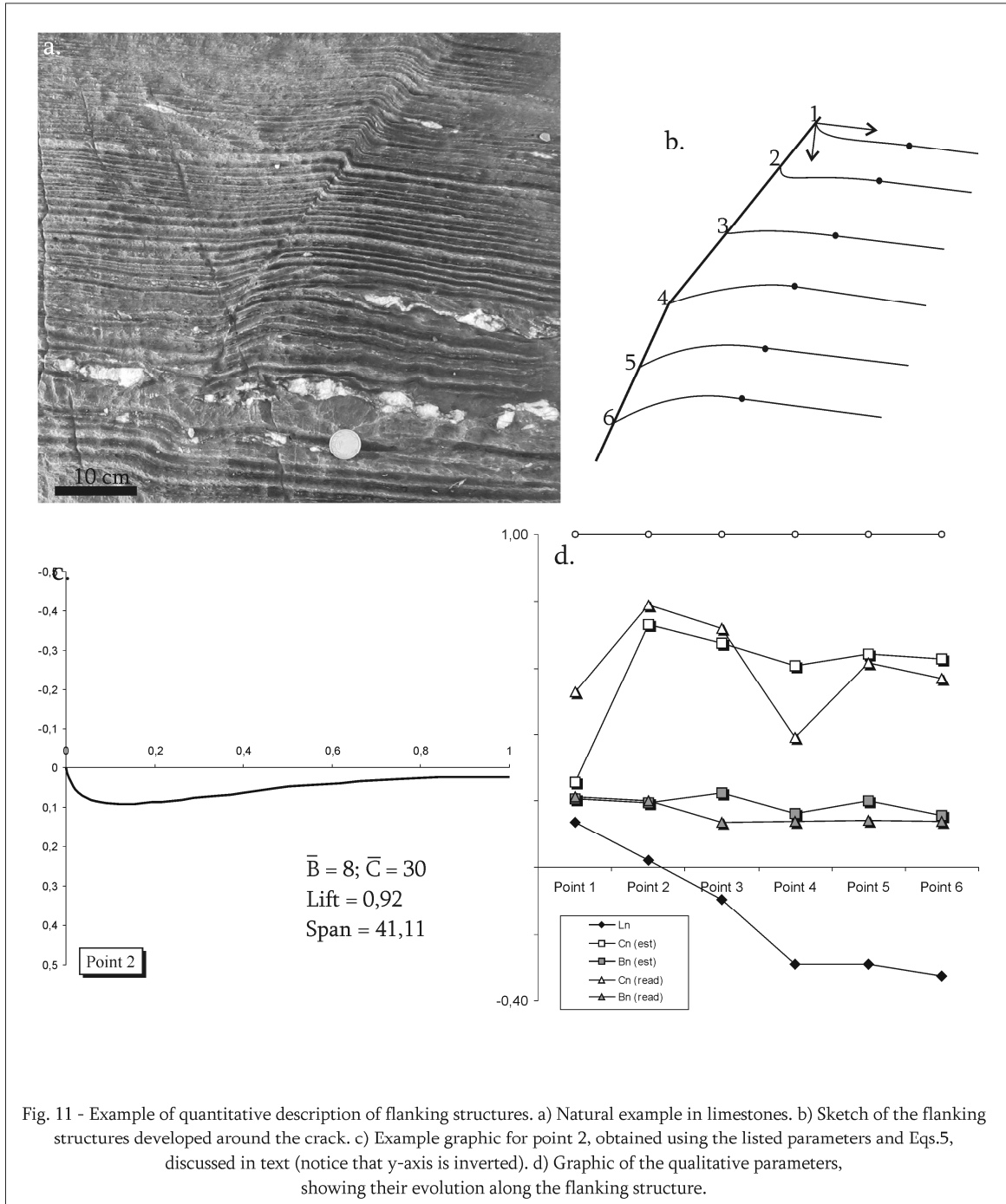


Fig. 11 - Example of quantitative description of flanking structures. a) Natural example in limestones. b) Sketch of the flanking structures developed around the crack. c) Example graphic for point 2, obtained using the listed parameters and Eqs.5, discussed in text (notice that y-axis is inverted). d) Graphic of the qualitative parameters, showing their evolution along the flanking structure.

## *4. Conclusions*

A method was presented for general description of flanking structure geometries observed in Nature using a relatively simple set of parameters. This can be done with two levels of accuracy. A qualitative method was described using the geometric features tilt, lift, slip and roll, which result in 27 different theoretical combinations that reflect virtually all possible cases observable in nature. This qualitative approach is recommended to use in field description of isolated flanking structures. A quantitative method, based in analytical modelling of Bézier curves, requires measurement of geometric features and mathematical treatment, but allows comparison between flanking structures.

## References

- Bézier, P., 1966. Definition numérique des courbes et surfaces – I. *Automatisme* 11, 625-632
- Bézier, P., 1967. Definition numérique des courbes et surfaces – II. *Automatisme* 12, 17-21
- De Paor, D.G., 1996. Bézier curves and geological design. In: De Paor, D.G. (Ed), *Structural Geology and Personal Computers*. Pergamon Press, pp. 389–417.
- Exner, U., Mancketow, N.S., Grasemann, B., 2004. Progressive development of s-type flanking folds in simple shear. *Journal of Structural Geology* 26, 2191-2201.
- Gayer, R.A., Powell, D.B., Rhodes, S., 1978. Deformation against metadolerite dykes in the Caledonides of Finnmark, Norway. *Tectonophysics* 46, pp. 99–115.
- Ghosh, S.K., 1975. Distortion of planar structures around rigid spherical bodies. *Tectonophysics* 28, 185-208.
- Grasemann, B., Stüwe, K. 2001. The development of flanking folds during simple shear and their use as kinematic indicators. *Journal of Structural Geology* 23, 714-724.
- Grasemann, B., Stüwe, K., Vannay, J.C. 2003. Sense and non-sense of shear in flanking structures. *Journal of Structural Geology* 25, 19-34.
- Hamblin, W. K. 1965. Origin of "reverse drag" on the down-thrown side of normal faults. *Geological Society of America Bulletin* 76, 1145-1164.
- Hudleston, P.J. 1989. The association of folds and veins in shear zones. *Journal of Structural Geology* 11, 949-957.
- Leith, C. K. 1914. *Structural Geology*. Constable, London.
- de Margerie, E., Heim, A. 1888. *Dislocations de L'écorce terrestre - Essai de définition et de nomenclature*. Verlag von J. Wurster & Comp., Zürich.
- Passchier, C.W., 2001. Flanking structures. *Journal of Structural Geology* 23, 951-962.
- Playfair, J., 1802. *Illustrations of the Huttonian theory of the earth*. William Creech, Edinburgh.
- Ramberg, H., 1963. Evolution of drag folds. *Geological Magazine* 100(2), 97-106.
- Srivastava, D.C., Lisle, R.J., 2004. Rapid analysis of fold shape using Bézier curves. *Journal of Structural Geology* 26, 1553-1559
- Suess, E., 1885. *Das Antlitz der Erde*. Tempsky, F.; Freytag, G., Prag and Wien; Leipzig.
- Tearpock, D.J., Bischke, R.E., 2003. *Applied Subsurface Geological Mapping*. Prentice Hall, New Jersey.
- Wiesmayr, G., Grasemann, B., 2005. Sense and non-sense of shear in flanking structures with layer-parallel shortening: implications for fault-related folds. *Journal of Structural Geology* 27, 249-264.

## Chapter II - Riedel-shear control on the development of pennant veins: field example and analogue modelling.

### *1. Introduction*

Veins are extension fractures filled with mineral deposits, commonly quartz or calcite, and one of the most common features in deformed rocks of all types and metamorphic grades. Opening of veins is structurally controlled by orientation of fractures in a volume of rock but other parameters, like pore fluid pressure or porosity, are also important. Single or en échelon tension gashes (Fig. 1a; eg Ramsay and Huber, 1983; Olson and Pollard, 1991), wing cracks (eg Horii and Nemat-Nasser, 1985; Willemse and Pollard, 1998) and swordtail terminations in boudin parting surfaces (Swanson, 1992) are common examples of veins developed as *mode I* extension fractures. As such, they can be used in the interpretation of bulk flow kinematics and are an important source of information on the deformation history of the host-rock, especially if associated with fibres (eg Bons, 2000; Köhn et al., 2000; Hilgers and Urai, 2002). However, pure tension fractures are not the only structural control on the development of veins. This chapter explores an alternative way of opening space for mineral deposition controlled by Riedel (R) and anti-Riedel (R') conjugate shear fractures. Riedel shear fractures were first recognised as a principal feature of brittle to semi-brittle shear zones by Riedel (1929), who produced these structures in analogue experiments with clay. The subject has since been the focus of extensive research in field studies (eg Moore, 1979; Davis et al., 1999; Ahlgren, 2001; Katz et al., 2004), analogue modelling with clay (eg Cloos, 1955; Wilcox et al., 1973; Tchalenko, 1968; Smith and Durney, 1992; Marques, 2001) and sand (eg Naylor et al., 1986), direct shear experiments (eg Bartlett et al., 1981; Moore and Byerlee, 1992; Schreus, 1994) and numerical modelling (eg Dresen, 1991; Braun, 1994; McKinnon and Garrido de la Barra, 1998). These works resulted in a widely accepted model of shear fracture orientation in non-coaxial deformation, illustrated in Fig. 1b. The most conspicuous element of this idealised geometry is the Riedel conjugate set, comprising synthetic Riedel fractures (R) and conjugate antithetical Riedel fractures (R'), oriented at  $45^\circ \pm \phi/2$ , where  $\phi$  is internal angle of friction of the rock. Also important are synthetic P-shear fractures (at  $-45^\circ + \phi/2$ ) and the purely tensional T fractures (at  $45^\circ$  in simple shear). The precise angular relationships of the different sets of fractures and the shear plane are dependent on the internal angle of friction, as well as on the strain rate and stress state (Ahlgren, 2001) and vorticity (Smith and Durney, 1992). This framework is generally interpreted as precursor to faults in a

synthetically-driven model (eg Ahlgren, 2001) where R-fractures are the first to develop, followed by P-fractures. This chapter investigates the influence of R-R' conjugate fractures as structural controls on veins, following the work of Swanson (1992), who suggested that R-fractures had some role in the kinematics of vein terminations, and introduces pennant veins, a new type of vein geometry, based on field observations in Namibia and analogue modelling.

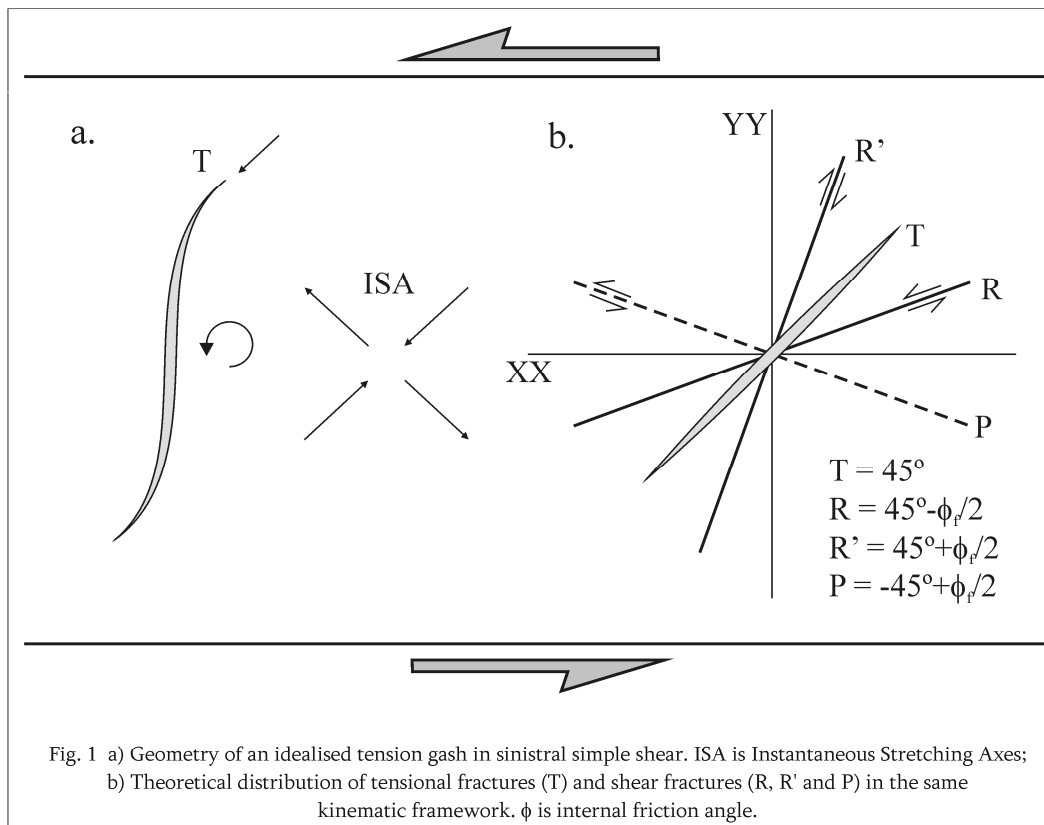
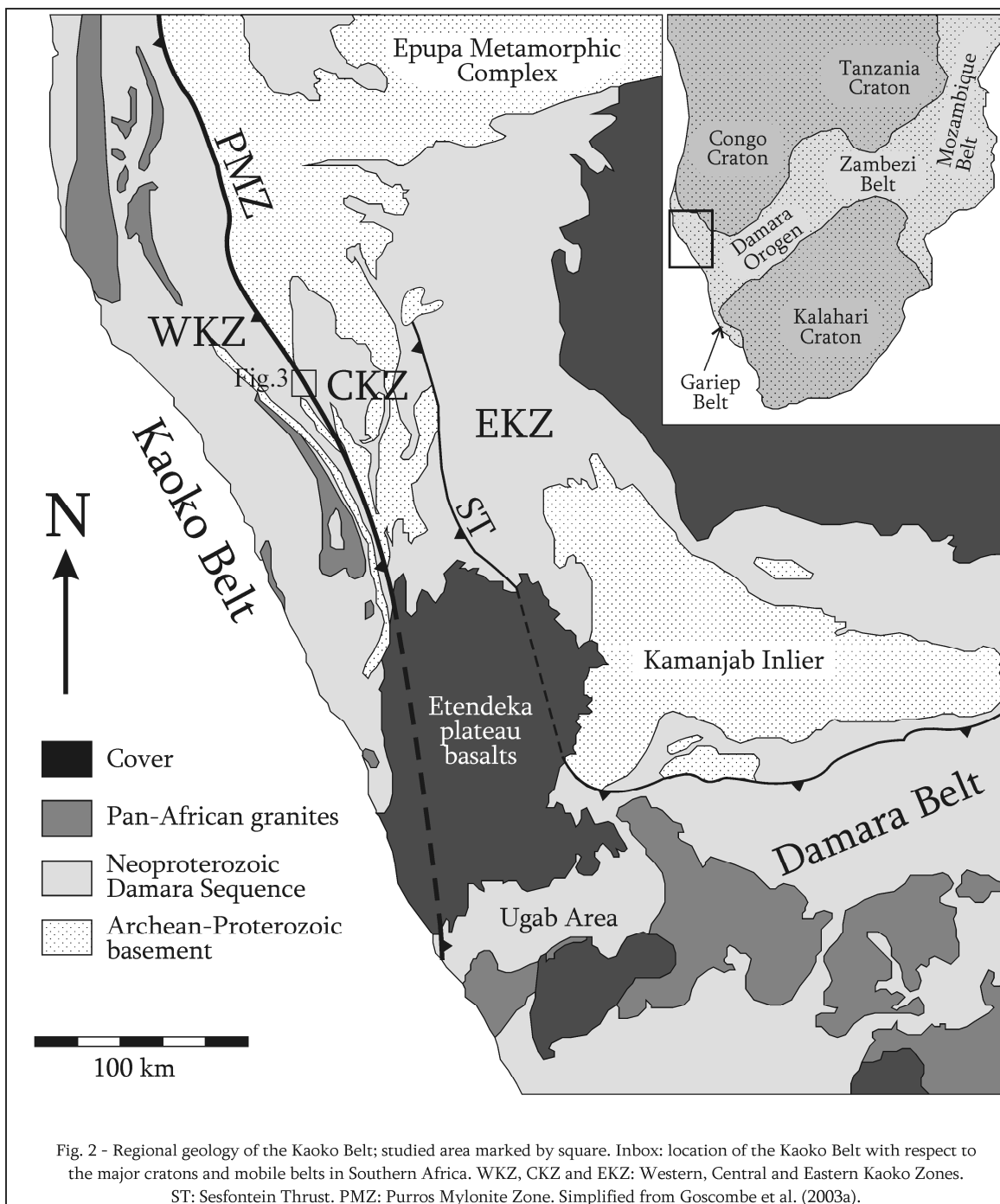


Fig. 1 a) Geometry of an idealised tension gash in sinistral simple shear. ISA is Instantaneous Stretching Axes; b) Theoretical distribution of tensional fractures (T) and shear fractures (R, R' and P) in the same kinematic framework.  $\phi$  is internal friction angle.

## 2. Geological setting

The Kaoko Belt in Namibia is a NNW trending, oblique convergent orogen, divided into three zones (Goscombe et al. 2003a; 2005a,b; Konopásek et al. 2005; Fig. 2). The West Kaoko Zone (WKZ) includes basement composed of Panafrican migmatites and granites with amphibolite to granulite metamorphic facies (Goscombe et al. 2003b; 2005a). The Central Kaoko Zone (CKZ) comprises Paleoproterozoic basement of migmatitic and gneissic rocks with a Neoproterozoic cover of deep basin and slope facies (Damara sequence - Goscombe et al. 2003a, Konopásek et al. 2005). Metamorphic conditions on the CKZ grade from upper-amphibolite facies in the West to lower greenschist facies in the East (Goscombe et al. 2003b; 2005a, Konopásek et al. 2005). The East Kaoko Zone (EKZ) represents the foreland of the orogen and comprises subgreenschist Damara sequence rocks of shelf facies

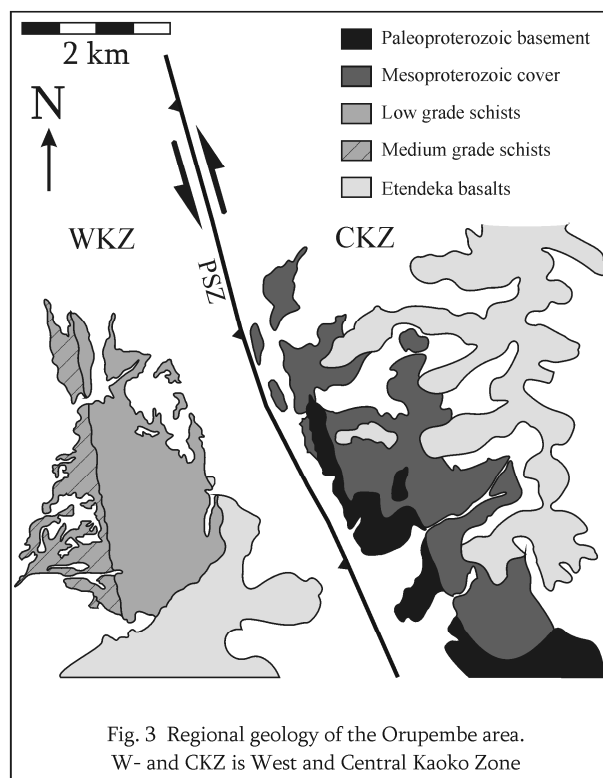
(Goscombe et al. 2003a,b). The WKZ and CKZ are separated by the Purros Mylonite Zone (PMZ), a crustal-scale, sub-vertical and sinistral strike-slip ductile shear zone, with a length of over 400 km extending from the South of Angola to the Ogden Rocks in the East of the Ugab zone (Passchier et al., 2002).



Deformation in the Kaoko Belt consists of three tectonic phases, the first of which (M1) only occurs in the WKZ (Goscombe et al. 2003a, 2005b; Konopásek et al. 2005). The second deformation phase (M2), active between 580-550 Ma, was dominated by transpressive deformation at peak

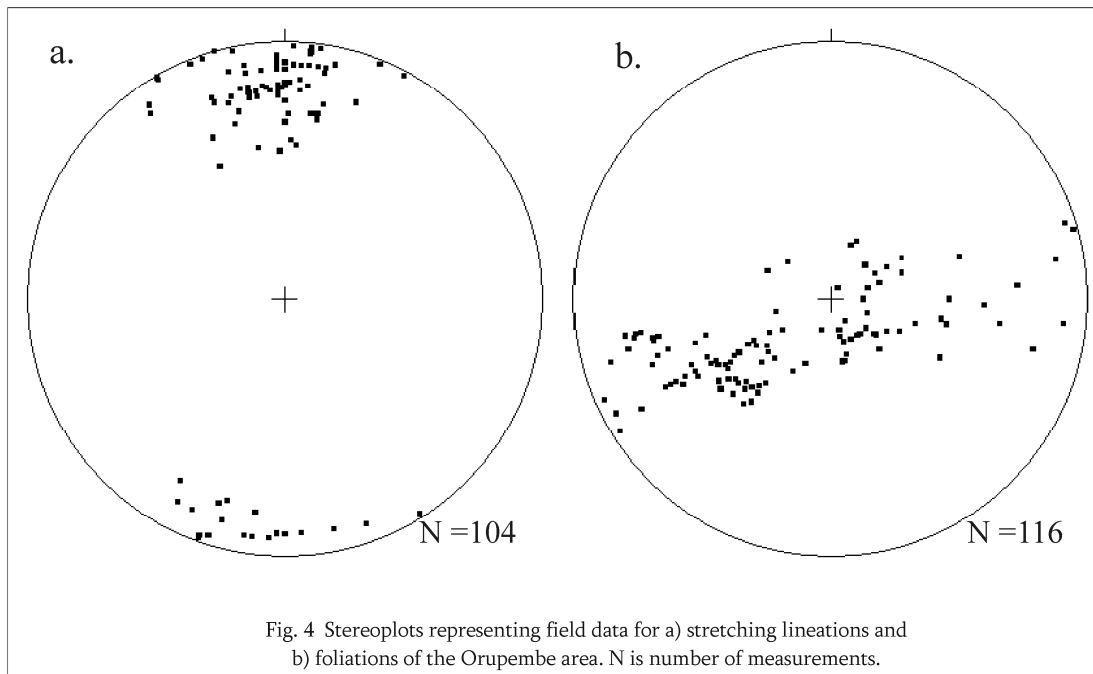
metamorphic conditions and during cooling, progressing from a wrench stage (M2w) to a convergent stage (M2c) (Goscombe et al. 2003a). The wrench stage is related to activity of the PMZ and resulted in pervasive and intense non-coaxial deformation that produced the dominant LS-fabric in the area. The convergent stage is considered continuous with the wrench stage and develops pervasive east-vergent folds with shallow plunging axes. These folds do not develop axial planar cleavage, although crenulation cleavage parallel to early M2w lineations is common in selected rock types. The axial plane varies in dip across the orogen and defines a large scale asymmetric flower structure, centred on the PMZ and evolving to the East as west dipping, progressively shallower, east-vergent nappes (Goscombe et al. 2003a). The third deformation phase (M3, between 535-505 Ma) resulted in North-South shortening of the orogen and produced large scale upright folds without an axial planar foliation. With these features, the Kaoko Belt represents a Neoproterozoic, crustal scale, sinistral transpressional orogen with flower structure architecture (Goscombe et al., 2003a, 2005b).

This study focuses on an area located near Orupembe which straddles the border between the WKZ and CKZ zones including outcrops of the Purros Mylonite Zone (Fig. 3). In Orupembe, the WKZ consists of a Neoproterozoic low grade turbiditic sequence with M2 deformation features. The PMZ is about 2 km wide, steeply dipping (60-70°) to the West and includes slivers of basement granitoid rocks. The CKZ locally consists of Paleoproterozoic basement comprising a granodioritic migmatite with hornblende and epidote layers overlain by pink orthogneiss with feldspar augen. The basement is covered by Mesoproterozoic quartzites and the Neoproterozoic Damara Sequence comprising (bottom to top) interbedded impure quartzites, calcsilicate rocks and micaschists,



followed by diamictites and cap carbonates (Hoffman et al., 1994). The main deformation feature throughout the area is an LS fabric produced by the M2 wrench stage. The foliation is generally gently dipping and parallel to bedding. It consist of recrystallised feldspar and epidote in the quartzitic and calcsilicate rocks, and aligned micas in the micaschist units.

The lineation trends approximately NS and is a shallow plunging quartz-feldspar aggregate lineation (Fig. 4a). Associated shear sense criteria, such as mantled objects and rare shear bands, indicate sinistral shear sense consistent with the overall kinematics of the Purros Mylonite Zone. The foliation is steeply dipping near the PMZ and evolves to the East into open folds with a gently SSE plunging axis and sub-vertical axial plane (Fig. 4b). This folding is related to the M2 convergent stage and does not develop a regional axial planar cleavage. However, micaschist units present a NNW/SSE trending crenulation lineation parallel to the fold axis of the large scale folds. The quartzitic more competent units do not develop mesoscopic folding. Instead they present a new type of vein geometry, which is the main focus of this study.



### 3. Quartz veins from the CKZ in Orupembe

Detailed field work in Orupembe revealed the presence of two different types of quartz veins (Fig. 5 and 6). Although the geometry of these veins is clearly distinct, they share common characteristics. Both occur in the same outcrops of quartzite interbedded with calcsilicate and micaschists layers and both represent sets of quartz veins developed under a metamorphic grade lower than that of the main stretching lineation, as suggested by their filling of quartz, less deformed than the host-rock, and the geometric cross-cutting of the main LS fabric. They are therefore late with respect to the main deformation that is ascribable to the wrench stage of the first deformation phase of the Kaoko

Belt. The first set of studied quartz veins has a typical sigmoidal geometry (Fig. 5; Fig. 6a,b). They are up to 20 cm in total length and up to 1 cm wide. These veins are unusual since their sigmoidal shape is visible only on the foliation plane and cannot be easily observed in planes orthogonal to the S-fabric, where they are short and straight. The main aggregate lineation is locally deflected near the centre of the sigmoidal veins. The tips and centres of these sigmoidal veins were measured as lines within the foliation plane, as summarised in Table 1. Tips define an average  $77^\circ$  angle with the lineation, whilst the centres are relatively less inclined with an average angle of  $34^\circ$ . In some examples, a younger vein generation cuts the central part of the veins with the same orientation as the tips (Fig. 6a).

The veins are interpreted as sigmoidal tension gashes, developed by progressive deformation of a quartz-filled tensional fracture oriented according to the maximum shortening instantaneous stretching axis (ISA) (cf. Fig. 1a; Ramsay and Huber, 1983; Passchier and Trouw, 2005). The second type of quartz veins has been observed in shallow dipping quartzitic units and has different characteristics (Fig. 5, Fig. 6c,d). These veins cut both the foliation and the aggregate lineation and can be observed in all surfaces of the outcrop. In the foliation plane, they present distinct triangular pennant-shaped terminations, hence the name pennant veins.

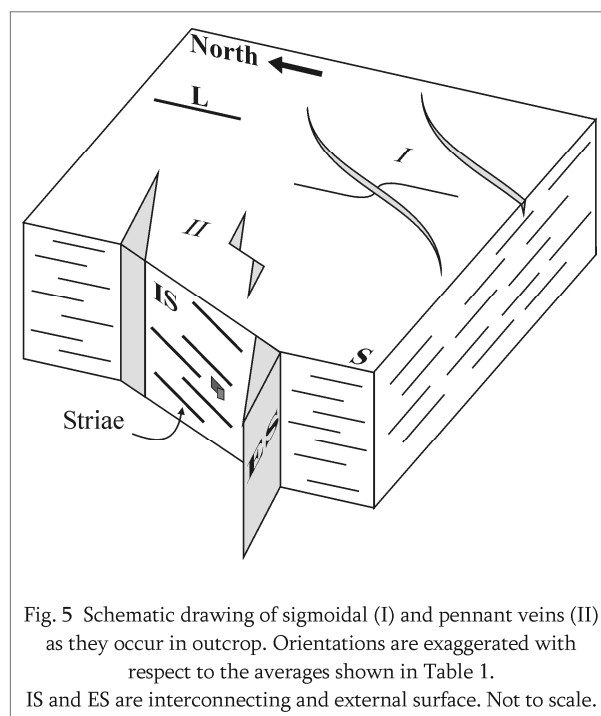


Fig. 5 Schematic drawing of sigmoidal (I) and pennant veins (II) as they occur in outcrop. Orientations are exaggerated with respect to the averages shown in Table 1. IS and ES are interconnecting and external surface. Not to scale.

These structures are up to 10 cm in length, measured in the foliation plane. The interconnecting surface (IS) is 5 to 20 cm wide and is usually not mineralised, although in some cases quartz is present uniting the pennant terminations in a single quartz vein. The orientation of the external surface (ES) of the pennants and interconnecting surface (IS) was measured in the field with results presented in Figure 7 and Table 1. The ES is approximately orthogonal to the regional NS lineation; the IS is less inclined to this fabric, with an average  $20^\circ$  angle to the external surface. The IS planes contain elongate white mica grains and striae, with shallow plunge to the SW and criteria suggesting downward motion of the southern block (Fig. 5). The striae make a small angle with the intersection line of the foliation and the IS. The mechanism causing the development of the pennant veins and associated features was not clear from field observations alone and therefore it was decided to use of analogue modelling as described below.

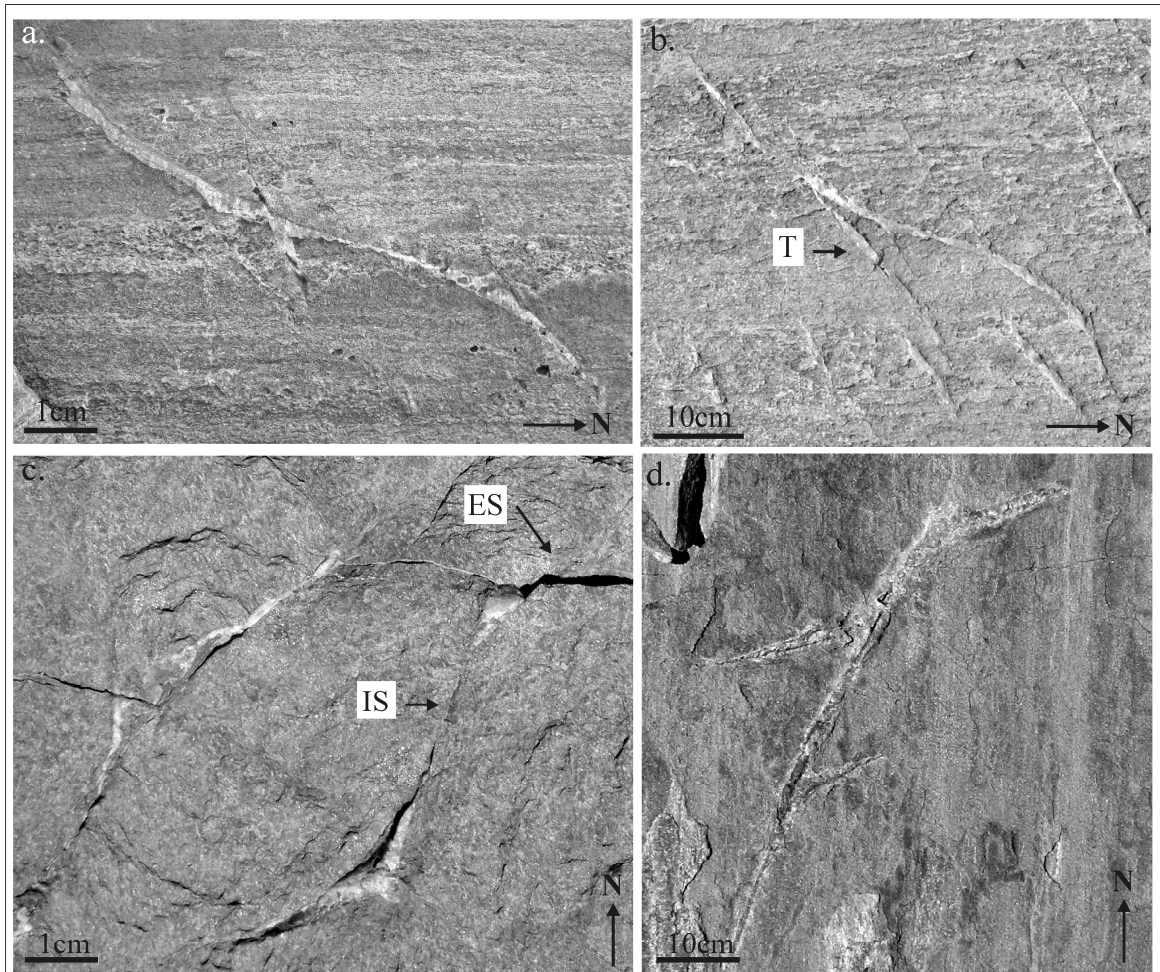
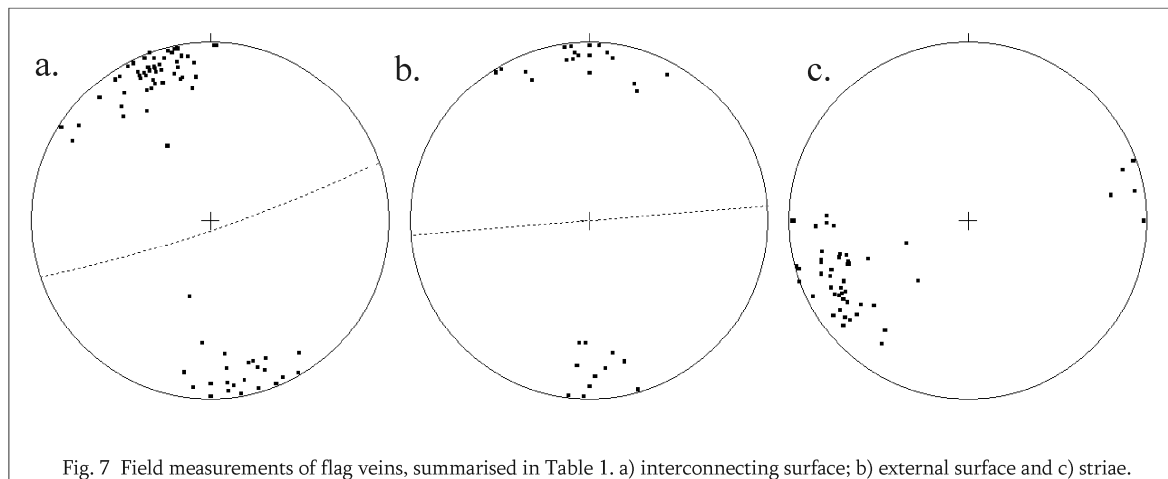


Fig. 6 Field examples of sigmoidal tension gashes (a,b) and pennant termination veins (c,d). T is tensional fracture (cf. Fig. 1); IS and ES are interconnecting and external surfaces. All photos parallel to foliation plane.

Sigmoidal veins (lines to L)	Tips			Centres		
	Av	$\sigma$	N	Av	$\sigma$	N
	77	20,2	96	34	16,5	52
Pennant veins (poles to planes)	Av ES	N	Av IS	N	Av Str	N
	175/90	34	161/85	82	247/17	54

Table 1 – Summary of field measurements on the two sets of veins. Av: Average; ES/IS: external/internal surface; Str: Striae; N: number of measurements.

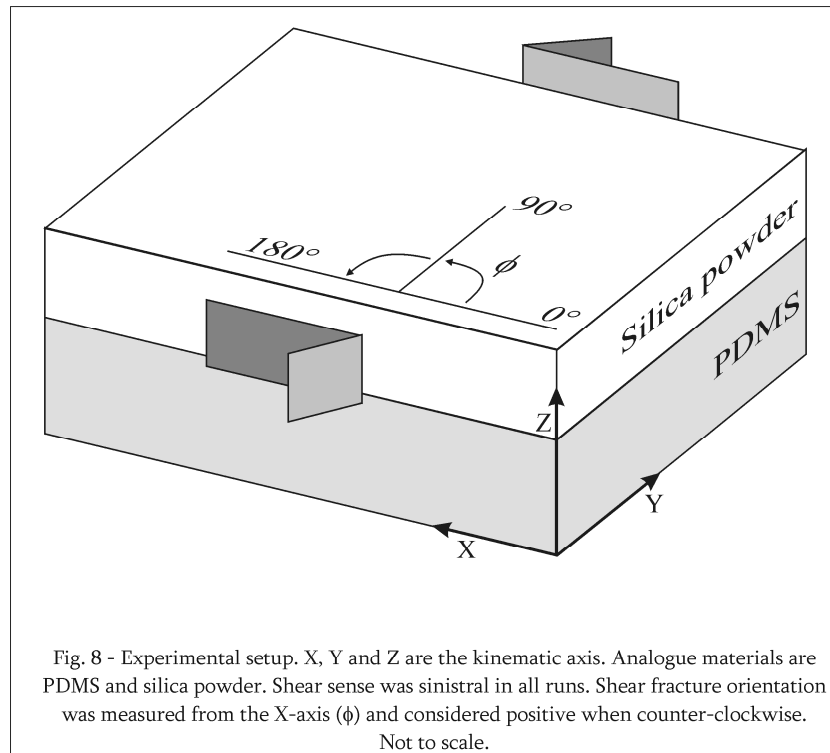


#### 4. Analogue modelling

Analogue experiments were carried out in a deformation rig described in Marques and Coelho (2001) and used subsequently in several other studies (eg Bose and Marques, 2004; Marques and Bose, 2004). This machine produces parallel-sided plane strain sinistral simple shear deformation imposed on the model by dislocation of one of the side walls. The far-field strain rate set by the machine was constant throughout the runs at  $10^{-3} \text{ s}^{-1}$ .

The experimental set up design (Fig. 8) was based on field observations and attempts to reproduce the geological setting of the veins as described above. It was assumed that the veins developed in non-coaxial flow, with vertical shear planes imposed on a horizontal or gently dipping foliation plane. The alternating micaschist / quartzite metasedimentary sequence is represented by two layers of different materials, transparent PDMS and white silica powder. PDMS (poly-dimethyl-siloxane, manufactured by Dow Corning of Great Britain under the trade name of SGM 36) is a polymer with Newtonian properties at room temperature, which has been extensively used in experimental modelling as analogue of viscous materials (see Weijermars, 1986 for properties). This material was used to simulate the micaschist layers, where fractures have not been observed, and was in complete adherence with the rig's side walls. On top of the PDMS (Fig. 8), a layer of fine-grained ( $20 \mu\text{m}$ ) silica powder was placed to represent the quartzite units. This material has cohesion of 300 Pa and fails according to a Coulomb criterion (Krantz, 1991). Similar powdered silica has been used as an analogue for the brittle upper crust in experiments by Galland et al. (2003). The silica powder layer was built by sieving with the help of a sugar sprinkler cooking device, from a height of about 10 cm. By using the same handling technique, physical properties of the silica powder such as density, cohesion and internal angle of friction are assured to remain similar in all runs (Krantz, 1991). The observation surface was imprinted with a grid of

markers in five of the experimental runs. These markers provided a gauge for dislocation (or slip) in the developing R/R' systems.



The boundary conditions imposed by the setup of the experiments specify that deformation is transmitted, point by point, to the silica powder from the PDMS underneath, not by push from the confining walls. The silica powder is unconfined in the vertical direction. The setup further determines that the simple shear plane is orthogonal to bedding, which is in good agreement with the fact that the field examples occur on the foliation plane.

The evolution of fracture orientation with progressive deformation is described by the angle  $\phi$ , measured between the fracture and the X-axis of finite strain (Fig. 8). Counter clockwise angles were considered positive; this corresponds to synthetic rotation of the fractures in the given sinistral shear sense. For every run the orientation of fracture sets was measured at shear strain gamma values of 0.125, 0.25, 0.5, 0.75 and 1.0  $\gamma$ . Although the rig is capable of attaining higher shear strains (up to  $12\gamma$ ), the experiments were limited to a maximum of 1.25  $\gamma$ . After this amount of shear strain, the observation surface was disrupted in such a way that it was virtually impossible to follow the evolution of individual sets of fractures any further. This is also the reason why the number of measurements in the latest stages of the experiments is less than for the initial part (Table 2): in numerous examples, the individual shear fractures were lost in the disrupted surface after a certain amount of deformation.

## 5. Experimental results

The results of 20 experimental runs are summarised in Table 2 and presented in graphical form in Fig. 9a. All angles were measured with respect to the shear zone boundary, represented in the analogue experiments by the shear rig wall.

The first noticeable effect of deformation in the silica powder was, in all runs, the development of R-R' shear fractures, either isolated or organised in conjugate sets, such as in Fig. 10i. Riedel shear fractures (R) appeared with an average orientation of 21°, whilst conjugate-riedel shear fractures (R') were as expected more steeply oriented, at ca. 73° (Table 2, Fig. 9a). The first measurement was made in all instances at 0.125  $\gamma$ , and it is therefore highly probable that these orientations have already a certain amount of rotation with respect to the original angle of the shear fracture at instantaneous deformation. Once established, the R- and R'-shear fractures follow different paths. R'-shear fractures experience consistent synthetical rotation, albeit about 5° less than expected for a material line with corresponding initial orientation (Fig. 9a). This is in agreement with the observation that shear strain is underestimated if calculated by the rotation of R'-shear structures, since other mechanisms, such as slip and rigid block rotation, may be present to accommodate deformation (Katz et. al., 2004).

Type	gamma	Average	$\sigma$	Max	Min	N
R	0,125 $\gamma$	21,69	5,63	36	10	57
	0,25 $\gamma$	24,13	7,05	46	10	109
	0,5 $\gamma$	28,70	8,06	59	8	128
	0,75 $\gamma$	34,02	10,85	69	14	119
	1 $\gamma$	37,58	13,66	66	12	74
	1,25 $\gamma$	37,00	12,79	71	22	29
R'	0,125 $\gamma$	73,45	6,83	87	54	122
	0,25 $\gamma$	78,84	7,38	99	57	136
	0,5 $\gamma$	91,13	9,64	111	65	144
	0,75 $\gamma$	105,08	10,61	126	77	127
	1 $\gamma$	114,90	9,66	138	96	79
	1,25 $\gamma$	119,86	7,95	138	105	39

Table 2 – Summary of the experimental results, shown by average and standard deviation. N is number of measurements, Max and Min are the maximum and minimum value.

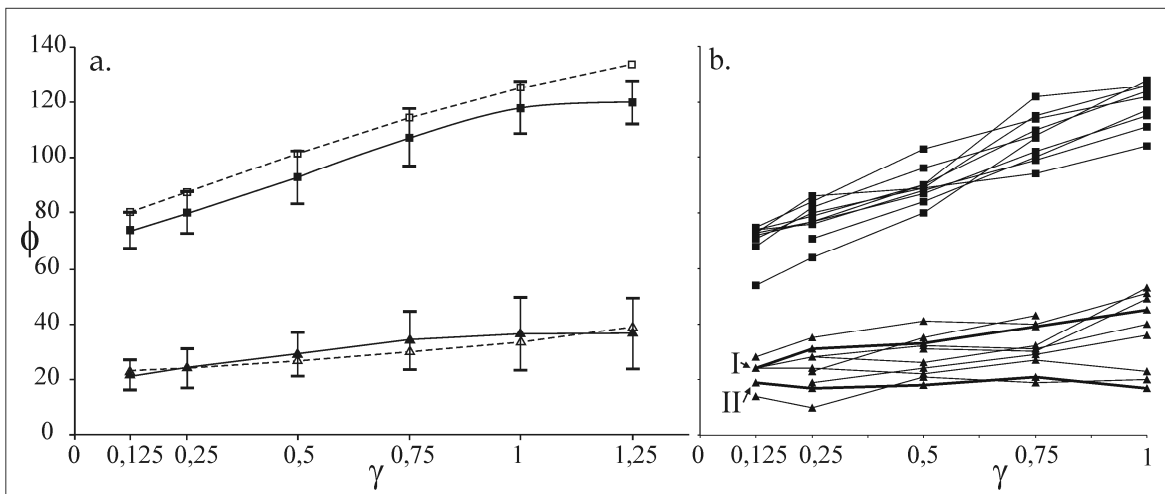


Fig. 9 - Evolution of shear fracture orientation as obtained in the experimental results. Closed squares and triangles represent experimental R'- and R-shears, respectively. a) average of 20 runs with standard deviation represented as error bars; open squares and triangles represent the orientation expected considering the rotation of a material line. b) Orientations measured in example run (#13). Bold lines I and II are individual fractures. See text for discussion.

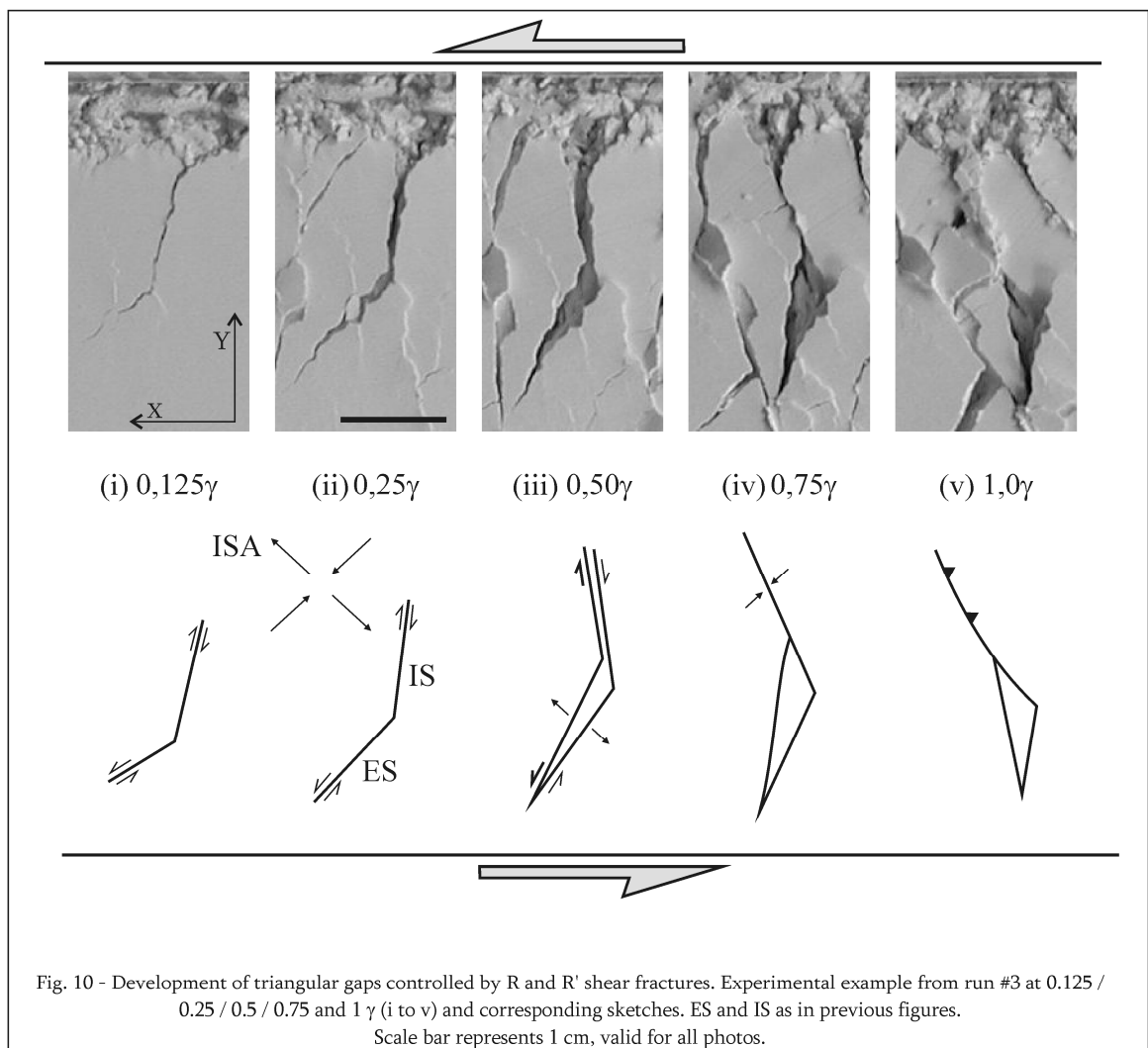


Fig. 10 - Development of triangular gaps controlled by R and R' shear fractures. Experimental example from run #3 at 0.125 / 0.25 / 0.5 / 0.75 and 1  $\gamma$  (i to v) and corresponding sketches. ES and IS as in previous figures. Scale bar represents 1 cm, valid for all photos.

R-shear fractures have a more variable behaviour and may or may not rotate continuously as their conjugate structures. Figure 9b represents an example run (#13) and although at first examination the rotation of the group might seem uniform, focussing on individual R-shear fractures shows intrinsic differences. Fracture I (Fig. 9b), for example, rotates synthetically, just as the R' counterparts, but fracture II, and several others, undergo limited rotation remaining within  $\pm 5^\circ$  of their initial orientation, with possible back rotation in some examples. A similar behaviour of R-shear fractures was reported by Swanson (1992) in analogue modelling with clay. This dual behaviour was observed in all runs and accounts for the increasing standard deviation values of R-shear fractures with progressive deformation (Table 1, Fig. 9a). Markers imprinted on the observation surface show that slip occurred in both R and R' and that these structures are mode II fractures (Fig. 11). The observed displacement is consistent with that expected for R-R' systems and can be an important criterion to distinguish modelled structures from previously described features (section 6.1). The amount of slip (displacement parallel to the fracture orientation) was measured, subsequently normalised considering the side of the grid as unit and plotted against rotation angles (Fig. 11a). Experimental results show that slip is inversely related to the amount of rotation: fractures that rotate more experience less slip. Conversely, fractures that rotated less, remained stable or back-rotated show more slip. In these cases, deformation was accommodated not by rigid rotation but mostly by displacement parallel to the fracture orientation. Figure 11a also shows that R and R' fractures that rotated continuously (I) show a smaller amount of slip compared to the R fractures which remained stationary or back rotated (II).

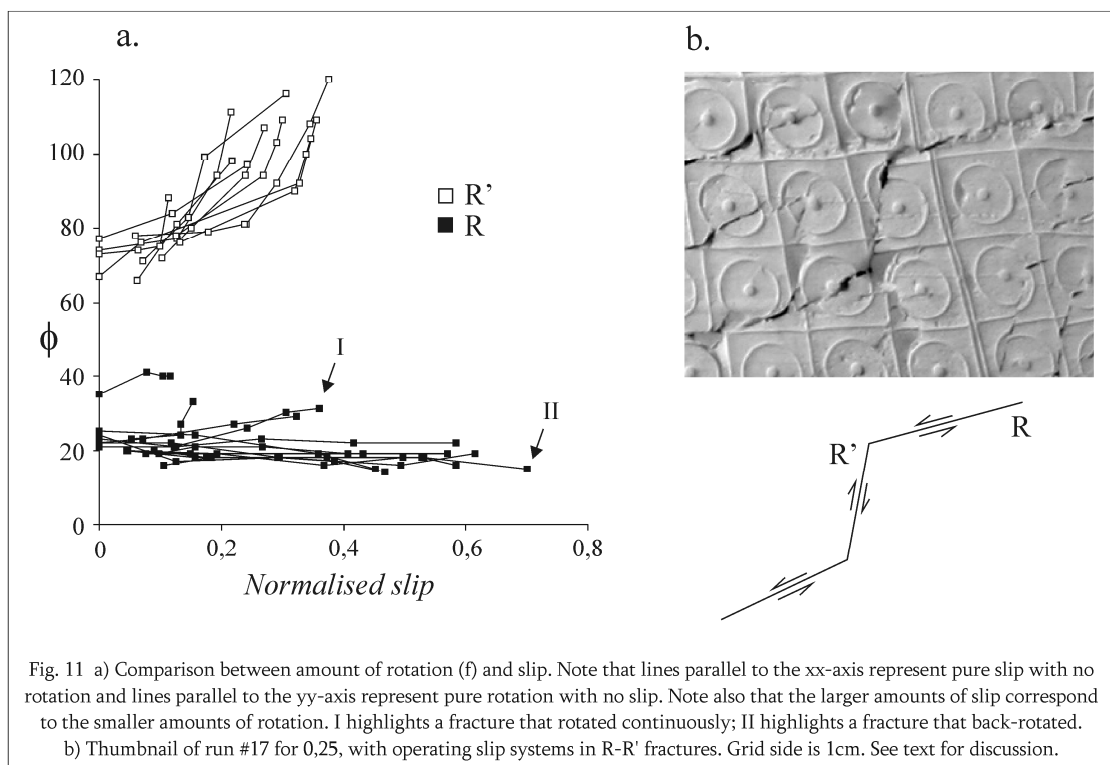


Fig. 11 a) Comparison between amount of rotation ( $\phi$ ) and slip. Note that lines parallel to the xx-axis represent pure slip with no rotation and lines parallel to the yy-axis represent pure rotation with no slip. Note also that the larger amounts of slip correspond to the smaller amounts of rotation. I highlights a fracture that rotated continuously; II highlights a fracture that back-rotated.  
b) Thumbnail of run #17 for 0,25, with operating slip systems in R-R' fractures. Grid side is 1cm. See text for discussion.

With progressive deformation, the slip systems operating in the obtuse angle between conjugate R-R' shear fractures induce slipping in opposed sense that develops into gaps with pennant shapes (Fig. 10), combined with shear fracture rotation. Converging slip sense explains why no gaps were observed in the acute angle between the shear conjugates. The opening is further enhanced by the orientation of the shear fractures with respect to the ISA. Since the experiments were performed under simple shear conditions, the ISA are known to be at angles of  $45^\circ$  (maximum shortening) and  $135^\circ$  (maximum stretching) with the flow plane (Fig. 10), thus favouring opening of the shear fractures in the first steps of deformation. When the fractures rotate enough, such as the R' that reach higher  $\square$ -values, they enter the shortening field and, instead of opening they become prone to shortening normal to the vein surface (Fig. 10iv,v). The pennant gaps however persisted in all runs, even when the R' shear fracture was in the shortening field. R' fractures oriented in this field often display minor thrusting of the right block over the left (Fig. 10v). The example of Fig. 10, although illustrative of the problem, represents the special case where both R- and R'-shear fractures rotate continuously. The majority of pennant gaps in the experiments however occur in the cases where the R'-shear rotates continuously whilst the R-shear tends to remain stable (Fig. 12a). R' shear fractures are usually considered to be relatively late and confined to the overlap areas of the dominant R- fractures in the general theoretical model of shear fractures (eg Ahlgren, 2001). However, in the present series of experiments, R'-fractures clearly dominated over R, suggesting that the subordinate role of R' is not a universal rule. Similar behaviour was already reported in previous studies based on field examples (eg Ahlgren, 2001; Katz et al., 2004).

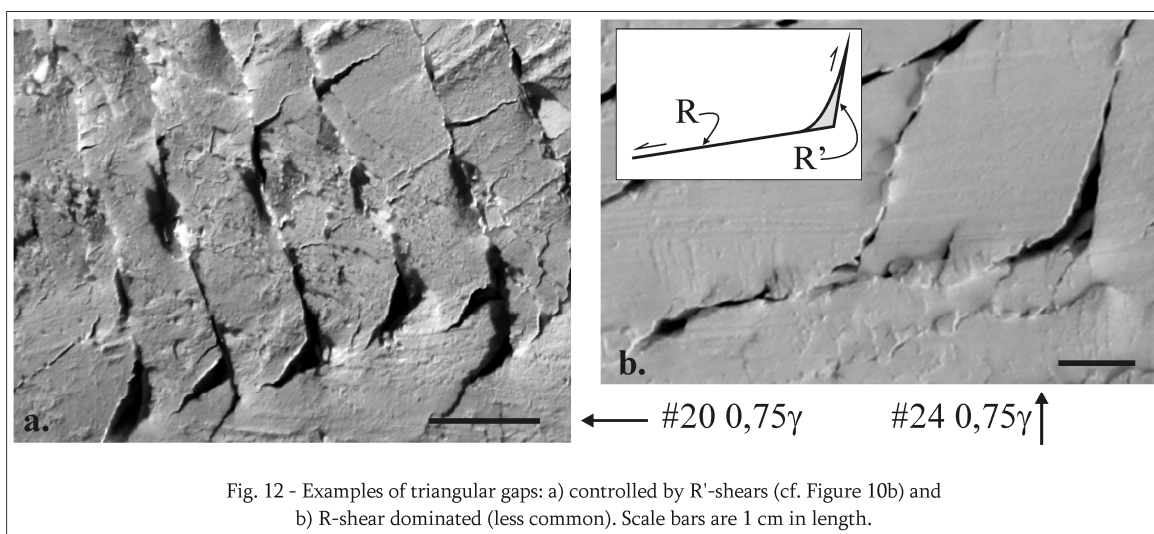


Fig. 12 - Examples of triangular gaps: a) controlled by R'-shears (cf. Figure 10b) and b) R-shear dominated (less common). Scale bars are 1 cm in length.

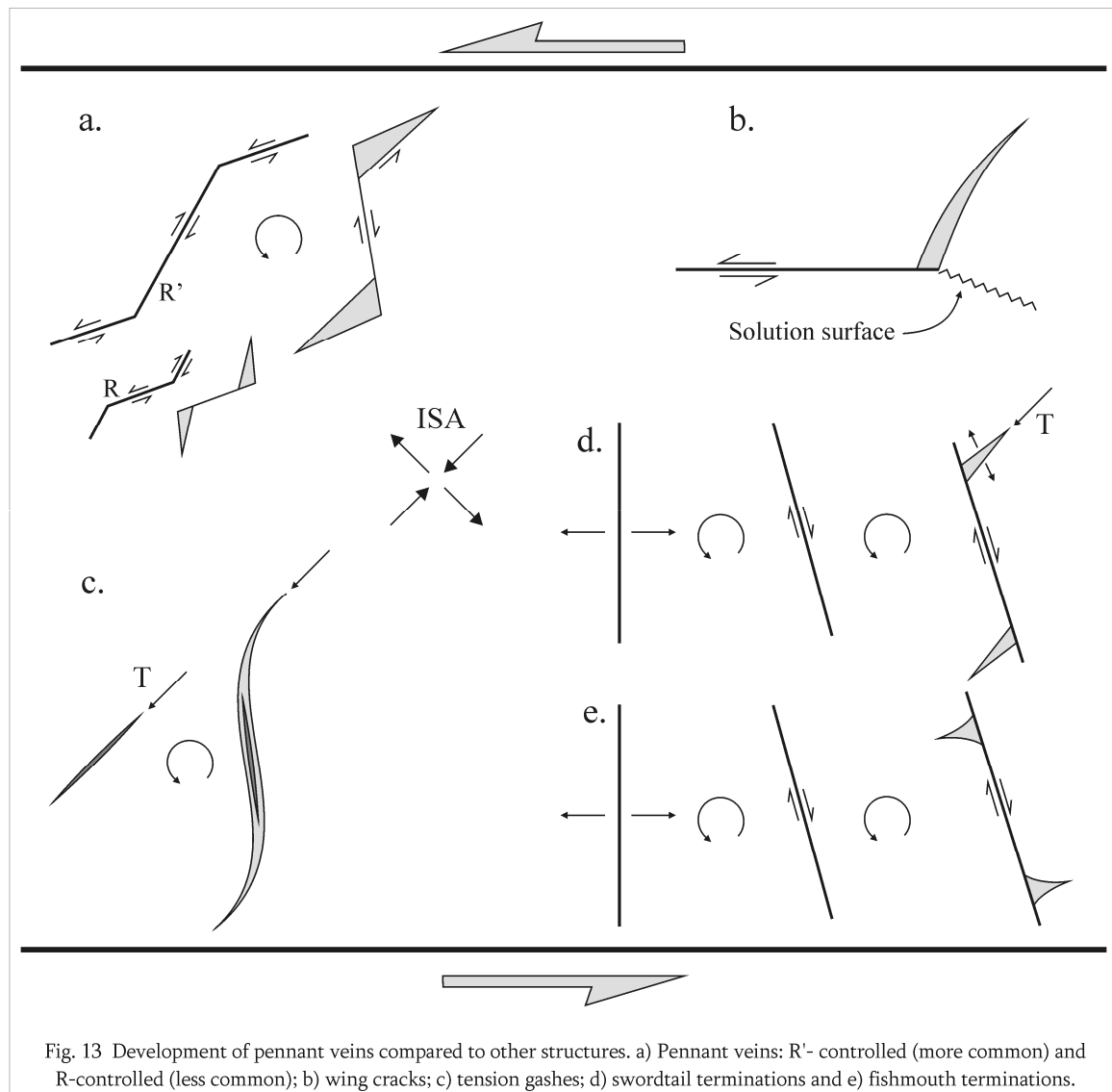
## 6. Interpretation and discussion

The gaps observed in the experimental runs (Fig. 10 and 12) and described in the previous section are interpreted here as the space available in Nature for the deposition of the pennant-shaped quartz veins observed in the field (Fig. 6c,d). As their analogue equivalents suggest, the geometry and orientation of the termination features, filled in Nature by quartz, are also controlled by the kinematics of R-R' shear fractures operating in the quartzite units.

### 6.1. Comparison of pennant veins

Wing cracks (Horii and Nemat-Nasser, 1985; Willemse and Pollard, 1998), splay fractures (Martell and Pollard, 1989; Cooke, 1997) or crack kinks (Nemat-Nasser and Horii, 1982; Cruikshank et al., 1991) are tension fractures associated with non-propagating fault or shear fracture terminations (Fig. 13). They are mode I features, but occur as a result of slipping on a parent mode II fracture. Wing cracks do not develop in the central region of a fault, where energy is accommodated best by propagation of slip patches (Martel and Pollard, 1989).

They are usually at a high angle to the parent fracture, dependent on the ratio between shear and normal stress, and variable between  $0^\circ$  (pure mode I) and about  $70^\circ$  (pure mode II) (Fig. 13b; Willemse and Pollard, 1998). Wing cracks are also commonly associated with solution surfaces oriented orthogonal to the cracks (Fig. 13b; Willemse and Pollard, 1998). With progressive deformation, wing cracks tend to acquire a curved horn shape, pointing towards the maximum shortening axis (Horii and Nemat-Nasser, 1985; Nemat-Nasser and Horii, 1982). From a geometric perspective, wing cracks are similar to pennant veins, especially the ones controlled by R-fractures (Fig. 12b). There are, however, important distinctions which make it necessary to define pennant veins as a separate category: 1) Wing cracks are extensional mode I features, without slip on their surface, whereas pennant veins develop by combined rotation of and displacement in R-R' mode II fractures (Fig. 11b). 2) The observed pennant veins are never associated with orthogonal solution surfaces or similar compression structures as wing cracks commonly are. If this was the case, the analogue examples would show perturbations on the surface at about  $90^\circ$  of the pennant termination, which are not present. 3) Wing crack orientation depends on the ratio between normal and shear stress, while pennant veins are controlled by R-R' conjugate fractures. 4) Pennant veins observed in the field and analogue experiments preserve their typical straight shape, unlike wing cracks that tend to develop arcuate geometries pointing towards the maximum shortening of the ISA.



Tension gashes (eg Ramsay and Huber, 1983; Olson and Pollard, 1991) are tension fractures opened parallel to the maximum instantaneous stretching direction (Fig. 13c). With progressive deformation, this fracture may be filled as a vein and undergo synthetic rotation with respect to the overall shear sense (Fig. 13c). Combined continuous growth results in a typical sigmoidal geometry that can be used as a shear sense indicator (eg Ramsay and Huber, 1983; Passchier and Trouw, 2005). Tension gashes may be distinguished from pennant veins as follows: 1) they are structurally controlled by tension fractures T instead of Riedel conjugate fractures; 2) they are mode I fractures without displacement parallel to the vein direction, whereas in pennant veins slip is present (Fig. 11b) and plays a major role in development of the veins (Fig. 10); 3) in the first increment of deformation tension gashes appear at an angle of ca. 45° with respect to a simple shear zone wall, while pennant external surfaces are either

considerably steeper (if controlled by R') or shallower (if controlled by R); 4) most tension gashes have a smooth, sigmoidal geometry, whereas pennant veins are always angular features.

Type I boudin parting surfaces (Hanmer, 1986) are pull-aparts developed normal to layering. With progressive deformation these surfaces rotate synthetically, producing antithetic slip with respect to the overall shear sense. According to Swanson (1992), these structures are privileged sites for the development of two types of asymmetric geometries, swordtail and fishmouth quartz-filled terminations (Fig. 14 in Swanson, 1992) which resemble pennant veins to some extent. Swordtail terminations are planar to arcuate fractures, developed in the extensional side of the boudin parting surface. In progressive deformation, the boudin parting surfaces rotate and oblique gash veins develop in their extensional side. Space available for quartz deposition in these oblique gashes is created by the slipping system operating in the boudin parting surface (Fig. 13d; Swanson, 1992). Fishmouth terminations result from the collapse of the contractional side of a boudin parting surface along a fault plane and disappear with further increments of deformation (Fig. 13e; Swanson, 1992); they can be easily distinguished from pennant veins by their contractional nature. Pennant veins are geometrically very similar to swordtail terminations and develop by the influence of slip on a pre-existing fracture. The difference resides in the type of fractures involved: swordtail terminations develop around tensional fractures (boudin parting surfaces and oblique gashes), whereas pennant veins are mode II fractures, opened by combined rotation and slip of R-R' conjugates.

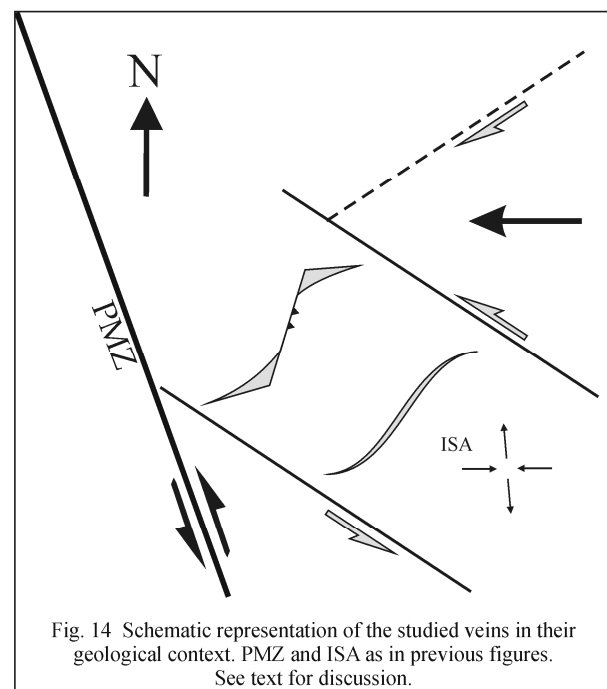
## 6.2. Kinematic interpretation

Gash-related features such as sigmoidal tension gashes, like the ones identified in the study area, or the swordtail terminations of Swanson (1992), are initially tensional fractures, parallel to the maximum shortening axis of the instantaneous stretching axes. In outcrop, these structures may present a distinctive sigmoidal shape where tips can be interpreted as gauges for the maximum shortening axis orientation (eg Ramsay and Huber, 1983). This observation allows sigmoidal tension gashes to be accurate shear sense indicators. The use of pennant veins as shear sense indicators is limited by their own characteristics. Since they develop on the extensional side of the shear fracture terminations, a statistical study of pennant vein orientation in outcrop can be used to estimate the location of the extension field of deformation. This, combined with other criteria such as boudin trails or folds, may be of use to determine shear sense. However, it is important to stress again that they are not parallel to the maximum shortening axis of the ISA, as the tips of tension gashes are, and therefore cannot be interpreted as indicators of this bulk flow element. The external surface of the pennant termination vein (Fig. 10) is controlled by the R-shear fracture, or less commonly by R' (Fig. 12), and shows the orientation of these

features in a given stage of deformation. This information is difficult to use in kinematic interpretation because both R- and R'-shear fractures are expected to undergo rotation throughout progressive deformation and the specific amount of shear strain is usually unknown in natural examples. Moreover, the initial orientation of R- and R'-shear fractures is highly dependent on the rheological properties of the rock, namely the internal angle of friction and pore fluid pressure.

### 6.3. Contribution to regional geology

The style of development of the observed sets of sigmoidal tension gashes and pennant veins (Fig. 5) are the only field evidence that deformation in the Orupembe area continued into a stage of brittle deformation after the development of the mylonitic lineations and foliations. This deformation is late or at least coeval with the latest stages of the M2 wrench stage that produced the main fabric due to: 1) the fact that the sigmoidal veins cut and deflect the main lineation and 2) the metamorphic grade of the quartz veins that, according to their brittle nature, is lower than the upper greenschist /



amphibolite facies of the main lineation (Goscombe et al. 2003b). What are the characteristics of the deformation that produced the veins? As an answer to this question, pennant veins are not very informative because, as seen in the analogue modelling, the amount of rotation of the R/R' shear fractures is high even in the first steps of deformation. Moreover, in field example the initial orientation of the R/R' shear fractures is unknown and, since the veins occur on the foliation plane, the direction of the shear plane is also undefined. Sigmoidal veins also occur on the foliation plane, but they give important information about flow kinematics since the known tip orientation of these veins indicates the maximum shortening ISA, which is, in simple shear, related to the shear plane by an angle of 45°. Their field orientation suggests the existence of a WNW-ESE trending sinistral ductile simple shear zone, or general transpression with ISA at 70° to the PSZ affecting the entire Orupembe area and overprinting the previous strike-slip pattern (Fig. 14). This solution is in good agreement with the field characteristics of the pennant veins, since pennant terminations are in the extensional quadrant as predicted by the

analogue modelling. WNW-ESE sinistral shear also justifies the down-to-the-south displacement shown by the striae observed in the interconnecting surfaces of the pennant veins (Fig. 5). On a regional scale, the WNW-ESE sinistral shear can be interpreted as associated with the E-W shortening responsible for the large scale folding. Both sets of veins are ascribable to the convergent stage of M2 (M2c) and therefore late with respect to the main wrench stage that produced the lineation. The fact that sigmoidal veins deflect the main lineation and that both sets develop under retrograde metamorphic conditions further support this conclusion. Crenulation cleavage and lineations parallel to early M2w lineations is present in the micaschist interbeds and the associated folding is only visible on map scale, but the sigmoidal and pennant veins are the only mesoscopic evidence of M2c present in the quartzitic layering of the study area.

## *7. Conclusions*

This chapter introduced pennant veins, a new type of vein geometry with a geometry similar to established types such as sigmoidal tension gashes, wing cracks and wordtail and fishmouth termination veins. Analogue modelling has shown that pennant terminations are controlled by the kinematics of Riedel conjugate sets of fractures. The space available for vein deposition is obtained by combined rotation of and slip in the operating shear fractures. The orientation of pennant terminations is expected to be in the extensional quadrant of the bulk flow and, if combined with other criteria, can be used as a shear sense indicator. Care has to be taken, however, to distinguish between R-dominated and R' dominated veins in such cases. However, neither the interconnecting nor the external surfaces of pennant veins correspond to the maximum shortening direction of the ISA as in tension gashes, but depend on the orientation of the R/R' conjugate set in a given moment of deformation. This observation, together with the uncertainty of the amount of rotation of shear fractures in natural examples, hinders the use of pennant veins as reliable gauges for bulk flow.

## References

- Ahlgren, S.G., 2001. The nucleation and evolution of Riedel shear zones as deformation bands in porous sandstone. *Journal of Structural Geology* 23, 1203-1214.
- Bartlett, W.L., Friedman, M., Logan, J.M., 1981. Experimental folding and faulting of rocks under confined pressure. Part IX. Wrench faults in limestone layers. *Tectonophysics* 79, 255-277.
- Bons, P.D., 2000. The formation of veins and their microstructures. In: Jessel, M.W., Urai, J.L. (Eds.) *Stress, strain and structure, a volume in honour of W.D. Means*. *Journal of the Virtual Explorer*, 2.
- Bose, S., Marques, F. O., 2004. Controls on the geometry of tails around rigid circular inclusions: insights from analogue modelling in simple shear. *Journal of Structural Geology* 26, 2145-2156.
- Braun, J., 1994. Three-dimensional numerical simulations of crustal scale wrenching using a non-linear failure criterion. *Journal of Structural Geology* 16, 1173-1186.
- Cloos, E., 1955. Experimental analysis of fracture patterns. *Geological Society of America Bulletin* 66, 241-256.
- Coelho, S., Passchier C.W., Grasemann, B., 2005. Geometric description of flanking structures. *Journal of Structural Geology* 27, 597-606.
- Cooke, M.L., 1997. Fracture localization along faults with spatially varying friction. *Journal of Geophysical Research* 102, 22425-22434.
- Cruikshank, K.M., Zhao, G., Johnson, A.M., 1991. Analysis of minor fractures associated with joints and faulted joints. *Journal of Structural Geology* 13, 865-886.
- Davis, G.H., Bump, A.P., Garcia, P.E., Ahlgren, S.G., 1999. Conjugate Riedel deformation band shear zones. *Journal of Structural Geology* 22, 169-190.
- Dresen, G., 1991. Stress distribution and the orientation of Riedel shears. *Tectonophysics* 188, 239-247.
- Galland, O., de Bremond d'Ars, J., Cobbold, P.R., Hallot, E., 1999. Physical models of magmatic intrusion during thrusting. *Terra Nova* 15(6), 405-409.
- Goscombe, B., Hand, M., Gray, D., 2003a. Structure of the Kaoko Belt, Namibia: progressive evolution of a classic transpressional orogen. *Journal of Structural Geology* 25, 1049-1081.
- Goscombe B., Hand M., Gray D., Mawby, J., 2003b. The metamorphic architecture of a transpressional orogen: the Kaoko Belt, Namibia. *Journal of Petrology* 44, 679-711.
- Goscombe, B., Gray, D., Hand, M., 2005a. Extrusional Tectonics in the Core of a Transpressional Orogen: the Kaoko Belt, Namibia. *Journal of Petrology* 46, 1203-1241
- Goscombe, B., Gray, D., Armstrong, R., Foster, D.A., Vogl, J., 2005b. Event geochronology of the Pan-African Kaoko Belt, Namibia. *Precambrian Research* 140, 103.e1-103-e.41.
- Hanmer, S., 1986. Asymmetrical pull-aparts and foliation fish as kinematic indicators. *Journal of Structural Geology* 8, 111-115.
- Hilgers, C., Urai, J.L., 2002. Microstructural observations on natural syntectonic fibrous veins: implications for the growth process. *Tectonophysics* 352, 257-274.
- Hoffman, P.F., Swart, R., Freyer, E.E., Guowei, H., 1994. Damara Orogen of Northwest Namibia. In: Niall, M., McManus, C. (Eds.), *Geological Excursion Guide of the international conference Proterozoic crustal and metallogenetic evolution*. Geological Society and Geological Survey of Namibia. 55 pp.

- Horii, H., Nemat-Nasser, S.J., 1985. Compression-induced microcracks growth in brittle solids: axial splitting and shear failure. *Journal of Geophysical Research* 90, 3105-3125.
- Jiang, D., Williams, P.F., 1998. High strain zones: a unified model. *Journal of Structural Geology* 20, 1105-1120
- Katz, Y., Weinberger, R., Aydin, A., 2004. Geometry and kinematic evolution of Riedel shear structures, Capitol Reef National Park, Utah. *Journal of Structural Geology* 26, 491-501.
- Köhn, D., Hilgers, C., Bons, P.D., Passchier, C.W., 2000. Numerical simulations of fibre growth in antitaxial strain fringes. *Journal of Structural Geology* 22, 1311-1324.
- Konopásek, J., Kröner, S., Kitt, S.L., Passchier, C.W., Kröner, A., 2005. Oblique collision and evolution of large-scale transcurrent shear zones in the Kaoko belt, NW Namibia. *Precambrian Research* 136, 139-157.
- Krantz, R.W., 1991. Measurements of friction coefficients and cohesion for faulting and fault reactivation in laboratory models using sand and sand mixtures. In: P.R. Cobbold (Editor), *Experimental and Numerical Modelling of Continental Deformation*. *Tectonophysics* 188, 203-207.
- Marques, F.O., 2001. Flow and fracturing of clay: analogue experiments in pure shear. *Geol. Soc. of Am. Bulletin, Memoir 193: Tectonic Modeling: A Volume in Honor of Hans Ramberg*, 261-270.
- Marques, F.O., Coelho, S., 2001. Rotation of rigid elliptical cylinders in viscous simple shear flow: analogue experiments. *Journal of Structural Geology* 23, 609-617.
- Marques, F.O., Bose, S., 2004. Influence of a permanent low-friction boundary on rotation and flow in rigid inclusion/viscous-matrix systems from an analogue perspective, *Tectonophysics* 382, 229-245.
- Martel, S.J., Pollard, D.D., 1989. Mechanics of slip and fracture along small faults and simple strike-slip fault zones in granitic rock. *Journal of Geophysical Research* 94, 9417-9428.
- McKinnon, S.D., Garrido de la Barra, I., 1998. Fracture initiation, growth and effect on stress field: a numerical investigation. *Journal of Structural Geology* 20, 1673-1689.
- Moore, D.E., Byerlee, J., 1992. Relationships between sliding behaviour and internal geometry of laboratory fault zones and some creeping and locked strike-slip faults of California. *Tectonophysics* 211, 305-316.
- Moore, J.M., 1979. Tectonics of the Najd transcurrent fault system, Saudi Arabia. *Journal of the Geological Society of London* 136, 441-454.
- Naylor, M.A., Mandl, G., Sijpesteijn, C.H.K., 1986. Fault geometries in basement-induced wrench faulting under different initial stress states. *Journal of Structural Geology* 8, 737-752.
- Nemat-Nasser, S., Horii, H., 1982. Compression induced nonplanar crack extension with application to splitting, exfoliation and rockburst. *Journal of Geophysical Research* 87, 6805-6821.
- Olson, J.E., Pollard, D.D., 1991. The initiation and growth of en echelon veins. *Journal of Structural Geology* 13, 595-608.
- Passchier, C.W., Trouw, R.A.J., 2005. *Microtectonics*. Second Edition. Springer-Verlag.
- Passchier, C.W., Trouw, R.A.J., A. Ribeiro, A., Paciullo, F.V.P., 2002. Tectonic evolution of the southern Kaoko belt, Namibia. *Journal of African Earth Sciences* 35, 61-75.
- Ramsay, J.G., Huber, M.I., 1983. *The Techniques of Modern Structural Geology*. Volume 1: Strain Analysis. Academic Press, London.
- Riedel, W., 1929. Zur Mechanik geologischer Brucherscheinungen. *Zentralbl. Mineral. Abt.* 354-368.

- Schreus, G., 1994. Experiments on strike-slip faulting and block rotation. *Geology* 22, 567-570.
- Smith, J.V., Durney, D.W., 1992. Experimental formation of brittle structural assemblages in oblique divergence. *Tectonophysics* 216, 235-253.
- Swanson, M.T., 1992. Late Acadian-Alleghian transpressional deformation: evidence from asymmetric boudinage in the Casco Bay area, coastal Maine. *Journal of Structural Geology* 14, 323-341.
- Tchalenko, J.S., 1968. The evolution of kink bands and the development of compression textures in sheared clays. *Tectonophysics* 6, 159-174.
- Weijermars, R., 1986. Flow behaviour and physical chemistry of bouncing putties and related polymers in view of tectonic laboratory applications. *Tectonophysics* 124, 325–358.
- Wilcox, R.E., Harding, T.P., Seely, D.R., 1973. Basic wrench tectonics. *The American Association of Petroleum Geologists Bulletin* 57, 74-96.
- Willemsse, E.J.M., Pollard, D.D., 1998. On the orientation and patterns of wing cracks and solution surfaces at the tips of a sliding flaw or fault. *Journal of Geophysical Research* 103, 2417-2438.



# Chapter III - Mohr-cyclides: a 3D representation of geological tensors.

## *1. Introduction*

### 1.1. Historical Background

Mohr diagrams, one of the most used and useful tools in structural geology, were introduced by German scientist Otto Mohr (1882). As a civil engineer, Mohr was especially interested in mechanical forces acting on planes and, thus, presented the scientific community with a graphical representation for three-dimensional stress, plotting normal stress ( $\sigma_n$ ) versus shear stress ( $\tau$ ). The result was the familiar Mohr diagram for stress, consisting of the three principal circles of stress and the surface they encompass, where any plane P can be plotted and assigned values for  $\sigma_n$  and  $\tau$ , with its orientation given in terms of single or double angles. This graphical representation has since been used extensively in empirical mechanical problems, either using failure envelopes or as a tool to study fracture opening and reactivation (Delaney et al., 1986; Jolly and Sanderson, 1997).

The Mohr-circle concept was adapted for strain tensors by Nadai (1950), who devised a graphical representation of quadratic elongation versus shear strain, where angles between lines are plotted in the unstrained form. The plot is in all ways similar to Mohr's diagram and establishes a parallel between the principal circles of stress and the principal sections of the deformation ellipse. Nadai (1950) also defined a Mohr diagram for reciprocal strain, with reciprocal quadratic elongation versus reciprocal shear strain.

Mohr diagrams were formally introduced to structural geology by Brace (1961), who coined the term and explored its multiple applications in the study of deformed rocks. This new line of research was not lost and Ramsay (1967) further expanded the relevance of Mohr diagrams in strain analysis, showing that Mohr circles for reciprocal strain could be used to estimate strain ellipses. Means (1982) introduced the Mohr diagram for the stretch tensor, where he explored the potential of polar coordinates and its applications to the study of material line behaviour, encompassing both rotational characteristics and stretch. This new method represented a significant departure from the previously published material, since the Cartesian coordinates were substituted by their polar counterparts in the interpretation of the Mohr diagram. In the following years, further research developed numerous applications of Mohr diagrams for strain to structural geology problems, namely inhomogeneous deformation (Means, 1983),

strain refraction (Means, 1983; Treagus, 1983), strain analysis (Treagus, 1986; Lisle and Ragan, 1988; Passchier, 1990a; Treagus 1990; Simpson and De Paor, 1993; Vissers, 1994; Zhang and Zheng, 1997) and vorticity analysis (Passchier and Urai, 1988; Passchier, 1990b). The pole of the Mohr diagram, although already in use in the engineering community since Drucker (1967), was introduced to structural geology by Ragan (1973), discussed by Cuttler and Elliott (1983) and formally defined by Allison (1984). De Paor and Means (1984) summarised tensor operations of Mohr diagrams and attempted to unify conflicting sign conventions, by defining Mohr circles of the First and Second Kind. Mohr diagrams for flow (velocity gradient) tensors were introduced by Lister and Williams (1983), following an idea of J.P. Platt. Since then, works like Means (1983), Bobyarchick (1986), Passchier (1986; 1987; 1988; 1993), Wallis (1992), Simpson and De Paor (1993) showed how these diagrams could be used to interpret and understand the principles of progressive deformation.

## 1.2. Tensors and Mohr-circles

As demonstrated first by Otto Mohr (1882), all tensors can be represented by Mohr diagrams. The relationship between a tensor  $\mathbf{T}_{ij}$  and its Mohr-circle can be illustrated using a second-rank tensor, which requires 4 components in a two-dimensional space (Fig.1). Considering a 2D coordinate system, the vertical axis  $T_{ij}$  is used to plot tensor components  $T_{12}$  and  $T_{21}$ , whereas horizontal coordinates stand for the  $T_{ii}$  components,  $T_{11}$  and  $T_{22}$ . Thus, two points can be plotted (Means, 1982):

$$x_1 \text{ as } (T_{11}, -T_{21}) \text{ and } x_2 \text{ as } (T_{22}, T_{12}).$$

Either the  $T_{12}$  or the  $T_{21}$  sign has to be changed from the original tensor components to insure equivalence of positions above or below the horizontal axis of the Mohr diagram. The convention of Means (1982) considers  $-T_{21}$ , and defines Mohr-diagrams of the *first kind* (De Paor and Means, 1984). If, on the other hand, one considers  $-T_{12}$ , the Mohr-diagram is said to be of the *second kind* (De Paor and Means, 1984). Points  $x_1$  and  $x_2$  define a diameter (dashed line) of a circle, which represents the Mohr-circle of tensor  $\mathbf{T}_{ij}$  (Fig.1). Any given tensor can be described by an infinite number of sets of  $\mathbf{T}_{ij}$  components, each representing a description of the tensor in a specific reference frame. Just like any circle can be defined by one of an infinite number of diameters, which correspond to the infinite

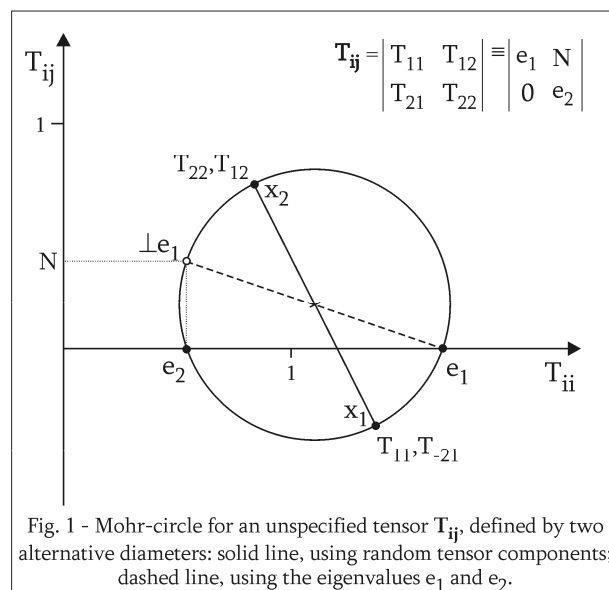


Fig. 1 - Mohr-circle for an unspecified tensor  $\mathbf{T}_{ij}$ , defined by two alternative diameters: solid line, using random tensor components; dashed line, using the eigenvalues  $e_1$  and  $e_2$ .

number of ways how reference axis can be selected (Fig.1). The coordinates points  $x_1, x_2$  represent a diameter defined by one set of four components of the tensor. Since there are infinite diameters, there are infinite sets and, thus, a Mohr circle can be defined as “(...) *the geometrical locus of all possible sets of tensor components*” (Means 1992).

Second-rank tensors in three dimensions, with 9 components, can also be represented by Mohr-circles. The easiest way to do this is to consider only part of the full tensor. A good example of this “technique” is the literature published on velocity gradient tensors, which, for Mohr-diagram purposes, simplifies flow to monoclinic geometries, characterised by the vorticity vector parallel to one of the eigenvectors and one of the instantaneous stretching axes. Assuming this, a tensor

$$T_{ij} = \begin{vmatrix} T_{11} & T_{12} & 0 \\ T_{21} & T_{22} & 0 \\ 0 & 0 & T_{33} \end{vmatrix} \quad \text{can be reduced to} \quad T_{ij} = \begin{vmatrix} T_{11} & T_{12} \\ T_{21} & T_{22} \end{vmatrix}$$

and plotted straightforward as a Mohr-circle, ignoring the three-dimensional component given by  $T_{33}$ . A second method to do this was suggested by Otto Mohr himself, for the case of Stress, applied later for quadratic deformation. The stress (deformation) tensor is written as a diagonal matrix, where  $T_{ii}$  are the eigenvectors of the tensor and the principal stresses  $\sigma_1, \sigma_2, \sigma_3$  (for instance Fig.3 below), or the principal quadratic elongations  $\lambda_1, \lambda_2, \lambda_3$ . These components are then used to draw three circles, of half-circles, that represent the principal sections of the stress or finite strain ellipsoid.

### 1.3. Scope

However ingenious, Mohr-circles for second-rank tensors remain simplifications because Mohr-space is always considered to be two-dimensional. This means that in order to accommodate a three-dimensional second-rank tensor in Mohr-space, it must be partitioned in three two-dimensional second-rank tensors, resulting in a combination of three Mohr-circles. In the literature the term “two-dimensional Mohr diagram” (one circle) is often used for 2D second-rank tensors and “three-dimensional Mohr diagram” (three circles) for 3D second-rank tensors. It is important, though, to point that in both cases tensors are plotted as circles in a 2D Cartesian space. In other words, the so called “three-dimensional circles” for stress are, in fact, the eigenvector sections of a second-rank symmetric tensor.

The purpose of this chapter of my PhD thesis is to investigate the possibility of expanding the representation of tensors in to a three-dimensional Mohr-space, using the examples of stress, flow and deformation. After some initial testing, it turned out that real three-dimensional Mohr-diagrams do exist and are represented by surfaces of the cyclide family and related toroids. These surfaces share all the

useful properties of 2D Mohr-diagrams, with the advantage of a full three-dimensional geometry. They will be henceforth referred to as *Mohr-cyclides*.

The symbols and conventions used on this chapter are listed in Table 1.

Table 1 - Symbols and notations used in Chapter III. In a few cases the same letter has different meanings, although in completely different contexts.

$\mathbf{T}_{ij}$	An unspecified tensor
$T_{ij}$	Tensor components
$\mathbf{R}_{ij}$	Rotation tensor
$A, B, C, D, E$	Cyclide parameters
$\theta, \psi$	Cyclide angles (long, lat)
$xx, yy, zz$	General xyz reference frame (in text)
$X_M, Y_M, Z_M$	Coordinates of a point in Mohr space
$i, j, k$	(Subscripted) Unspecified components or reference frame
//	Parallel to
$\perp$	Orthogonal to
$\mathbf{S}_{ij}$	Stress tensor
$\sigma_1, \sigma_2, \sigma_3$	Principal stresses (max, int, min)
$P, N_P$	Plane P, pole to P
$\sigma, \sigma_n, \tau$	Stress and its normal and shear components
$\sigma_{nP}, \tau_P$	Normal and shear stress on P
$\varphi$	$\sigma \wedge \sigma_n$
$S, N_S$	Stress plane and its pole
$\delta$	$N_S \wedge \sigma_1$
$\alpha$	$N_P \wedge \sigma_1$
$\beta$	$N_P \wedge \sigma_2$
$\gamma$	$N_P \wedge \sigma_3$
$\mathbf{L}_{ij}$	Flow tensor
$e, \hat{e}$	Eigenvectors of $\mathbf{L}_{ij}$ (the flow apophysis), eigenvalues
$\mathbf{D}_{ij}$	Stretching rate tensor: stretching component of $\mathbf{L}_{ij}$
$ISA_{1,2,3}$	Instantaneous stretching axes; eigenvectors of $\mathbf{D}_{ij}$
$\dot{s}_{1,2,3}$	Instantaneous stretching rates; eigenvalues of $\mathbf{D}_{ij}$
$\mathbf{W}_{ij}$	Vorticity tensor: rotational component of $\mathbf{L}_{ij}$
$v, \omega$	Velocity, angular velocity
$\bar{w}; \bar{w}; w_i$	Vorticity vector with respect to ISA; its magnitude; its components
$\bar{W}; \bar{W}$	Vorticity vector with respect to reference frame, its magnitude
$W_T$	Truesdell's vorticity number
$W'$	Spin component
$W_K$	Sectional vorticity number
$A_K$	Sectional dilatancy number
$T_K$	Sectional extrusion number
$V_K$	Volumetric change number
$\dot{\omega}$	Rate of angular velocity
$\dot{s}$	Stretching rate at point $m$
$\bar{s}$	Mean stretching rate in the section normal to vorticity

$\mathbf{l}_i$	Lines of no instantaneous stretch
$\chi$	$\mathbf{l}_i \wedge \mathbf{l}_j$ ( $\cos \chi = A_{\mathbf{k}}$ )
$v$	$e_j \wedge e_k$ ( $\cos v = W_{\mathbf{k}}$ )
$\vec{m}$	Position vector of point $m$ in the velocity field
$\vec{m}'$	Position vector of $m$ after 1 unit of time
$\eta_i$	$\dot{m} \wedge \text{ISA}_i$
$\dot{d}, \bar{d}$	rate of displacement vector, its magnitude
$U$	Pole of $\vec{m} - \dot{d}$ plane
$\varphi$	$\vec{m} \wedge \dot{d}$
$\delta$	$U \wedge \vec{w}$ (parallel to one eigenvector)
$\mathbf{F}_{ij}$	Direct deformation tensor
$\mathbf{H}_{ij}$	Reciprocal deformation tensor
$\mathbf{G}_{ij}$	Green tensor
$\mathbf{C}_{ij}$	Cauchy tensor
$k, k'$	Material line, deformed
$k_0, k_r$	Initial and final lengths of $k$
$S, S'$	Stretch of a line, reciprocal
$\hat{e}, \hat{e}'$	Elongation, reciprocal
$\lambda, \lambda'$	Quadratic elongation, reciprocal
$\phi_k$	Rotation angle ( $k \wedge k'$ )
$\gamma$	Shear strain
$\gamma'$	Gamma prime
$\theta_k$	$k \wedge xx$ -axis
$\nu_k$	$k \wedge yy$ -axis
$\omega_k$	$k \wedge S_1$ (principal axis of strain ellipse)

#### 1.4. Some properties of cyclides

A general cyclide is a non-spherical fourth degree surface, introduced by Dupin (1822), which can be defined in the canonical form by an implicit equation:

$$(x^2 + y^2 + z^2 - D^2 + B^2)^2 = 4(Ax - CD)^2 + 4(By)^2 \quad (\text{Eq.1})$$

or a parametric system (eg Pratt, 1990; Fig.2a):

$$\begin{aligned} x &= \frac{B \sin \psi (C \cos \theta - D)}{A - C \cos \theta \cos \psi} \\ y &= \frac{D(C - A \cos \theta \cos \psi) + B^2 \cos \theta}{A - C \cos \theta \cos \psi} \quad \text{with} \quad \begin{array}{l} \theta \geq 0^\circ \\ \psi \leq 180^\circ \end{array} \quad (\text{Eq.2}) \\ z &= \frac{B \sin \theta (A - D \cos \psi)}{A - C \cos \theta \cos \psi} \end{aligned}$$

where  $A$ ,  $B$ ,  $C$  and  $D$  are constant parameters, with  $B^2 = A^2 - C^2$ . The relative magnitude of parameters  $A$ ,  $C$  and  $D$  ( $B$  is always dependent) defines the shape of the surface in the cyclide family (Table 2; Fig.2; Shene, 2000). As seen below, this work will focus mainly on single-crescent cyclides and torii with converging points. Some other cyclide properties are (Allen and Dutta, 1997; Shene, 2000; Fig.2):

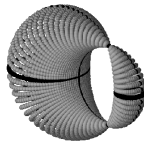
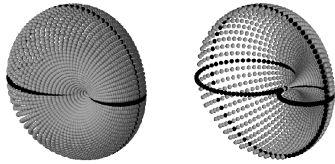
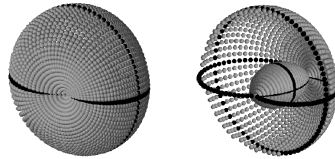
#1: All lines in the curvature of the cyclide, defined by equal values of  $\theta$  or  $\psi$ , are circles.

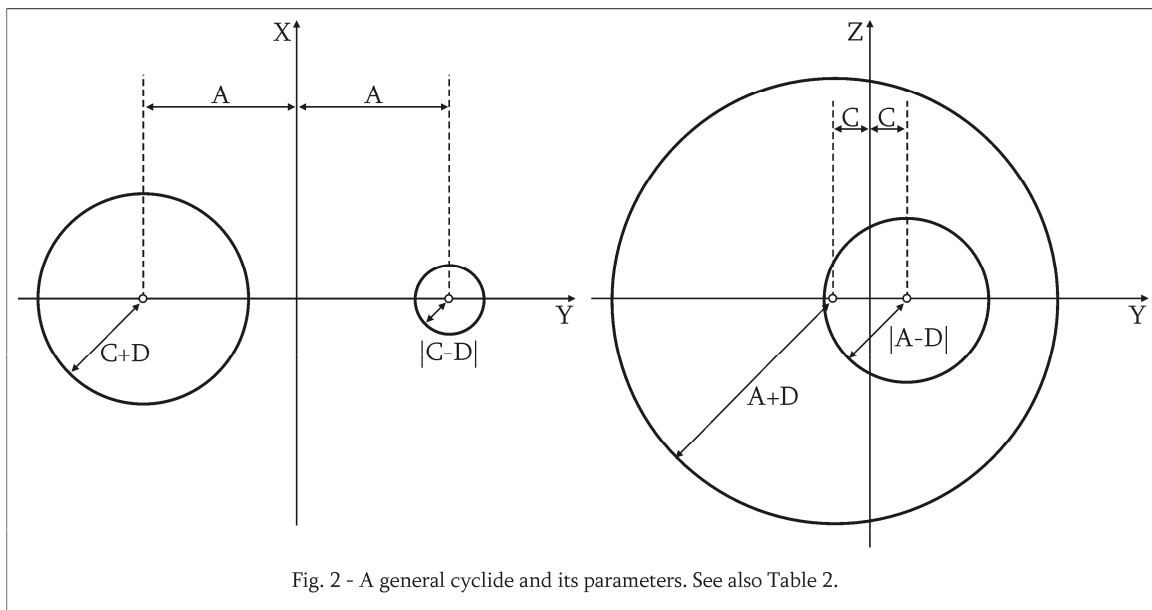
#2: A cyclide has two orthogonal planes of symmetry.

#3: The cyclide is fully defined by four major circles, two in each symmetry plane, given by:  $\theta=0^\circ, \theta=180^\circ, \psi=0^\circ, \psi=180^\circ$ . If parameter  $D$  is equal to either  $A$  or  $C$ , three circles are enough.

#4: The radii of the major circles are defined by the  $A, C, D$  parameters.

Table 2 – The cyclide family, classified according to parameters  $A$ ,  $C$  and  $D$ .  
Black lines represent the principal circles of each cyclide surface.

Parameters	Cyclide type	
$0 < D \leq C < A$	Double-crescent cyclide	
$D = C$	Single-crescent cyclide	
$0 \leq C < D \leq A$	Ring cyclide (torus)	
$D = A$	Torus with a converging point or single singularity spindle-cyclide	
$0 \leq C \leq A < D$	Double-singularity spindle cyclide	



## 2. Mohr-Cyclides for Stress

### 2.1. Mohr-circles for stress

A stress tensor  $\mathbf{S}_{ij}$  can be represented in 2D as a Mohr diagram, defined by the three major circles, which represent planes of principal stress, and the area encompassed by them (Fig.3). The principal circles intersect the  $\sigma_n$  axis at three points, which correspond to the three principal axis of stress –  $\sigma_1$ ,  $\sigma_2$  and  $\sigma_3$  (maximum, intermediate and minimum stress). Since shear stress is zero at these orientations,  $\sigma_1$ ,  $\sigma_2$  and  $\sigma_3$  also represent the eigenvalues of  $\mathbf{S}_{ij}$ . Normal and shear stress ( $\sigma_n$  and  $\tau$ ) values can be read as Cartesian coordinates in the  $\sigma_n$ - and  $\tau$ -axis for any plane P, represented by its normal  $N_P$  within this area. The orientation of P with respect to the principal stresses is given by arcs of circles (dashed lines in Fig.3). Since stress is a symmetric tensor, principal circles are centred on the  $\sigma_n$ -axis and, for simplification, Mohr-diagrams usually display the top half-circles only. Alternatively, plane P can be plotted in the Mohr diagram with polar coordinates  $\sigma, \varphi$ , where  $\varphi$  is the angle between  $\sigma$  and  $\sigma_n$ , as:

$$\begin{aligned} M_x &= \tau = \sigma \cdot \sin \varphi \\ M_y &= \sigma_n = \sigma \cdot \cos \varphi \end{aligned} \quad (\text{Eq.3})$$

The three Mohr-circles  $\sigma_i \sigma_j$  can be analytically defined by the general circle equation:

$$\left(\sigma_n - \frac{\sigma_i + \sigma_j}{2}\right)^2 + \tau^2 = \left(\frac{\sigma_i - \sigma_j}{2}\right)^2 \quad i,j=(1,2,3) \text{ with } i < j \quad (\text{Eq.4})$$

Knowing either the values for the  $\sigma_1$ ,  $\sigma_2$  and  $\sigma_3$  principal stresses, or having a population of stress points, it is possible to define completely a 2D Mohr diagram for a particular stress tensor and to read  $\sigma_n$  and  $\tau$  as Cartesian coordinates.

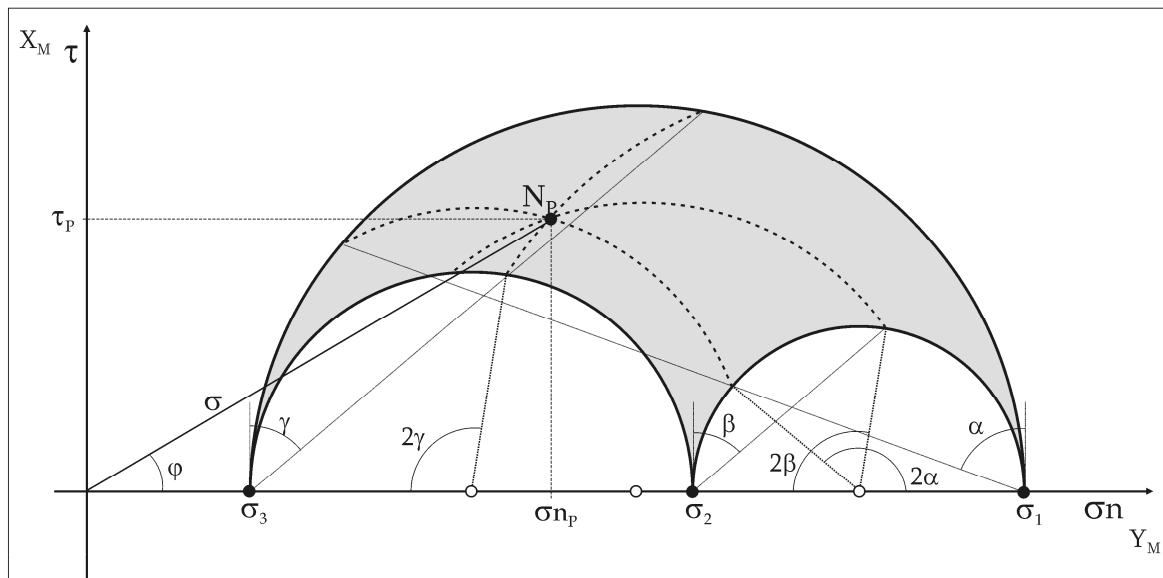


Fig. 3 - A Mohr-diagram for stress (lower half left out for simplicity). All possible orientations plot as poles to planes in the circle perimeter or in the shaded area. Stress components for a plane P can be read as Cartesian  $(\sigma_{n_p}, \tau_p)$  or polar  $(\sigma \cos\varphi, \sigma \sin\varphi)$  coordinates. Orientation of plane P is determined with angles  $\alpha, \beta, \gamma$ , measured to its pole with respect to the principal stresses  $\sigma_1, \sigma_2, \sigma_3$ .

## 2.2. Plotting procedure

The stress tensor operation assigns stress vectors  $\sigma$  to each plane P, via multiplication by its pole  $N_P$ . In traditional Mohr diagrams for stress, the angle between  $\sigma$  and  $N_P$  is used to find normal and shear stress for each plane, as discussed above. However, some information is omitted with this construction method, because angle  $\sigma \wedge N_P$  can be the same for planes with different orientations in space. This implies that two different planes are plotted in the same point in Mohr-space. 3D constructions in Mohr space address this problem.

Plotting  $S_{ij}$  in a three-dimensional space requires the extra step of defining a second angle. In order to do this, it is useful to choose an inherent property of the stress tensor itself, ie, something that does not involve external reference frames. I considered the relative orientation of the *stress plane* S, which contains all the stress vectors  $(\sigma, \sigma_n$  and  $\tau)$ , with respect to one of the eigenvectors of  $S_{ij}$ , in this

case,  $\sigma_1$ . This is the first significant difference between 2D and 3D representations of stress, since the geometrical properties of 2D Mohr-circles unavoidably lock S in its 2D ( $\sigma_n$ - $\tau$ ) reference frame. Angle  $\delta$  is thus defined as the angle between the *pole of stress plane* -  $N_s$  - and the maximum principal stress -  $\sigma_1$  (Fig.4).  $\delta$  values can be calculated using the dot-product expression:

$$N_s \cdot \sigma_1 = \bar{N}_s \cdot \bar{\sigma}_1 \cdot \cos \delta$$

$$\cos \delta = \frac{N_{sx}\sigma_{1x} + N_{sy}\sigma_{1y} + N_{sz}\sigma_{1z}}{\bar{N}_s \cdot \bar{\sigma}_1}$$

(Eq.5)

where  $N_{si}$ ,  $\sigma_{1i}$  are the vectorial components and the upper bar denotes magnitude. Since  $N_s$  is the pole of the stress plane, defined for instance by  $\sigma_n$  and  $\sigma$ , its components are obtained via the cross-product:

$$\sigma_n \times \sigma = \det \begin{vmatrix} N_{sx} & N_{sy} & N_{sz} \\ \sigma_{nx} & \sigma_{ny} & \sigma_{nz} \\ \sigma_x & \sigma_y & \sigma_z \end{vmatrix},$$

where

$$\begin{aligned} N_{sx} &= \sigma_{ny}\sigma_z - \sigma_{nz}\sigma_y \\ N_{sy} &= \sigma_{nz}\sigma_x - \sigma_{nx}\sigma_z \\ N_{sz} &= \sigma_{nx}\sigma_y - \sigma_{ny}\sigma_x \end{aligned} \quad (\text{Eq.6})$$

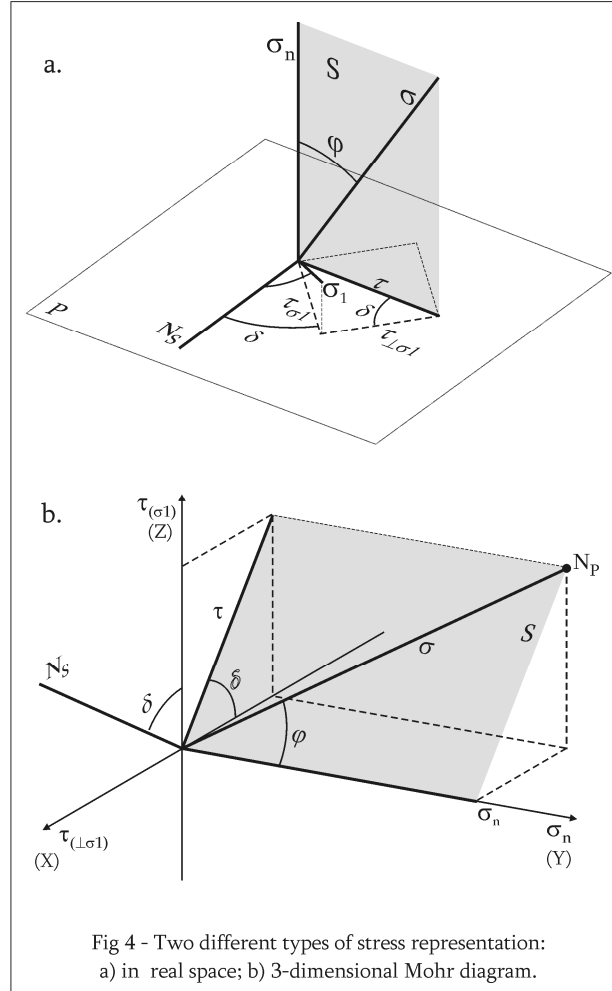


Fig 4 - Two different types of stress representation:  
a) in real space; b) 3-dimensional Mohr diagram.

Note that  $N_s$  is distinct from  $N_P$ , the pole to the plane P where stresses are operating, in fact,  $N_s$  is always a line in plane P (Fig.4a). Since  $N_s$  is normal to  $\tau$ , and following the Pythagoras theorem, shear stress in P can be partitioned in two components, one in the direction of  $\sigma_1$  -  $\tau_{\sigma_1}$ , and the other normal to the principal maximum stress -  $\tau_{\perp\sigma_1}$  (Fig.4).

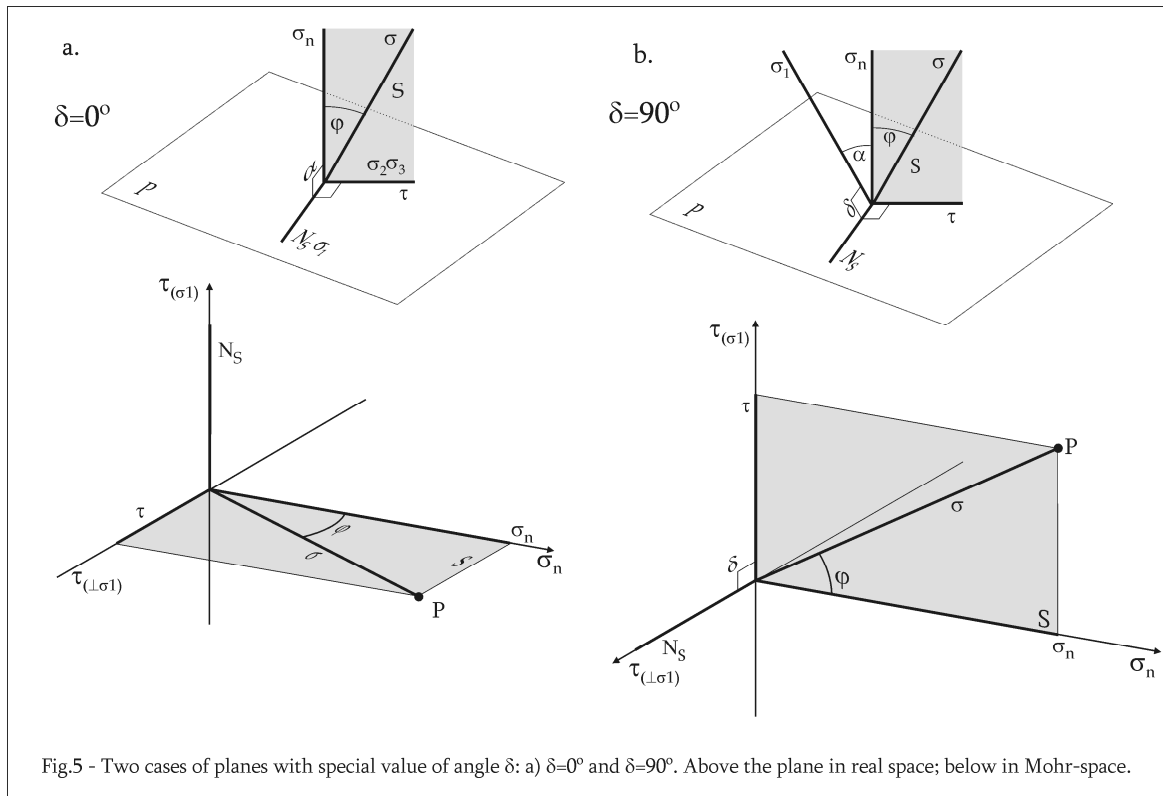
The value of  $\delta$  defines three cases of special significance to understand its geometrical effect:

1) Where  $\delta = 0^\circ$  (Fig.5a),  $\sigma_1$  lies in the P-plane and, therefore, is orthogonal to the S-plane and its components  $\sigma$ ,  $\sigma_n$  and  $\tau$ . It is clear that  $\sigma_2$  and  $\sigma_3$  will be on the S-plane and that  $\alpha (N \wedge \sigma_1) = 90^\circ$ , so  $\delta=0^\circ$  defines the  $\sigma_2\sigma_3$  principal stress plane, plotted in the XY-plane of the Mohr-cyclide. In this case, there is no shear stress in the  $\sigma_1$  direction ( $\tau_{\sigma_1} = 0$ ), which is in agreement with the condition  $\sigma_1 \perp \tau$ .

2) If  $\delta = 90^\circ$  (Fig.5b),  $\sigma_1$  is a line in the S-plane, normal to the P-plane. In this arrangement,  $\alpha$  is variable and one of the minor principal stresses (either  $\sigma_2$  or  $\sigma_3$ ) is parallel to  $N_s$ . Therefore,  $\delta=90^\circ$  is a

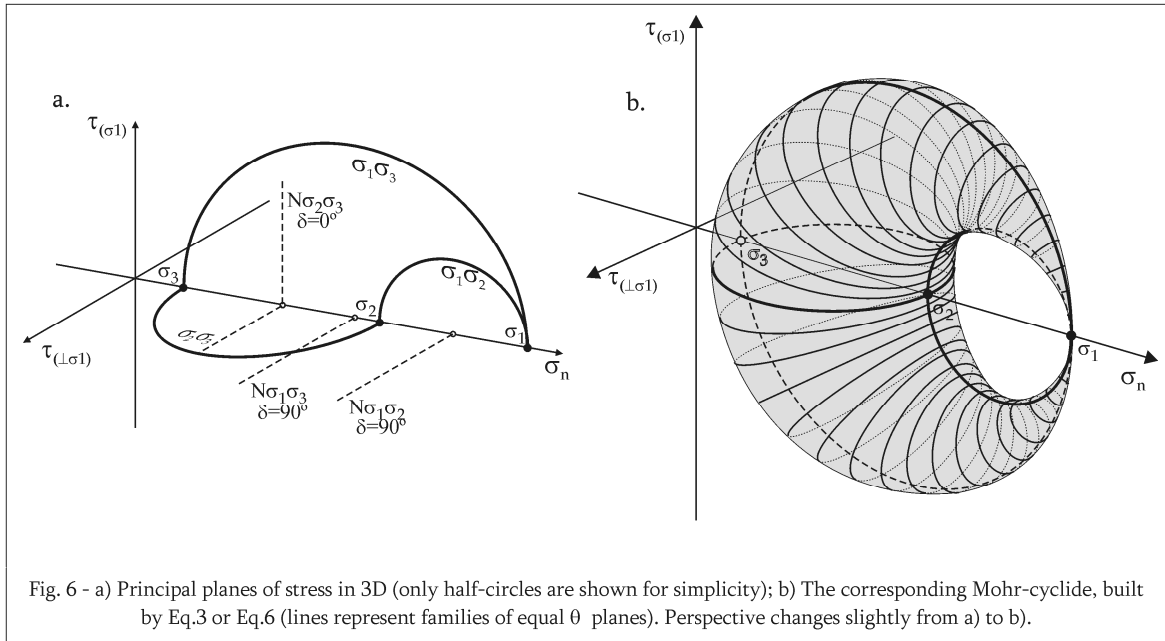
condition for the  $\sigma_1\sigma_2$  and  $\sigma_1\sigma_3$  principal planes of stress, which plot in the YZ-plane in Mohr space. In these planes, shear stress is null in orientations normal to  $\sigma_1$  ( $\tau_{\perp\sigma_1} = 0$ ), in good accord with the fact that  $\sigma_1$  and  $\tau$  are both in S.

3) All other scenarios, with  $\delta$  in the range  $]0^\circ, 90^\circ[$  or  $]90^\circ, 180^\circ[$  (Fig.4b) are intermediate between the two previous conditions and account for planes oblique to the principal stress planes.



In 2D representations of three-dimensional stress, all principal stress planes are coplanar circles in the Mohr-diagram. Adding angle  $\delta$  allows the stress planes to unfold from the fixed 2D plane (YZ) and materialise a three-dimensional surface with the same properties of a Mohr diagram (Fig.6). The resulting shape is a single-crescent cyclide, a *Mohr-cyclide for stress*, following the popular Mohr-circle denomination. They are spherical, three-dimensional surfaces that converge to a point representing the eigenvector chosen as reference, in this case,  $\sigma_1$ . The Mohr-cyclide can be defined in polar coordinates or analytically. Polar coordinates of P in a Mohr-cyclide are similar to coordinates in the 2D scenario, but with the extra degree of freedom added by angle  $\delta$  they become  $(\sigma, \varphi, \delta)$ , as shown in Fig.4b:

$$\begin{aligned}
 X_M &= \sigma \cdot \sin \varphi \cdot \cos \delta \\
 Y_M &= \sigma \cdot \cos \varphi \\
 Z_M &= \sigma \cdot \sin \varphi \cdot \sin \delta
 \end{aligned}
 \tag{Eq.7}$$



The analytical description of the Mohr-cyclide follows the equations of a general cyclide (Eq.1 and 2). However, Mohr-cyclides for stress represent a special case, where the simplification  $C = D$  applies (Table 2). The parameters can be further adapted, considering the radii of the principal circles of the cyclide which represent the principal planes of stress, as shown above (Fig.7):

$$A = \frac{2\sigma_1 - \sigma_2 - \sigma_3}{4} \quad (\text{Eq.8})$$

$$C = \frac{\sigma_2 - \sigma_3}{4}$$

There is, nevertheless, one important difference: cyclides in the canonical form are centred at the origin, while stress Mohr-cyclides may not. To address this problem, it is necessary to introduce an extra parameter, called  $E$ , that shifts the Mohr-cyclide in the Y-direction.  $E$  can be found by the expression:

$$E = \sigma_1 - A = \frac{2\sigma_1 + \sigma_2 + \sigma_3}{4} \quad (\text{Eq.9})$$

Note that  $E$  is not a translation in the physical sense, it merely allows the principal plane of the cyclide to be identical to the principal planes of stress. Substituting Eqs.8 and 9 into Eq.2, yields:

$$X_M = \frac{1/2\sqrt{\sigma_1^2 - \sigma_1\sigma_2 - \sigma_1\sigma_3 + \sigma_2\sigma_3} \cdot \sin\psi \cdot (\sigma_2 - \sigma_3) \cdot (\cos\theta - 1)}{2\sigma_1 - \sigma_2 - \sigma_3 - (\sigma_2 - \sigma_3) \cdot \cos\theta \cdot \cos\psi}$$

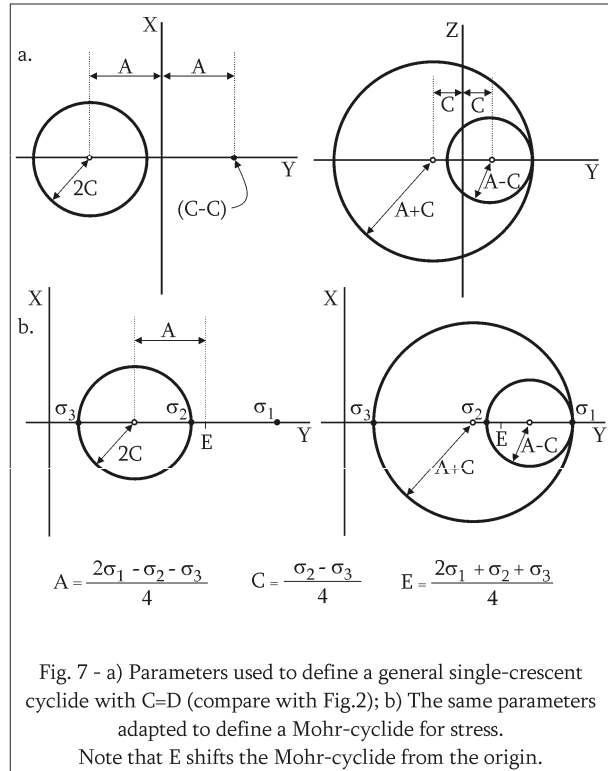
$$Y_M = \frac{(\sigma_2 - \sigma_3) \cdot [\sigma_2 - \sigma_3 - (2\sigma_1 - \sigma_2 - \sigma_3) \cdot \cos\theta \cdot \cos\psi] + (\sigma_1^2 - \sigma_1\sigma_2 - \sigma_1\sigma_3 + \sigma_2\sigma_3) \cdot \cos\theta}{2\sigma_1 - \sigma_2 - \sigma_3 - (\sigma_2 - \sigma_3) \cdot \cos\theta \cdot \cos\psi} +$$

$$Z_M = \frac{1/2\sqrt{\sigma_1^2 - \sigma_1\sigma_2 - \sigma_1\sigma_3 + \sigma_2\sigma_3} \cdot \sin\theta \cdot [2\sigma_1 - \sigma_2 - \sigma_3 - (\sigma_2 - \sigma_3) \cdot \cos\psi]}{2\sigma_1 - \sigma_2 - \sigma_3 - (\sigma_2 - \sigma_3) \cdot \cos\theta \cdot \cos\psi} + \frac{2\sigma_1 + \sigma_2 + \sigma_3}{4} \quad (\text{Eq.10})$$

A similar substitution can be done for Eq.1, but Eqs.10, although lengthy, are not complex and are definitely more practical to compute because they require only simple trigonometry, without involving 4<sup>th</sup>-degree polynomials.

A Mohr-cyclide for stress can, thus, be constructed using either:

- 1) The magnitudes of stress of a population of planes, with angles  $\varphi$  ( $\sigma \wedge \sigma_n$ ) and  $\delta$  ( $N_s \wedge \sigma_1$ ) and Eq.7 or;
- 2) The principal stresses values and Eqs.10.

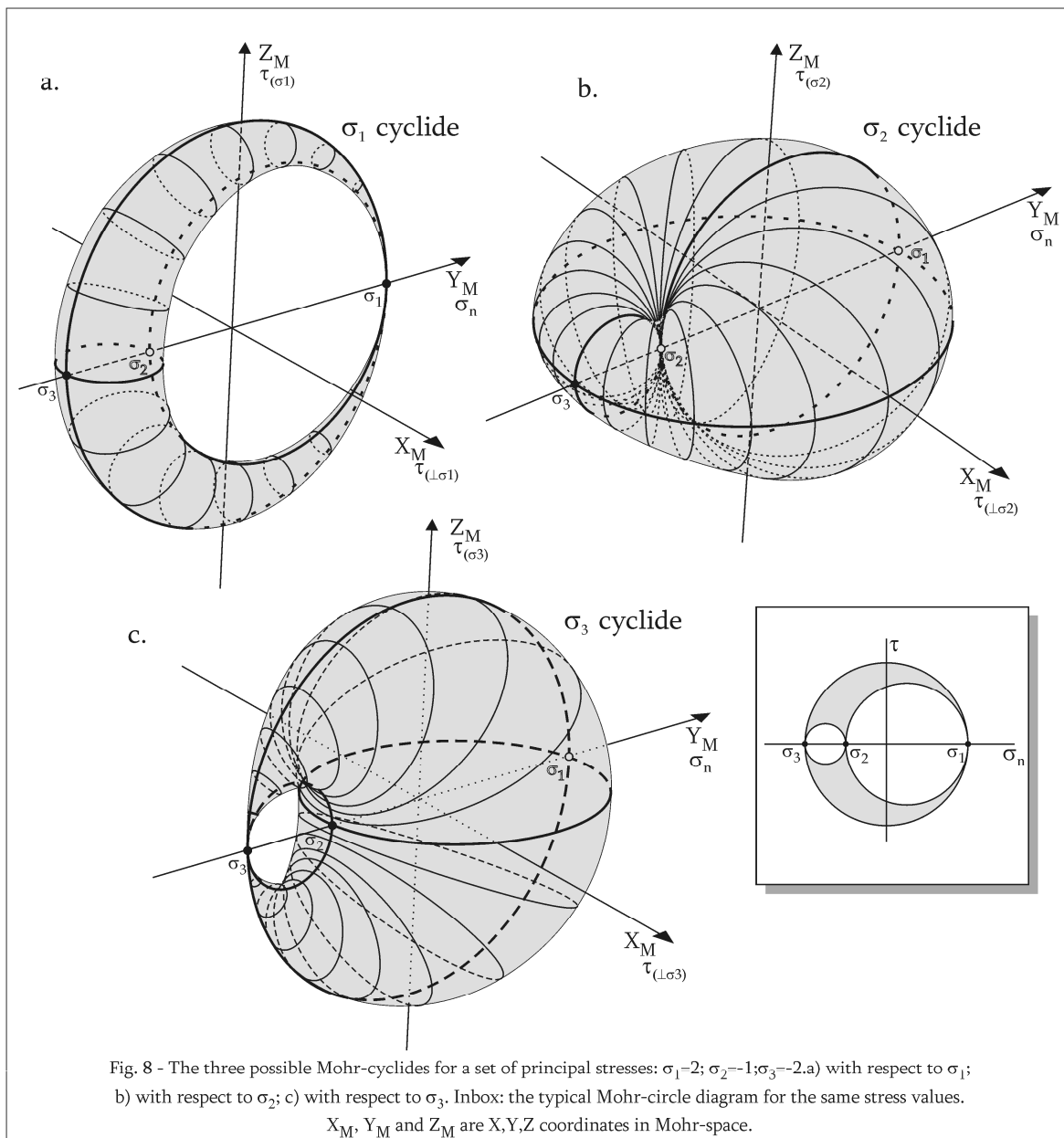


### 2.3. Alternative Mohr-cyclides for stress

Mohr-cyclides for stress are, as seen above, simple-crescent cyclides with a converging point at the principal maximum stress. Although  $\sigma_1$  was considered the most useful reference axis (Fig.6b, 8a), it is possible to define  $\delta$  with respect to any of the other principal stresses, which results in a change of the cyclide’s converging point. Doing this, even for the same relative magnitude of principal stresses, yields dramatic geometric differences.

Using  $\sigma_3$  as reference, the Mohr-cyclide keeps its simple-crescent shape, although reversed with respect to  $\sigma_1$ -cyclides (Fig.8c), because the convergence point is the minimum principal stress. Accordingly,  $\sigma_1\sigma_2$  is now horizontal, producing a “bulkier” shape, while  $\sigma_1\sigma_3$  and  $\sigma_2\sigma_3$  are vertical in Mohr-space. The most notorious geometrical variation appears when the intermediate  $\sigma_2$  is chosen as reference: the Mohr-cyclide loses the simple-crescent shape and becomes a torus with a converging point at  $\sigma_2$  (Fig.8b). The difference in surface shape may look remarkable but represents a continuum in the cyclide family, which results from “sliding” the converging point from the maximum principal stress

to the intermediate and minimum values. (If one would abandon the condition  $\sigma_1 > \sigma_2 > \sigma_3$ , and decrease  $\sigma_1$  gradually in Fig.8, the crescent would change to a sphere ( $\sigma_1 = \sigma_2$ ), then a torus ( $\sigma_2 > \sigma_1 > \sigma_3$ ), a second sphere ( $\sigma_1 = \sigma_3$ ) and finally a reversed crescent cyclide ( $\sigma_2 > \sigma_3 > \sigma_1$ ). The possible cyclides define the same stress tensor, each with respect to one of the three principal stresses, and can all be interpreted as Mohr-diagrams. However, the significance of the reference axes changes with the principal stress selected for each case.



It is possible to derive equations similar to Eq.7 and Eq.10 for the additional scenarios, considering the parameter changes noted in Table 3. Taking into account these geometrical differences,

the interpretation of these diagrams should be similar. It is interesting to note that, despite the fact that the differences are merely geometrical and a result of a different reference, all these three geometries are reduced to the same two-dimensional Mohr-circles diagram (inbox in Fig.8). This means that, if the Mohr-Coulomb failure envelope is ever adapted to Mohr-cyclides, its formulation must take into account the principal stress used to define the surface, since this choice has profound consequences in the cyclide geometry.

Table 3 – Parameters for a stress Mohr-cyclide

Reference axis	Cyclide shape	Cyclide parameters			
		<i>A</i>	<i>C</i>	<i>D</i>	<i>E</i>
$\sigma_1$	Single-crescent	$\frac{2\sigma_1 - \sigma_2 - \sigma_3}{4}$	$\frac{\sigma_2 - \sigma_3}{4}$	<i>C</i>	$\frac{2\sigma_1 + \sigma_2 + \sigma_3}{4}$
$\sigma_2$	Torus	$\frac{\sigma_1 - \sigma_3}{4}$	$\frac{-\sigma_1 + 2\sigma_2 - \sigma_3}{4}$	<i>A</i>	$\frac{\sigma_1 + 2\sigma_2 + \sigma_3}{4}$
$\sigma_3$	Single-crescent	$\frac{-\sigma_1 - \sigma_2 + 2\sigma_3}{4}$	$\frac{\sigma_1 - \sigma_2}{4}$	<i>C</i>	$\frac{\sigma_1 + \sigma_2 + 2\sigma_3}{4}$

## 2.4. Interpretation

Mohr diagrams are a popular tool in structural geology analysis, as well as in several engineering fields, because they provide a quick way of visualising and quantifying stress parameters. The known Mohr-circles can provide, for any plane P, information about shear and normal stress ( $\tau_P$ ,  $\sigma_n$ ) and angles of P with the three principal stresses ( $\alpha$ ,  $\beta$  and  $\gamma$ ). Mohr-diagrams have a great advantage over stress ellipsoid as a visualisation tool, because ellipsoids can only be constructed if  $\sigma_1, \sigma_2, \sigma_3$  are all positive or all negative. In this section, I will show how Mohr-cyclides are useful for these estimations.

### 2.4.1. Normal and shear stress

The departure from 2D representations, where the XY Cartesian axis are labelled  $\sigma_n$  and  $\tau$  implies that coordinates in Mohr-cyclides must be interpreted differently. While  $\sigma_n$  can still be read directly as the Y-Mohr coordinate ( $Y_M$ ), there is no similar parallel for the value of  $\tau$ , which is now a vector in the  $X_M Y_M$  plane. The Cartesian coordinates of this 3D representation should be read as follows (Fig.4b):

- 1)  $X_M$  :  $\tau_{(\sigma^1)}$ , component of  $\tau$  in the  $\sigma_1$  direction
- 2)  $Y_M$  :  $\sigma_n$ , normal stress (as in 2D)
- 3)  $Z_M$  :  $\tau_{(\perp\sigma^1)}$ , component of  $\tau$  in the direction orthogonal to  $\sigma_1$

If the cyclide is defined with respect to a principal stresses other than  $\sigma_1$ , then this interpretation must be changed accordingly as illustrated in Figure 8.

2D Mohr-circles allow the reader to infer  $\sigma_n$  and  $\tau$  values for each plane from Cartesian coordinates in Mohr-space and this is also possible in Mohr-cyclides. However, since  $\tau$  is partitioned into two components,  $\tau$ -values are read indirectly according to  $\tau^2 = \tau_{(\sigma_1)}^2 + \tau_{(\perp\sigma_1)}^2$ . A second method to determine  $\sigma_n$  and  $\tau$  values relies on the fact that Mohr-cyclides always give the values of principal stresses, the only three intersections of the cyclide surface with the  $Y_M$  coordinate axis. Knowing this, the precise magnitudes of  $\sigma_n$  and  $\tau$  can be determined with analytical equations including  $\sigma_1$ ,  $\sigma_2$  and  $\sigma_3$ . These are:

$$\begin{aligned} \sigma_n &= (\sigma_1 - \sigma_3) \cos^2 \alpha + (\sigma_2 - \sigma_3) \cos^2 \beta \\ \tau^2 &= (\sigma_1 - \sigma_3)^2 \cos^2 \alpha \cos^2 \beta + (\sigma_2 - \sigma_3)^2 \cos^2 \beta \cos^2 \gamma + (\sigma_1 - \sigma_3)^2 \cos^2 \alpha \cos^2 \gamma \end{aligned} \quad (\text{Eq.11})$$

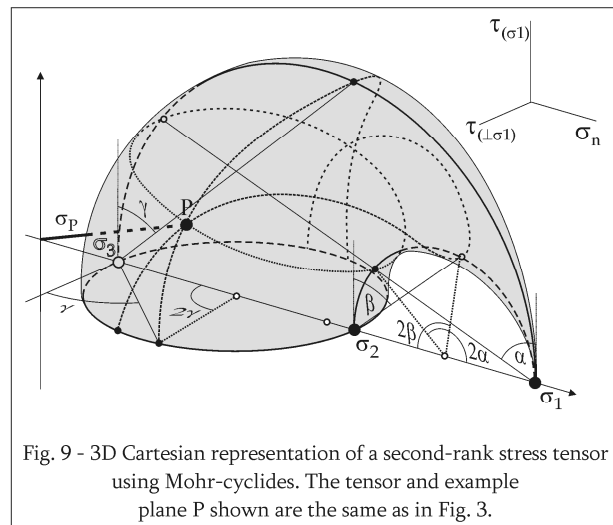
and their derivation can be found in general structural geology text books such as, for instance, Ramsay and Lisle (2000, page 786-787).

#### 2.4.2. Angles with principal stresses

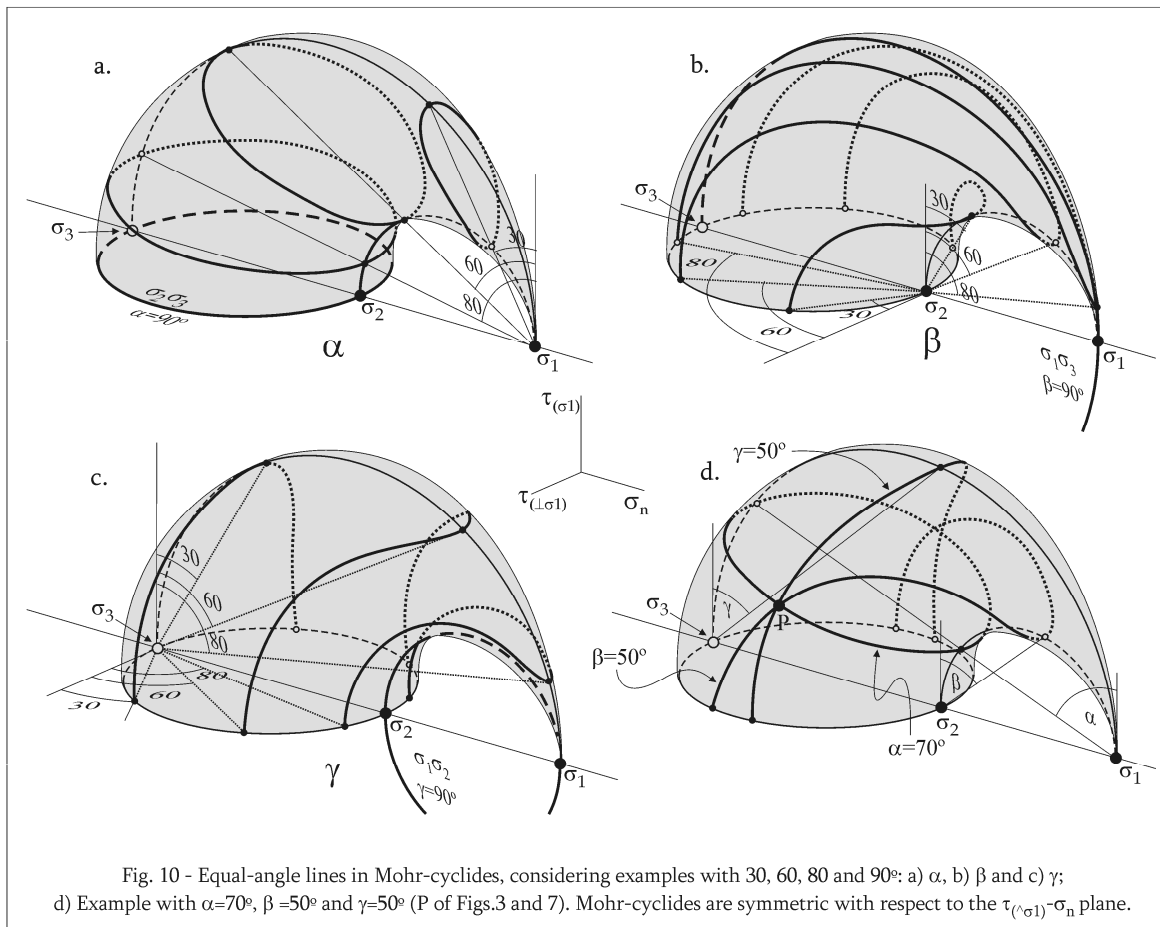
Mohr diagrams are especially useful because they allow quantification of the angles between the pole to a plane,  $N_P$ , and the principal stresses,  $\sigma_1$ ,  $\sigma_2$  and  $\sigma_3$ . In Mohr-circles, angles  $\alpha$ ,  $\beta$  and  $\gamma$ , can be read in two ways (Fig.3):

- 1) directly, considering lines parallel to  $\tau$  at  $\sigma_1$ ,  $\sigma_2$  and  $\sigma_3$ , or
- 2) as double angles in the principal planes of stress,  $\sigma_1\sigma_2$ ,  $\sigma_1\sigma_3$  and  $\sigma_2\sigma_3$ .

Since Mohr-circles are a 2D representation, the angles are all contained in the  $XY$ -plane ( $\sigma_n\tau$ ). Equal-angle lines will be represented as arcs in the Mohr-circle plane, in the space limited by the three principal circles (grey in Fig.3). These arcs are concentric with respect to the centres of principal circles (dashed lines in Fig.3). Each angle measures  $90^\circ$  in the plane that does not contain its reference principal stress:  $\alpha$  ( $P \wedge \sigma_1$ ) is  $90^\circ$  in  $\sigma_2\sigma_3$ ,  $\beta$  ( $P \wedge \sigma_2$ ) in  $\sigma_1\sigma_3$  and  $\gamma$  ( $P \wedge \sigma_3$ ) in  $\sigma_1\sigma_2$ .



The same principles apply to 3D Mohr-cyclides, though the extra dimension adds insight on how these angles are distributed in space. As before,  $\alpha$ ,  $\beta$  and  $\gamma$  can be read as single or double angles (Fig.9), but in Mohr-cyclides equal-angle lines are not confined to a plane and have more complex geometries than concentric arcs, illustrated on Fig. 10. An interesting point to note is that only equal  $\alpha$  lines, although not arcs of circles, keep a relatively simple geometry. This is because the Mohr-cyclide in Fig. 10 is defined with respect to  $\sigma_1$ .



### 2.4.3. Geometrical variation

Mohr-cyclides for stress are defined by the values of the eigenvectors of  $\mathbf{S}_{ij}$ , which translate into the physical world as the principal stresses in a particular stress field. Because principal stresses define the stress ellipsoid, Mohr-cyclides are powerful tools to represent graphically its shape variations and the stress state they represent. A compact way to illustrate the relationship between stress ellipsoid and Mohr-cyclide is by means of the stress diagram suggested by Lisle (1979). The graph makes use of the stress ratio,

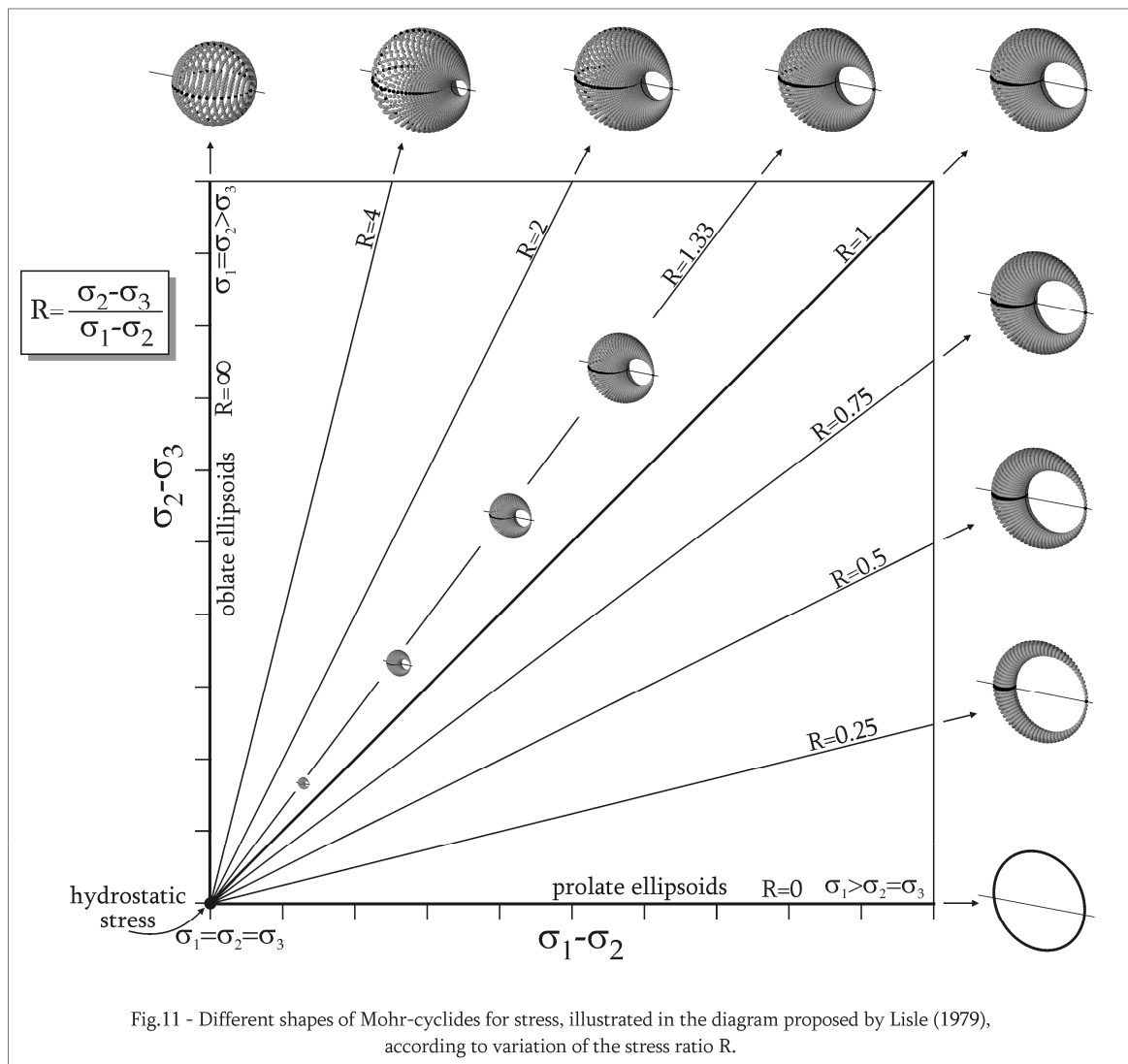
$$R = \frac{d_1}{d_2} = \frac{\sigma_2 - \sigma_3}{\sigma_1 - \sigma_2}$$

by plotting  $d_1$  values as ordinates and  $d_2$  as abscissas. I could have used other stress ratios, such as the  $\varphi$  proposed by Angelier (1979) and Etchecopar et al. (1981), or the Lode parameter, to build alternative graphs, but  $R$  proved to be the most useful for the present purpose. Figure 11 illustrates all possible shapes of Mohr-cyclides, defined with respect to  $\sigma_1$ , and allows the following observations:

a) *Oblate stress ellipsoids*, characterised by  $\sigma_1 = \sigma_2 > \sigma_3$ ,  $R = \infty$  and typical of axial extension stress states, plot in the  $d_1$ -axis and are represented by *spheres*. This applies to both uni- and biaxial extensions.

b) On the other hand, the (uni- or bi-) axial compression represented by *prolate stress ellipsoids*, with  $\sigma_1 > \sigma_2 = \sigma_3$  and  $R = 0$ , plots in the  $d_2$ -axis. The Mohr-cyclide for this state is a *circle*.

c) Hydrostatic stress, where  $\sigma_1 = \sigma_2 = \sigma_3$ , is given by a point at the origin of the diagram. In Mohr-space, hydrostatic stress is also represented by a point.



d) Intermediate situations, with  $\sigma_1 \neq \sigma_2 \neq \sigma_3$ , are given by *single-crescent cyclides* with different proportions, according to their R-value.

The fact that some stress ellipsoids can be represented in Mohr-space by spheres and circles is in no contradiction with the statement that three-dimensional Mohr-diagrams are surfaces of the cyclide family. Spheres can be interpreted as a special type of cyclide, the surface that materialises the transition between single crescent cyclides and torii. Although simpler analytical solutions are the norm in common use, spheres can also be described with the implicit or parametric equations of the cyclide family (Eq.1-2). The same reasoning applies to circles.

### 3. Mohr-Cyclides for Flow

#### 3.1. The flow tensor

The flow tensor, known also as velocity gradient tensor ( $\mathbf{L}_{ij}$ ), describes the velocity field of any point in a homogeneously deforming body (eg. Spencer 1980):

$$L_{ij} = \frac{\partial v_i}{\partial x_j} \quad v_i = L_{ij}x_j \quad (\text{Eq.12})$$

Since it is fixed in a set coordinate reference frame,  $\mathbf{L}_{ij}$  does not account for translation.  $\mathbf{L}_{ij}$  describes an instantaneous velocity field and does not include information about deformation paths or finite strain. The flow tensor can be linked with incremental deformation when integrated in order to time (Ramberg 1975). The flow tensor can be decomposed in its symmetric ( $\mathbf{D}_{ij}$ ) and antisymmetric ( $\mathbf{W}_{ij}$ ) components (eg Spencer 1980, Lister and Williams 1983, Means 1983). The partitioning of  $\mathbf{L}_{ij}$  is additive:

$$\begin{aligned} L_{ij} &= D_{ij} + W_{ij} \\ D_{ij} &= \frac{1}{2}(L_{ij} + L_{ij}^T) \\ W_{ij} &= \frac{1}{2}(L_{ij} - L_{ij}^T) \end{aligned} \quad (\text{Eq.13})$$

$\mathbf{D}_{ij}$ , the strain rate, stretching rate or rate of deformation tensor, can be interpreted as the stretching component of flow. It is a symmetric quantity and its eigenvectors are known as the *instantaneous stretching axes* of flow (ISA<sub>i</sub>). The eigenvalues associated with these directions are the *instantaneous stretching rates*,  $\dot{s}_i$  (eg Lister and Williams 1983, Means 1983).  $\dot{s}$

$\mathbf{W}_{ij}$ , the antisymmetric or skewed part, is the vorticity tensor and represents the rotational component of flow and the angular velocities ( $\omega$ ) of lines. The rotational features of the velocity field can

be described in terms of angular velocities with respect to the external reference frame and the ISA (Means et al. 1980):

$$\boldsymbol{\omega}_{em} = \boldsymbol{\omega}_{eISA} + \boldsymbol{\omega}_{ISAm} \quad (\text{Eq.14})$$

where  $\boldsymbol{\omega}_{em}$ , the angular velocity of line  $m$  with respect to the external reference frame ( $e$ ) is the sum of the angular velocity of the ISA with respect to  $e$  ( $\boldsymbol{\omega}_{ISAE}$ ) and the angular velocity of  $m$  with respect to the ISA ( $\boldsymbol{\omega}_{ISAm}$ ). It is possible now to define two vorticity vectors, “the peculiar and characteristic glory of three-dimensional kinematics” (Truesdell 1954, pg 59):

$$\begin{aligned} \vec{W} &= 2\boldsymbol{\omega}_{em} \\ \vec{w} &= 2\boldsymbol{\omega}_{sm} \end{aligned} \quad (\text{Eq.15})$$

$\vec{W}$  is the vorticity of material lines with respect to the reference frame and  $\vec{w}$  is the vorticity with respect to the ISA. Doubling Eq.14 and substituting the terms as in Eq.15, we obtain (Means et al., 1980):

$$\vec{W} = \vec{W}' + \vec{w} \quad \text{with} \quad \vec{W}' = 2\boldsymbol{\omega}_{es} \quad (\text{Eq.16})$$

where  $\vec{W}'$ , the spin component, describes the angular velocity of the ISA with respect to the external reference frame; in steady-state flow,  $\vec{W}'$  is considered zero (Means et al. 1980, Lister and Williams 1983). The  $w_i$  components of the vorticity vectors, either  $\vec{W}$  or  $\vec{w}$  ( $w_x, w_y, w_z$ ), can be read directly from the vorticity tensor  $\mathbf{W}_{ij}$  (Means et al., 1980):

$$W_{ij} = \begin{vmatrix} 0 & -\frac{1}{2}w_z & \frac{1}{2}w_y \\ \frac{1}{2}w_z & 0 & -\frac{1}{2}w_x \\ -\frac{1}{2}w_y & \frac{1}{2}w_x & 0 \end{vmatrix} \quad (\text{Eq.17})$$

The relative importance of stretching and rotational components of flow is often described by  $W_T$ , the kinematic vorticity number defined by Truesdell (1954), which combines the magnitude of  $\vec{w}$  and the stretching rates associated with the ISA:

$$W_T = \frac{\vec{w}}{\sqrt{2(\dot{s}_1^2 + \dot{s}_2^2 + \dot{s}_3^2)}} \quad (\text{Eq.18})$$

This is a very useful relationship which allows two extremes:

- 1) For  $\mathbf{W}_T = \mathbf{0}$ , material lines do not rotate with respect to the ISA, or, in other words, the flow is coaxial.
- 2) For  $\mathbf{W}_T = \infty$ , the instantaneous stretching rate is zero, which means that the flow is a rigid rotation.

Everything else in the middle reflects non-coaxial flows, with simple shear assuming the value  $W_T = 1$ .

Truesdell's vorticity number describes general flow in three-dimensions. However, most of the published literature on the subject considers only monoclinic flows, where vorticity is parallel to one of the ISA and to one of the flow apophyses (eigenvectors) of  $\mathbf{L}_{ij}$ . In this instance, it is possible to simplify  $W_T$  into:

$$W_{T_i} = \frac{w_i}{\sqrt{2(\dot{s}_j^2 + \dot{s}_k^2)}}, \quad (\text{Eq.19})$$

a sectional Truesdell vorticity number, defined in section  $jk$ , normal to  $ISA_i$  and flow apophysis  $\mathbf{e}_i$ . However, as noted by Passchier (1997),  $w$  and the stretching rates along the ISA may vary by some orders of magnitude. The problem is solved by defining a normalising parameter  $\bar{s}$ , the mean stretching rate in the section normal to vorticity in monoclinic flows (Passchier 1997):

$$\bar{s} = \frac{|\dot{s}_j - \dot{s}_k|}{2} \quad (\text{Eq.20})$$

Dividing  $w/2$  (see Eq.17) by  $\bar{s}$  we obtain the *sectional kinematic vorticity number*.

$$W_{K_i} = \frac{w_i}{|\dot{s}_j - \dot{s}_k|} \quad (\text{Eq.21})$$

$W_K$  is intimately connected with the nature of  $\mathbf{L}_{ij}$  and can also be defined with the angle between the flow apophyses at  $jk$  (eg Passchier 1987, Bobyarchick 1987):

$$W_{K_i} = \cos(e_j \wedge e_k) = \cos \nu \quad (\text{Eq.22})$$

Passchier (1997, 1998) derived other kinematic numbers that can be used to further describe monoclinic flows, namely the *sectional kinematic dilatancy number*,  $A_K$ ,

$$A_{K_i} = \frac{\dot{s}_j + \dot{s}_k}{\dot{s}_j - \dot{s}_k}, \quad (\text{Eq.23})$$

the *sectional kinematic extrusion number*,  $T_K$ ,

$$T_K = \frac{\dot{s}_i}{\dot{s}_j - \dot{s}_k} \quad (\text{Eq.24})$$

and the *kinematic volume change number*,  $V_K$

$$V_K = A_K + T_K = \frac{\dot{s}_i + \dot{s}_j + \dot{s}_k}{\dot{s}_j - \dot{s}_k} \quad (\text{Eq.25})$$

$A_K$  defines the rate of area change in the  $jk$ -plane, while  $T_K$  is a measure of the stretching rate along the vorticity direction and  $V_K$  quantifies rate of volume change. The effects of these parameters in the flow geometry are summarised in Table 4. According to Passchier (1997),  $W_K$ ,  $A_K$ ,  $T_K$  and  $V_K$  are

dimensionless numbers that fully describe the geometry of a flow with vorticity parallel to  $ISA_i$  ( $e_i$ ) and normal to the plane  $ISA_jISA_k$  ( $e_j e_k$ ).

Table 4 – Effect of kinematic parameters in monoclinic flows with vorticity parallel to  $ISA_i$ , following Passchier (1997).

Parameter	Formula	< 0	0	> 0
$W_k$	$\frac{w}{ s_j - s_k } = \cos \nu$	Clockwise non-coaxial	Coaxial flow	Counter-clockwise non-coaxial
$A_k$	$\frac{s_j + s_k}{s_j - s_k}$	Area decrease	Equal area	Area increase
$T_k$	$\frac{s_i}{s_j - s_k}$	Shortening in $i$	Plane strain	Stretching in $i$
$V_k$	$\frac{s_i + s_j + s_k}{s_j - s_k}$	Volume decrease	Isochoric flow	Volume increase

### 3.2. Mohr-circles for monoclinic flow

Mohr-circles for the flow tensor, first introduced by Lister and Williams (1983, following Platt), have the following properties (Fig.12):

1) The coordinate axes  $X_M, Y_M$  represent, respectively,  $\dot{s}$  - stretching rate and  $\dot{\omega}$  - rate of angular velocity.

2) As for stress, the Mohr-circle is defined by the diameter  $L_{11}; -L_{21}, L_{22}; L_{12}$  (cf. Means 1982).

3) The maximum and minimum stretching rates plot in the diameter parallel to the  $\dot{s}$ -axis; they represent the maximum and minimum instantaneous stretching axes:  $ISA_1$  and  $ISA_2$ .

4) Any point  $m$ , with  $\eta = m \wedge ISA_1$  measured counter clockwise in real and Mohr space, has  $\dot{\omega}_m$  angular velocity and  $\dot{s}_m$  stretching rate.

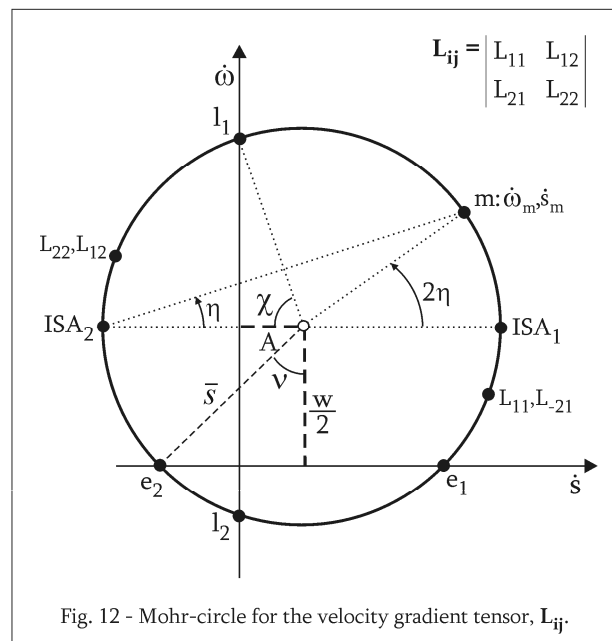


Fig. 12 - Mohr-circle for the velocity gradient tensor,  $L_{ij}$ .

5) The Mohr-circle intersects the abscissa at  $e_1$  and  $e_2$ , the two single directions of no angular velocity - the eigenvectors of  $\mathbf{L}_{ij}$ ;  $v = e_1 \wedge e_2$ . Some flows have only one eigenvector and others none; in these cases, the Mohr-circle has one or zero intersections with the abscissa.

6) The Mohr-circle intersects the ordinate at  $\mathbf{l}_1$  and  $\mathbf{l}_2$ , the two single directions of no instantaneous stretch;  $\chi = \mathbf{l}_1 \wedge \mathbf{l}_2$ . As in 5), it is possible to have only one or zero intersections with the ordinate.

7) From 3) it is clear that the radius of the Mohr-circle corresponds to the mean stretching rate  $\bar{s} : (ISA_1 - ISA_2)/2$ .

8) Coordinates of the Mohr-circle centre are of special significance: the ordinate of the centre is half the magnitude of the vorticity vector -  $w/2$  (cf. 5) and Eq.21); the abscissa  $A$  is a measure of area change, closely related to  $A_K$ :

$$A_K = \cos \chi$$

$$A = A_K \cdot \bar{s} \tag{Eq.26}$$

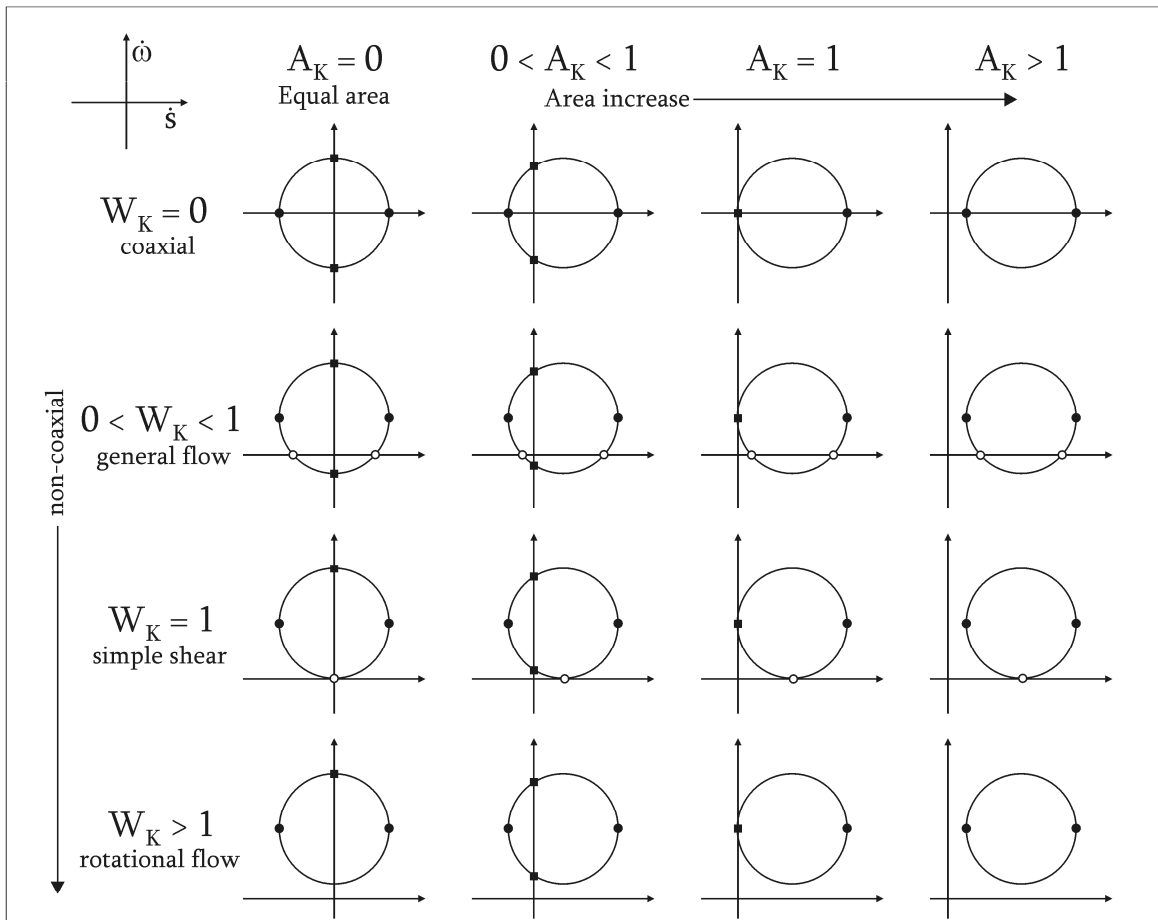


Fig. 13 - Basic two-dimensional flow geometries represented by Mohr-circles. Closed circles: ISA; open circles: eigenvectors of  $L_{ij}$ ; squares: lines of no instantaneous stretch. Flow names as in Passchier (1997), Simpson and DePaor (1993). Area decrease ( $A_K < 0$ ) and clockwise shear senses ( $W_K < 0$ ) are not represented for simplicity because they are symmetric to the positive counterparts..

Mohr-circles are, thus, able to represent different types of two-dimensional flow, such as pure shear, general non-coaxial or special types of pulsating flows (Fig.13). The relationship between Mohr-circle geometry and the characteristics of  $\mathbf{L}_{ij}$ , allows the diagrams to be useful as a gauge of flow parameters (Passchier and Urai 1988, Passchier 1990b, 1991) or as elements to study inhomogeneous progressive deformation (Means 1983).

### 3.3. Plotting procedure

The procedure followed in this section is in some ways analogous to the description of stress-cyclides (section 4.2), although adapted to the characteristics of a flow tensor. The most important divergence is that, unlike  $\mathbf{S}_{ij}$ , the flow tensor does not have to be symmetric, ie, allows lower symmetries. The degree of symmetry of flow depends on the relationship between the vorticity vector and the ISA: if  $\vec{w}$  is parallel to one of the ISA, flow is considered monoclinic; if not, the flow has triclinic geometry (eg Robin and Cruden, 1994; Jiang and Williams, 1998; Iacopini et al., 2006).

The canonical form of a monoclinic flow tensor with  $\text{ISA}_k$  parallel to vorticity in the  $zz$ -direction is:

$$L_{ij} = \begin{vmatrix} L_{11} & L_{12} & 0 \\ L_{21} & L_{22} & 0 \\ 0 & 0 & L_{33} \end{vmatrix} \quad (\text{Eq.27})$$

where  $\text{ISA}_i$  and  $\text{ISA}_j$  lie in the  $xy$ -plane at an angle with the reference frame. Before proceeding, it is useful to write  $\mathbf{L}_{ij}$  in such a way that all the ISA are parallel to the reference frame. (This step is not strictly necessary, but produces user friendly algebra below.) This can be accomplished with the general tensor transformation rule (De Paor and Means, 1984):

$$L'_{ij} = R_{ij} \cdot L_{ij} \cdot R_{ij}^T \quad (\text{Eq.28})$$

$\mathbf{R}_{ij}$  is an orthogonal rotation tensor and  $\mathbf{R}_{ij}^T$  its transpose. The result follows the additive properties of  $\mathbf{L}_{ij}$  (Eq.13):

$$L'_{ij} = \begin{vmatrix} \dot{s}_x & -w_z/2 & 0 \\ w_z/2 & \dot{s}_y & 0 \\ 0 & 0 & \dot{s}_z \end{vmatrix} \quad (\text{Eq.29})$$

$\mathbf{L}'_{ij}$  is the equivalent of  $\mathbf{L}_{ij}$  in a reference frame where  $\text{ISA}_x$  is parallel to  $xx$ ,  $\text{ISA}_y$  to  $yy$  and  $\text{ISA}_z$  to  $zz$ , identical to its parent in eigenvalues, principal stretching rates, vorticity magnitude, relative orientation of  $\vec{w}$  with respect to the ISA and, it follows, in all kinematic numbers (Eqs.20-25) and Truesdell's vorticity number (Eq.18). The main advantage of preferring  $\mathbf{L}'_{ij}$  to  $\mathbf{L}_{ij}$  is that principal stretches and components of  $\vec{w}$  are given directly from tensor components and, as such, tedious

calculations of  $D_{ij}$  eigenvalues can be bypassed. Other monoclinic flows can also be described with this notation (cf. Eq.17):

$$L'_{ij} = \begin{vmatrix} \dot{s}_x & 0 & w_y/2 \\ 0 & \dot{s}_y & 0 \\ -w_y/2 & 0 & \dot{s}_z \end{vmatrix}, \quad \mathbf{w} \text{ parallel to ISA}_y \text{ and } yy \quad (\text{Eq.30})$$

$$L'_{ij} = \begin{vmatrix} \dot{s}_x & 0 & 0 \\ 0 & \dot{s}_y & -w_x/2 \\ 0 & w_x/2 & \dot{s}_z \end{vmatrix}, \quad \mathbf{w} \text{ parallel to ISA}_x \text{ and } xx \quad (\text{Eq.31})$$

Henceforth,  $L'_{ij}$  will be written simply  $L_{ij}$ .

$L_{ij}$  describes the velocity field of an imaginary particle at a point  $m$  in space, defined by the position vector  $\vec{m}$  (Fig.14a):

$$v_i = L_{ij} m_j \quad (\text{Eq.12})$$

This operation results in three velocity vectors, oriented with respect to the reference axis; using tensor notation of Eqs. 29-31, these are coincident with the ISA and  $\vec{w}$  will be parallel to one of them. These velocity vectors define  $\dot{d}$ , the rate of displacement vector, also a velocity; its magnitude,  $\bar{d}$ , is given by the Pythagoras theorem:

$$\bar{d} = \sqrt{v_x^2 + v_y^2 + v_z^2} \quad (\text{Eq.32})$$

$\dot{d}$  describes the velocity of a particle that happens to be at point  $m$  in a given moment of deformation, or, in other words, describes velocity vectors from an Eulerian perspective. The orientation of  $\dot{d}$  in space is crucial to build Mohr-cyclides for flow and is given by two angles,  $\phi$  and  $\delta$  (Fig.14a).  $\phi$  is the angle between  $\dot{d}$  and  $\vec{m}$  the position vector of  $m$ , given by the dot-product:

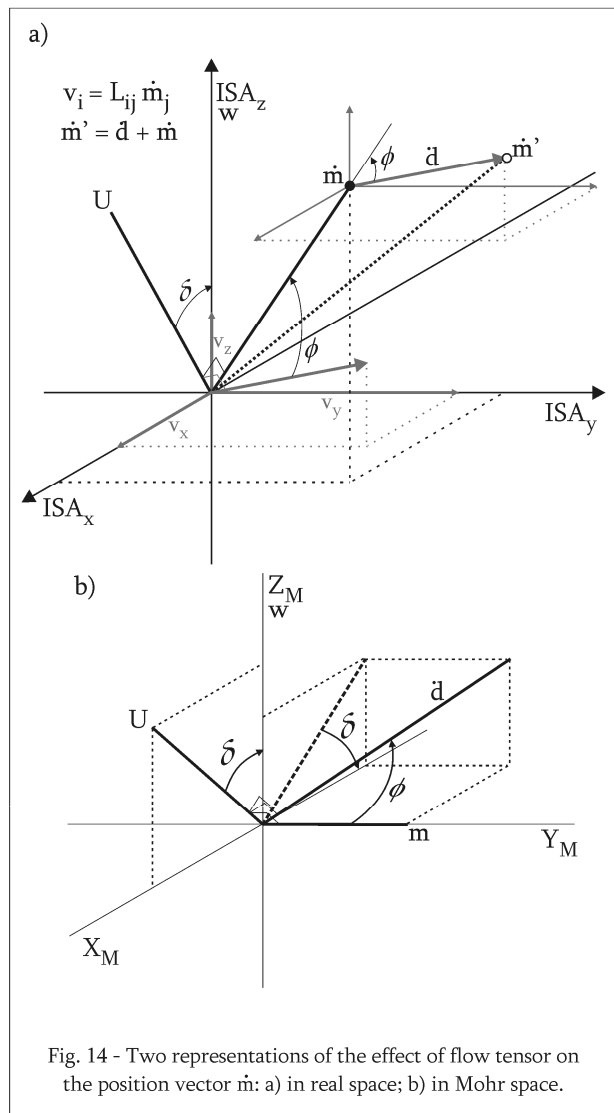


Fig. 14 - Two representations of the effect of flow tensor on the position vector  $\vec{m}$ : a) in real space; b) in Mohr space.

$$\cos \varphi = \frac{m_x v_x + m_y v_y + m_z v_z}{d} \quad (\text{Eq.33})$$

$\delta$  is the angle between  $\mathbf{U}$ , the pole of the plane defined by  $\dot{\mathbf{d}}$  and  $\vec{m}$ , and one of the eigenvectors of  $\mathbf{L}_{ij}$ . Since the Mohr-cyclide is being constructed for monoclinic flow, it is interesting to choose the eigenvector that lies parallel to the vorticity vector  $\vec{w}$ , and thus,  $\delta$  can be defined simply as  $\mathbf{U} \wedge \vec{w}$ :

$$\cos \delta = \frac{U_x w_x + U_y w_y + U_z w_z}{\mathbf{U} \cdot \mathbf{w}} \quad (\text{Eq.34})$$

$U_i$  components are obtained with the cross-product of  $\vec{m}$  and  $\dot{\mathbf{d}}$ :

$$\vec{m} \times \dot{\mathbf{d}} = \det \begin{vmatrix} U_x & U_y & U_z \\ m_x & m_y & m_z \\ v_x & v_y & v_z \end{vmatrix}, \text{ where}$$

$$\begin{aligned} U_x &= m_y v_z - v_y m_z \\ U_y &= m_z v_x - v_z m_x \\ U_z &= m_x v_y - v_x m_y \end{aligned} \quad (\text{Eq.35})$$

With vorticity fixed in the  $zz$ -axis in Mohr-space, irrespective of its real orientation in real space, the Mohr-cyclide can now be plotted with the following polar coordinates (Fig.14b):

$$\begin{aligned} X_M &= \bar{d} \cdot \sin \varphi \cdot \cos \delta \\ Y_M &= \bar{d} \cdot \cos \varphi \\ Z_M &= \bar{d} \cdot \sin \varphi \cdot \sin \delta \end{aligned} \quad (\text{Eq.36})$$

$\vec{w}$  can be considered in any of the reference axes;  $zz$  was chosen here for graphical convenience.

Alternatively, Mohr-cyclides for monoclinic flows can be described by the general cyclide equations (Eq.1 and 2), adapted to reflect the geometry of a flow tensor as done above for stress. There are, however, two major differences. First,  $\mathbf{L}_{ij}$  does not have to be symmetric, in fact it is not for all non-coaxial flows. Second, angle  $\delta$  in flow-cyclides is measured with respect to  $\vec{w}$  (which can be parallel to any of the ISA), whereas in stress,  $\delta$  is tagged to  $\sigma_1$ . Considering the general case where the vorticity vector  $\vec{w}$  is parallel to the  $i$ -axis and  $\text{ISA}_i$ , parameters  $A$ ,  $C$  and  $E$  can be redefined with the formulas (Fig.15):

$$A = \sqrt{(E_y - \dot{s}_i)^2 + E_x^2}$$

$$C = \frac{|\dot{s}_j - \dot{s}_k|}{4} \quad (\text{Eq.37})$$

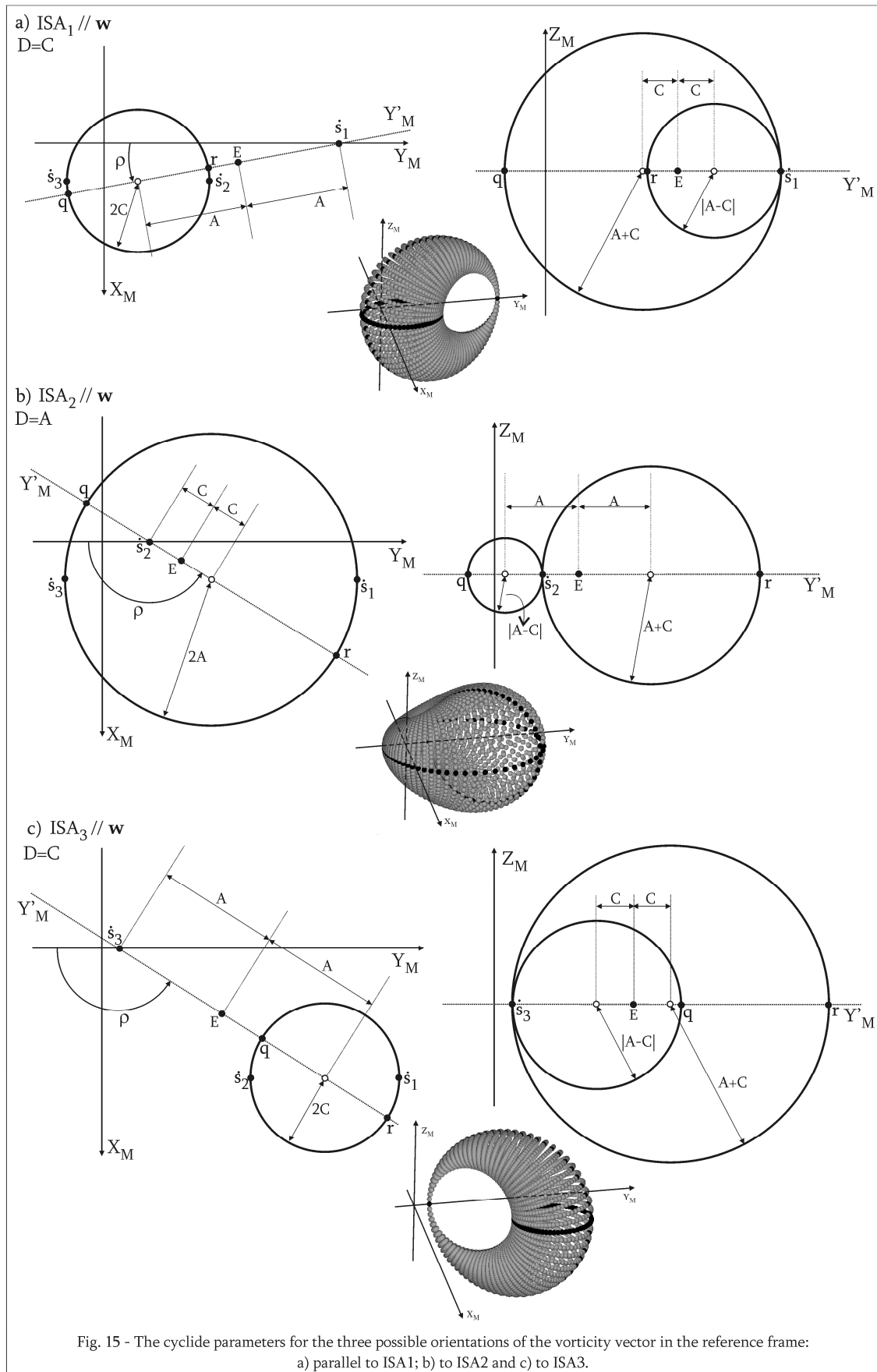
$$E = \begin{cases} E_x = \frac{w_i}{4} \\ E_y = \frac{2\dot{s}_i + \dot{s}_j + \dot{s}_k}{4} \end{cases}$$

Table 5 – Parameters for flow Mohr-cyclides.

ISA <sub>z</sub>	Cyclide shape	Cyclide parameters (vorticity parallel to z – Eq. 29; Fig. 15)				
		A	C	D	Ex	Ey
ISA <sub>1</sub>	Single-crescent	$\sqrt{(E_y - s_z)^2 + E_x^2}$	$\frac{ s_x - s_y }{4}$	C	$\frac{w_z}{4}$	$\frac{s_x + s_y + 2s_z}{4}$
ISA <sub>3</sub>						
ISA <sub>2</sub>	Torus	$\frac{ s_x - s_y }{4}$	$\sqrt{(E_y - s_z)^2 + E_x^2}$	A		
ISA <sub>y</sub>	Cyclide shape	Cyclide parameters (vorticity parallel to y – Eq. 30)				
		A	C	D	Ex	Ey
ISA <sub>1</sub>	Single-crescent	$\sqrt{(E_y - s_y)^2 + E_x^2}$	$\frac{ s_x - s_z }{4}$	C	$\frac{w_y}{4}$	$\frac{s_x + 2s_y + s_z}{4}$
ISA <sub>3</sub>						
ISA <sub>2</sub>	Torus	$\frac{ s_x - s_z }{4}$	$\sqrt{(E_y - s_y)^2 + E_x^2}$	A		
ISA <sub>x</sub>	Cyclide shape	Cyclide parameters (vorticity parallel to x – Eq. 31)				
		A	C	D	Ex	Ey
ISA <sub>1</sub>	Single-crescent	$\sqrt{(E_y - s_x)^2 + E_x^2}$	$\frac{ s_y - s_z }{4}$	C	$\frac{w_x}{4}$	$\frac{2s_x + s_y + s_z}{4}$
ISA <sub>3</sub>						
ISA <sub>2</sub>	Torus	$\frac{ s_y - s_z }{4}$	$\sqrt{(E_y - s_x)^2 + E_x^2}$	A		

As before,  $B^2 = A^2 - C^2$  and  $D$  is equal to  $C$  or  $A$ . Figure 15 illustrates the case where  $\vec{w}$  is parallel to  $zz$ , ie., when  $\vec{w}$  has only  $w_z$  components (Eq. 29), but the construction will be similar in all aspects for the other two orientations of  $\vec{w}$  (Eqs. 30 and 31). Table 5 summarises the parameters for all scenarios. Mohr coordinates for any point  $(\theta, \psi)$  will be obtained by substituting these parameters on Eq.2. This procedure produces the coordinates

$$\begin{aligned} X_M^\circ &= \frac{B \sin \psi (C \cos \theta - D)}{A - C \cos \theta \cos \psi} \\ Y_M^\circ &= \frac{D(C - A \cos \theta \cos \psi) + B^2 \cos \theta}{A - C \cos \theta \cos \psi} \\ Z_M^\circ &= \frac{B \sin \theta (A - D \cos \psi)}{A - C \cos \theta \cos \psi} \end{aligned} \quad (\text{Eq.2})$$



which define a cyclide with appropriate shape and parameters, but symmetric with respect to the  $Y_M Z_M$ - and  $X_M Y_M$ -planes. Because flow may have an asymmetric component, it is necessary to define an angle to rotate the parametric cyclides, in order to assure geometrical correspondence with their tensor. This is easily accomplished with the general rotation tensor  $\mathbf{R}_{ij}$ :

$$R_{ij} = \begin{vmatrix} \cos \rho & \sin \rho & 0 \\ -\sin \rho & \cos \rho & 0 \\ 0 & 0 & 1 \end{vmatrix} \quad (\text{Eq.38})$$

where the rotation vector is normal to  $Z_M$  (because symmetry in the  $X_M Y_M$ -plane is desirable following the convention for  $\delta$ ) and the rotation angle  $\rho$  is the angle between the negative  $Y_M$  and the cyclide vertical symmetry plane.  $\rho$  can be found by the expressions:

$$\rho = \arctan\left(\frac{w_i}{2\dot{s}_1 - \dot{s}_2 - \dot{s}_3}\right) \text{ if } \dot{s}_i > E_y, \text{ or}$$

$$\rho = 180^\circ - \arctan\left(\frac{w_i}{2\dot{s}_1 - \dot{s}_2 - \dot{s}_3}\right) \text{ if } \dot{s}_i < E_y \quad (\text{Eq.39})$$

which, since they are equivalent to:

$$\tan \rho = \frac{W_K}{A_K - 2T_K}, \quad (\text{Eq.40})$$

characterize  $\rho$  as a gauge for non-coaxiality of the flow: for  $\rho=0^\circ$ ,  $W_K$  is zero, the flow is coaxial and the cyclide is symmetric in the  $Y_M Z_M$ -plane. By convention,  $\rho$  is measured counter-clockwise for flows with  $W_K > 0$  and clockwise if  $W_K < 0$ . The rotated coordinates of the parametric Mohr-cyclide can now be obtained by simple multiplication of  $X_M^\circ$ ,  $Y_M^\circ$ ,  $Z_M^\circ$  by  $\mathbf{R}_{ij}$ :

$$\begin{aligned} X_M &= X_M^\circ \cdot \cos \rho - Y_M^\circ \cdot \sin \rho + E_x \\ Y_M &= X_M^\circ \cdot \sin \rho + Y_M^\circ \cdot \cos \rho + E_y \\ Z_M &= Z_M^\circ \end{aligned} \quad (\text{Eq.41})$$

Again, the components of parameter  $E$  must be added to removed the cyclide centre from the origin.

The third method to draw Mohr-cyclides gives an outline of their shape and uses the tensor components directly, in a way similar to the plotting scheme proposed by Means (1982) and described in Chap. 2 (Fig.16). The construction for a flow tensor with  $\dot{s}_x < \dot{s}_y < \dot{s}_z$  and  $ISA_1$  parallel to  $\vec{w}$  at  $zz$ -axis, proceeds as follows:

- 1)  $\mathbf{L}_{ij}$ 's reference axes (the  $ISA$ , Eq.29) are plotted in Mohr-space with coordinates:

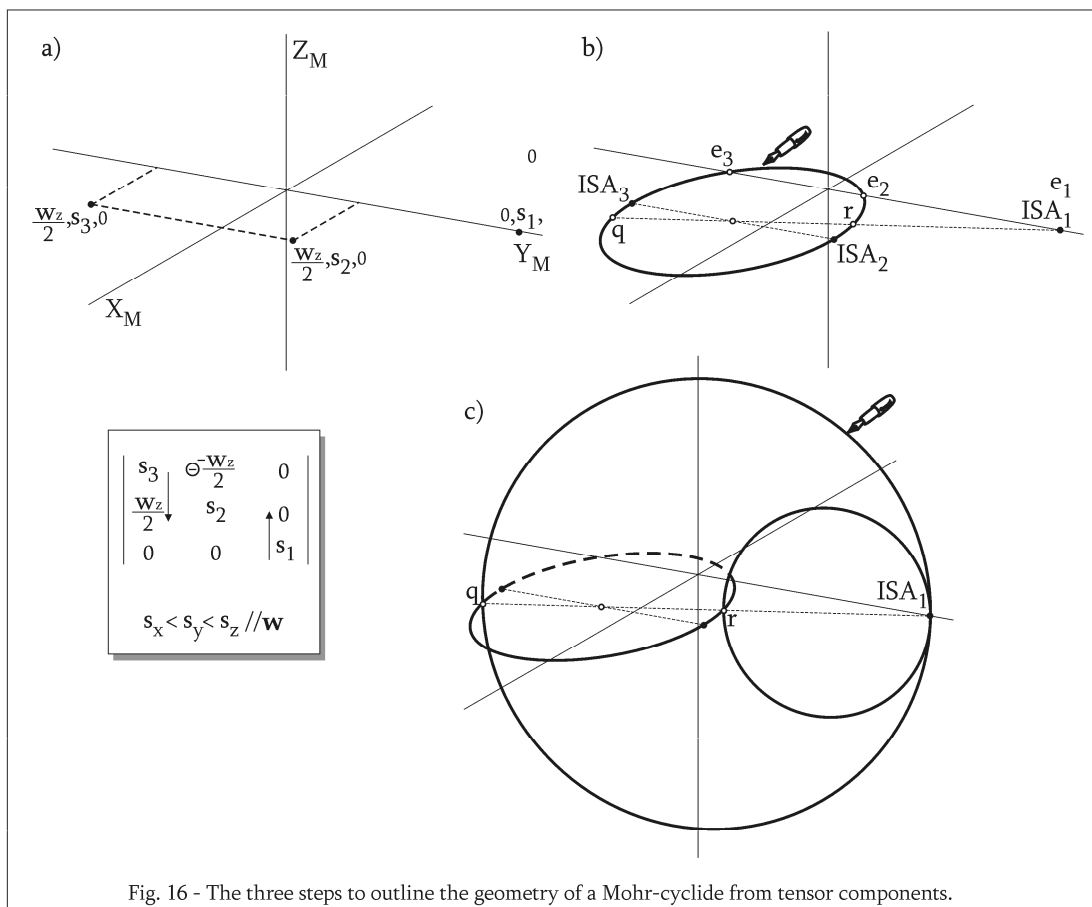
$$\begin{aligned}
 \text{ISA}_1: \{0, \dot{s}_1, 0\} & \text{ (component reversal)} \\
 \text{ISA}_2: \{w_z / 2, \dot{s}_2, 0\} & \text{ (sign change)} \\
 \text{ISA}_3: \{w_z / 2, \dot{s}_3, 0\} & \text{ (component reversal; Fig.16a)}
 \end{aligned}
 \tag{Eq.43}$$

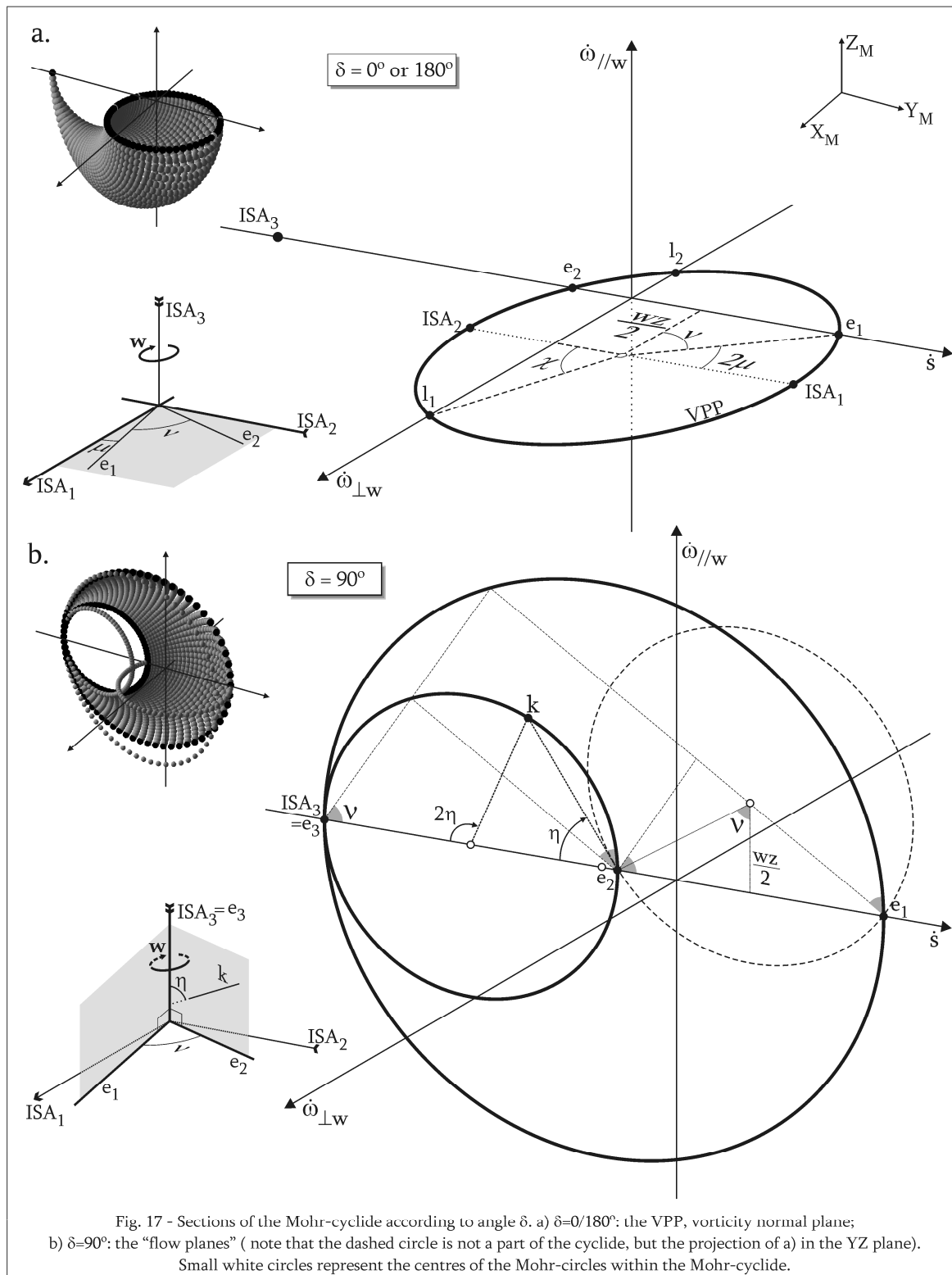
2)  $\text{ISA}_2$  and  $\text{ISA}_3$  (in this example) define a diameter of a circle, parallel to  $Y_M$ . This circle is the equivalent of two-dimensional Mohr-diagrams and intersects  $Y_M$  at  $e_2$  and  $e_3$ , two eigenvectors of  $L_{ij}$ . The line connecting the centre of the circle and  $\dot{s}_1$  intersects the circle at points  $q$  and  $r$  (Fig.16b).

3) Line segments  $\text{ISA}_1-r$  and  $\text{ISA}_1-q$  define the diameters of two additional vertical circles. These three circles are the three major circles of a single crescent cyclide (Fig.16c) or a torus, in the case of  $\text{ISA}_2$  parallel to  $\vec{w}$ .

Summarising, Mohr-cyclides for monoclinic flow can be:

- 1) Accurately plotted using polar coordinates (Eq.36; Fig.14);
- 2) Accurately plotted using parametric equations (Eq.41; Table 5; Fig.15);
- 3) Outlined from tensor components (Fig.16).





### 3.4. Interpretation

The previous section described three ways to build cyclides for asymmetric tensors with an eigenvector parallel to the reference frame; the following paragraphs will address their interpretation as Mohr-cyclides for monoclinic flow.

#### 3.4.1. Reference frame and special sections

In two dimensions (Fig.12), the abscissa  $Y_M$  in Mohr space is labelled  $\dot{s}$ , the stretching rate, whereas the ordinate  $X_M$  stands for  $\dot{\omega}$ , the rate of angular velocity. Expanding Mohr space to three dimensions creates another reference axis,  $Z_M$ . The physical meaning of this extra coordinate is related to the significance of angle  $\delta$ , defined, as seen above, with respect to  $\vec{w}$ :  $Z_M$  represents a second angular velocity rate, measured parallel to the vorticity vector, and not a second stretching rate. Thus, the coordinates of a point in a Mohr-cyclide for flow represent:

- 1)  $X_M$  :  $\dot{\omega}_{(\perp \vec{w})}$ , component of the angular velocity rate normal to the vorticity vector;
- 2)  $Y_M$  :  $\dot{s}$ , stretching rate (as in 2D);
- 3)  $Z_M$  :  $\dot{\omega}_{(\vec{w})}$ , component of angular velocity rate parallel to the vorticity vector.

A cyclide is a three-dimensional surface and, as such, can be cut in all directions in space. Some of these cross-sections have special significance when the cyclide is interpreted as a Mohr-diagram for flow. Angle  $\delta$  defines two of these important sections (Fig.17):

1)  $\delta=0^\circ, \delta=180^\circ$  (Fig.17a) characterises lines where the displacement vector  $\vec{d}$  is normal to  $\vec{w}$ , ie, particles moving in the plane normal to vorticity, the VPP (*vorticity profile plane* cf. Robin and Cruden, 1994). Accordingly, in Mohr-space, these particles plot as a circle in the  $X_M Y_M$ -plane, with  $Z_M=0$  and, therefore, there is no angular velocity component parallel to  $\vec{w}$ . This circle includes the ISA and the eigenvectors normal to vorticity, as well as  $\mathbf{l}_1$  and  $\mathbf{l}_2$ , the lines of no instantaneous stretch. The  $\delta=0^\circ$  circle is also a symmetry plane of the cyclide and, thus, one of the defining circles of its parametric equations. It is essential to point out that this circle is also the equivalent of 2D Mohr-circles in the Mohr-cyclide (compare with Fig.12; proof in section 5.1.), always defined in the VPP. Thus, the coordinates of the centre can also be read as gauges for the  $W_K$  and  $A_K$  parameters.

2)  $\delta = 90^\circ$  (Fig.17b) is the geometrical locus of particles with  $\vec{d}$  in planes that contain the vorticity vector and one of the  $\vec{w}$  normal eigenvectors (the flow apophyses). The eigenvector planes, do not have an angular velocity component normal to  $\vec{w}$  and  $X_M=0$ . Depending on the number of real (non-imaginary) eigenvalues of  $\mathbf{L}_{ij}$ , there can be 2, 1 or no planes with  $\delta=90^\circ$ . In the example of Figure 17b,



A second set of sections through the cyclide, with geological meaning in terms of monoclinic flow, are the principal sections of the *instantaneous stretching ellipsoid* (Fig.18). These sections are circles within the cyclide, defined by diameters comprising the ISA coordinates (Eq.43). If flow is coaxial, the sections of the instantaneous stretching ellipsoid are identical to the principal circles of the cyclide. For non-coaxial flow, they are not identical and the diameters of circles  $ISA_1ISA_3$  and  $ISA_1ISA_2$  are related by an angle which only has expression in the Mohr-cyclide. In geographical space, the ISA planes are, by definition, at  $90^\circ$  of each other. The existence of this angle is not conflicting with this statement because, in the Mohr-cyclide, the ISA plot at opposite ends of diameter and, therefore, are orthogonal via the double-angle rule of Mohr-circles. Representation of these sections in a typical 2D Mohr-diagram requires more sophisticated construction methods, such as the *locii* of Treagus (1986, 1990), which, although geometrically flawless, are not as intuitive as plain circles.

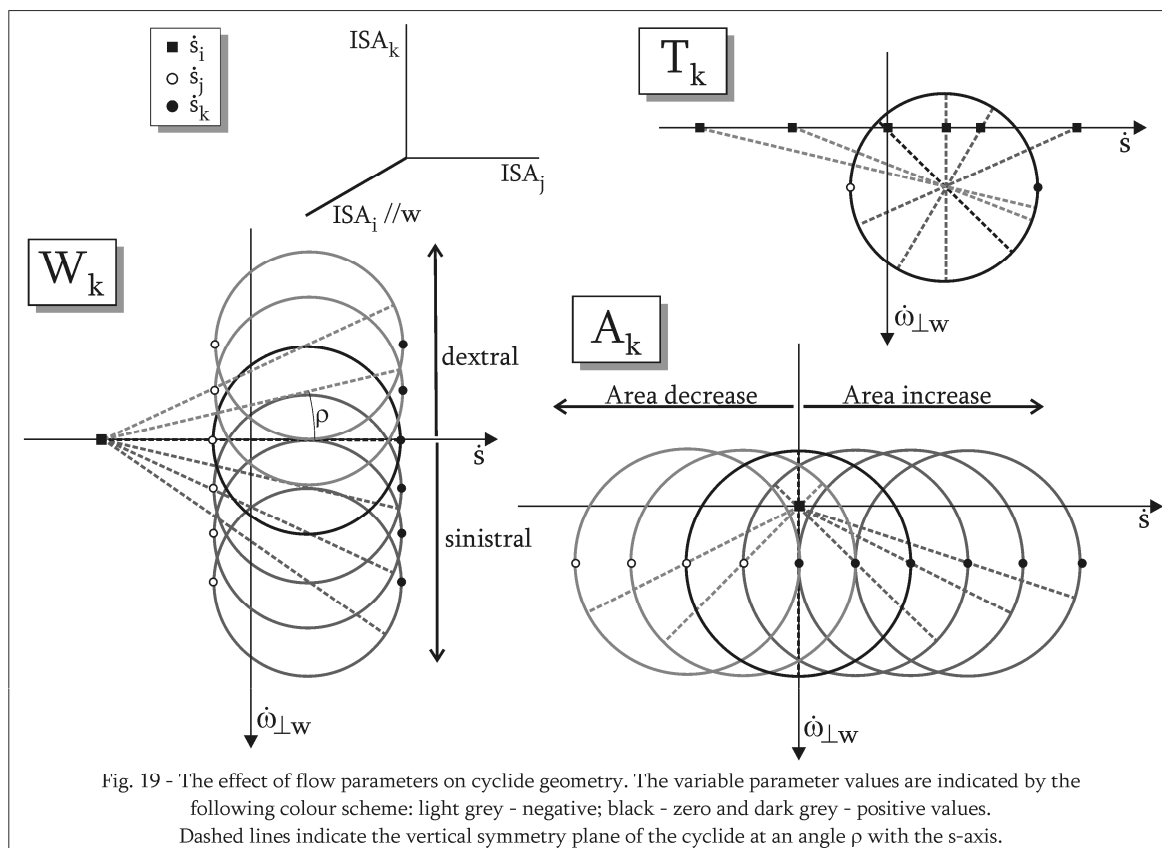
The special sections of Mohr-cyclides are excellent examples of a useful property of cyclides, which states that all lines in their curvature are circles (Allen and Dutta, 1997; Shene, 2000). From this, it follows that Mohr-cyclides are, in fact, a collection of an infinite number of Mohr-circles defined by their orientations with respect to a reference axis, the vorticity vector, in the case of flow-cyclides. The paradigm of this statement is the cyclide section normal to vorticity (Fig.17a), the three-dimensional equivalent of the 2D Mohr-circle for flow. This allows Mohr-cyclides the power to represent, in a simple way, multiple orientations in space, including the vorticity profile plane, the shear zone boundary and odd outcrop surfaces, defined by geomorphological fancy, more often than not in conflict with the structural geologist's convenience.

### 3.4.2. Influence of flow parameters

All monoclinic flows can be efficiently described with four flow numbers,  $\dot{s}_i$ , the stretching rates along the ISA, and  $\bar{w}$ , the magnitude of the vorticity vector, which can be combined to define three kinematic numbers, or flow parameters,  $W_k$ ,  $A_k$ ,  $T_k$ ;  $V_k$  is not independent (Passchier, 1997). Figure 19 illustrates the relative influence of the flow parameters on the Mohr-cyclides.

For constant stretching rate values, the kinematic vorticity number,  $W_k$ , slides the basal section of the cyclide in the direction parallel to the  $\hat{\omega}_{\perp w}(Y_M)$ -axis. This is similar to  $W_k$ 's effect on Mohr-circles (Fig.13) but, in 3D, the cyclide remains pinned to the stretching rate of the ISA parallel to vorticity. This means that, considering the whole surface,  $W_k$  actually rotates the cyclide around a rotation axis parallel to the  $\hat{\omega}_{//w}(Z_M)$ -axis at  $\dot{s}_i$ . The result is an increasing value of angle  $\rho$  (Eq.40) which correlates with increasing grades of non-coaxiality. Keeping  $W_k$  and  $\dot{s}_i$  constant, the effect of  $A_k$

depends on the stretching rates normal to vorticity,  $\dot{s}_j$  and  $\dot{s}_k$ , and, as for  $W_k$ , is superficially similar to the observed in Mohr-circles.  $A_k$  slides the basal plane of the cyclide in the  $\dot{s}$ -axis, consequence of a rotation controlled by a rotation vector fixed parallel to the  $\dot{\omega}_{\perp w}$  ( $Z_M$ )-axis at  $\dot{s}_i$ . The effect of  $T_k$  cannot be gauged in Mohr-circles, due to their geometric restrictions, but is ready for inspection on Mohr-cyclides. Allowing variation in  $\dot{s}_i$ , while keeping  $\dot{s}_j$  and  $\dot{s}_k$  constant reveals a slide of the apex of the cyclide in the  $\dot{s}$ -axis.



### 3.4.3. Geometries and examples of Mohr-cyclides

As stated in section 2.3., there are different types of Mohr-cyclides, consistent with the geometries allowed in the cyclide family of surfaces (Table 2). For monoclinic flow described with equations 29-31, the type of Mohr-cyclide depends first on the relative orientation of the ISA reference frame with respect to the vorticity vector and, second, on the magnitude of the instantaneous stretching axis parallel to it. Or, to put it simple, the answer lies in the questions: which ISA is parallel to vorticity? what is the relative magnitude of this ISA?

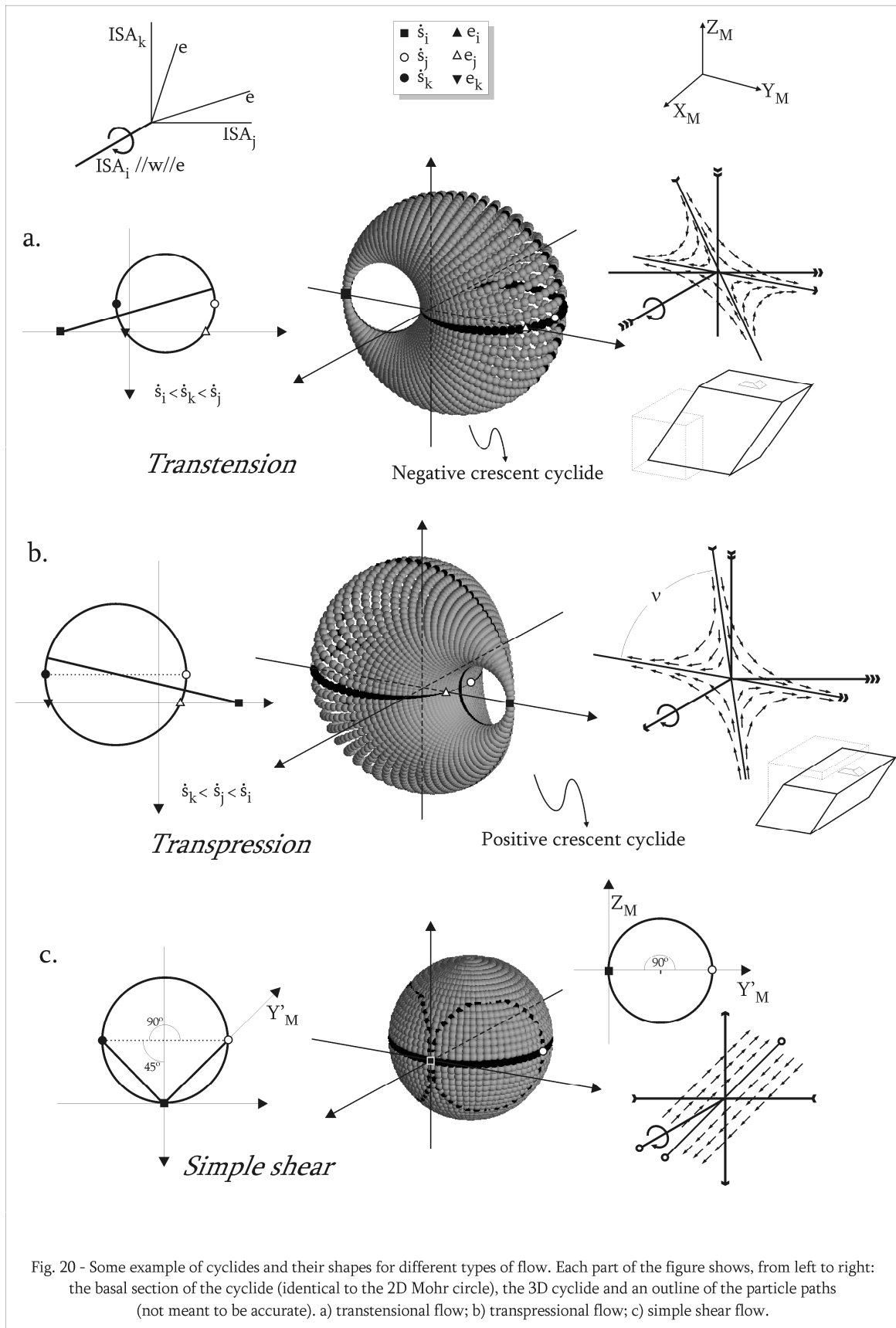


Fig. 20 - Some example of cyclides and their shapes for different types of flow. Each part of the figure shows, from left to right: the basal section of the cyclide (identical to the 2D Mohr circle), the 3D cyclide and an outline of the particle paths (not meant to be accurate). a) transensional flow; b) transpressional flow; c) simple shear flow.

Figure 20 illustrates shape variations of Mohr-cyclides of major flow types, using examples where  $\vec{w}$  is parallel to the  $i$ -axis (Eq.29-31),  $\dot{s}_j > \dot{s}_k$  and the value of  $\dot{s}_i$  is variable; this is equivalent to a case where flow parameter  $T_k$  is allowed to change. Subscripts  $i,j,k$  are preferred here because the geometry of Mohr-cyclides depends more on the relative magnitude of principal stretching rates than on their absolute value and is completely independent of their real orientation, as long as the ISA are pinned to a reference frame. Another feature that is important to decide which shape a Mohr-cyclide will assume is the number of eigenvectors of  $\mathbf{L}_{ij}$  ( $e$ ) and their eigenvalues  $\dot{e}_i$ , compared to the stretching rate parallel to vorticity. Note that the convention  $\dot{s}_j > \dot{s}_k$  implies  $\dot{e}_j > \dot{e}_k$ . For simplicity, this discussion is mainly based on isochoric flows, but the same principles will also apply to situations with volume change.

a) **Transtensional flow** (Sanderson and Marchini, 1984) is characterised by an area increase in the  $ISA_j$ - $ISA_k$  plane, compensated by shortening in the direction of  $\vec{w}$ . In terms of stretching rates, this definition implies  $\dot{s}_i < 0$ ,  $\dot{s}_i < \dot{s}_j + \dot{s}_k$  and allows  $\dot{s}_i < \dot{s}_k$  as well as  $\dot{s}_i > \dot{s}_k$ . In isochoric flow, this means  $A_k = -T_k$ . Transtension can be represented in Mohr-space by two surfaces of the cyclide family. The transition between the two shapes is governed by the relative magnitude of  $\dot{s}_i$  and eigenvalues  $\dot{e}_j, \dot{e}_k$ : if  $\dot{e}_j < \dot{s}_i < \dot{e}_k$ , the Mohr-cyclide will be a *torus with a vanishing point* at  $\dot{s}_i$  (Fig.21 below); if  $\dot{s}_i < \dot{e}_j, \dot{e}_k$ , the Mohr-cyclide will be a *negative crescent cyclide* (Fig.20a), a crescent cyclide “facing” the negative end of  $Y_M$ .

b) The counterpart of transtension is **transpressional flow** (Sanderson and Marchini, 1984), where area decrease on the  $ISA_j$ - $ISA_k$  plane is balanced with stretching in the direction of  $\vec{w}$ . Translating into stretching rate values, the conditions for transpression are  $\dot{s}_i > 0$ ,  $\dot{s}_i > \dot{s}_j + \dot{s}_k$ , with  $\dot{s}_i > \dot{s}_j$  or  $\dot{s}_i < \dot{s}_j$ . Transpression can be illustrated by *positive crescent* Mohr-cyclides (cyclides “facing” the positive end of  $Y_M$ ) for  $\dot{s}_i > \dot{e}_j, \dot{e}_k$  (Fig.20b) or *torii with a vanishing point* at  $\dot{s}_i$  for  $\dot{e}_j > \dot{s}_i > \dot{e}_k$  (Fig.21 below). It is important to note that transpression and transtension are always indistinguishable in 2D Mohr-circles, because these diagrams consider only one section of the bulk flow. Mohr-cyclides include information about stretching rate parallel to vorticity and, thus, allow the differentiation of these two types of flow.

c) **Simple shear** or **parallel flow** is the simplest form of non-coaxial flows, with no volume change and characterised by a kinematic vorticity number  $W_k = 1$  or  $W_k = -1$  ( $|2w_i| = |\dot{s}_j - \dot{s}_k|$ ). To ensure laminar flow,  $T_k = A_k = 0$ , which means that simple shear is always isochoric. Unlike the previous examples, the Mohr-diagram for simple shear flow is nor a cyclide nor a torus, but a plain and homely

*sphere*. This is not in contradiction with the statement that 3D Mohr-diagrams are surfaces from the cyclide family because, as seen in chapter 2.3.3., they represent a continuum in the group and the transition between single crescent cyclides and torii with vanishing points. The sphere touches the  $\dot{s}$ -axis of the Mohr-diagram only at the origin (Fig.20c), which is consistent with the fact that flow tensors for simple shear have only one eigenvector. The eigenvector lies as expected in the plane normal to  $\vec{w}$ , at 45° with the instantaneous stretching axes. The instantaneous stretching axes are orthogonal, as read, in the form of double-angles, on their respective planes.

Spherical surfaces are not exclusive of simple shear flows (with one eigenvector), as they occur whenever  $\dot{s}_i$  equals the stretching rate of one of the eigenvectors in the  $ISA_jISA_k$ -plane. This circumstance, however possible, represents a special case of the Cardano condition, when two of the three real eigenvalues coincide.

d) **Pure shear**, or coaxial flow, occurs when the eigenvectors of the flow coincide with the instantaneous stretching axes, which translates in  $W_K=0$ . Mohr-cyclides for pure shear flow can be represented by different kinds of surfaces, including negative and positive single crescent cyclides, torii, spheres and circles, since the relative magnitudes of  $\dot{s}_i$ ,  $\dot{s}_j$  and  $\dot{s}_k$  are not relevant. However, they have one thing in common: whatever the shape, the Mohr-cyclide will be symmetric with respect to both the  $X_M Y_M$ - and the  $Y_M Z_M$ -planes and the  $ISA_j ISA_k$  circle will be centred on the  $Y_M (\dot{s})$ -axis. The reason for this is the angular velocity of the instantaneous stretching axes, zero at all times following the definition of coaxial flow, implies that  $\dot{\omega}_{(\perp \vec{w})} = \dot{\omega}_{(\vec{w})} = 0$  ( $X_M = Z_M = 0$ ).

f) **Rotational flow**, or super simple shear (Simpson and De Paor, 1993) occurs whenever the kinematic vorticity number  $W_K$  has an absolute value greater than 1. Translating this condition into tensor algebra, it follows that a rotational flow tensor has only one non-imaginary real eigenvalue, in the direction parallel to  $\vec{w}$ . These special cases produce negative or positive crescent shaped Mohr-cyclides, but never torii surfaces, which require three real eigenvalues. Rotational flows are easily identified by Mohr-cyclides which touch the  $\dot{s}$ -axis only in one point, at the stretching rate correspondent to the ISA parallel to vorticity,  $\dot{s}_i$  in this example.

g) **Outward-** and **inward-radiant** flow types (Passchier, 1991) are defined by Mohr-cyclides of all shapes, located entirely on the positive or negative  $\dot{s}$ -axis. Although mathematically possible, the existence of these flow types in Geology is somewhat unrealistic, since they represent either “exploding” or “imploding” flows with extreme volume change. The extreme case of outward- or inward-radiant flows occurs for  $A_K = \infty$ . On this particular condition, the Mohr-cyclide will be a *circle*. Just as spheres, circles represent a special case of the cyclide family, characterised by  $\dot{s}_j = \dot{s}_k$ .

The discussion so far can be summarised with the example a tensor defined by (Fig.21):

$$L_{ij} = \begin{vmatrix} 0.5 & 0 & 0 \\ 0 & -2 & 0.75 \\ 0 & -0.75 & 1.5 \end{vmatrix} \text{ in the form } L_{ij} = \begin{vmatrix} \dot{s}_x & 0 & 0 \\ 0 & \dot{s}_y & -w_x/2 \\ 0 & w_x/2 & \dot{s}_z \end{vmatrix} \quad (\text{Eq.31})$$

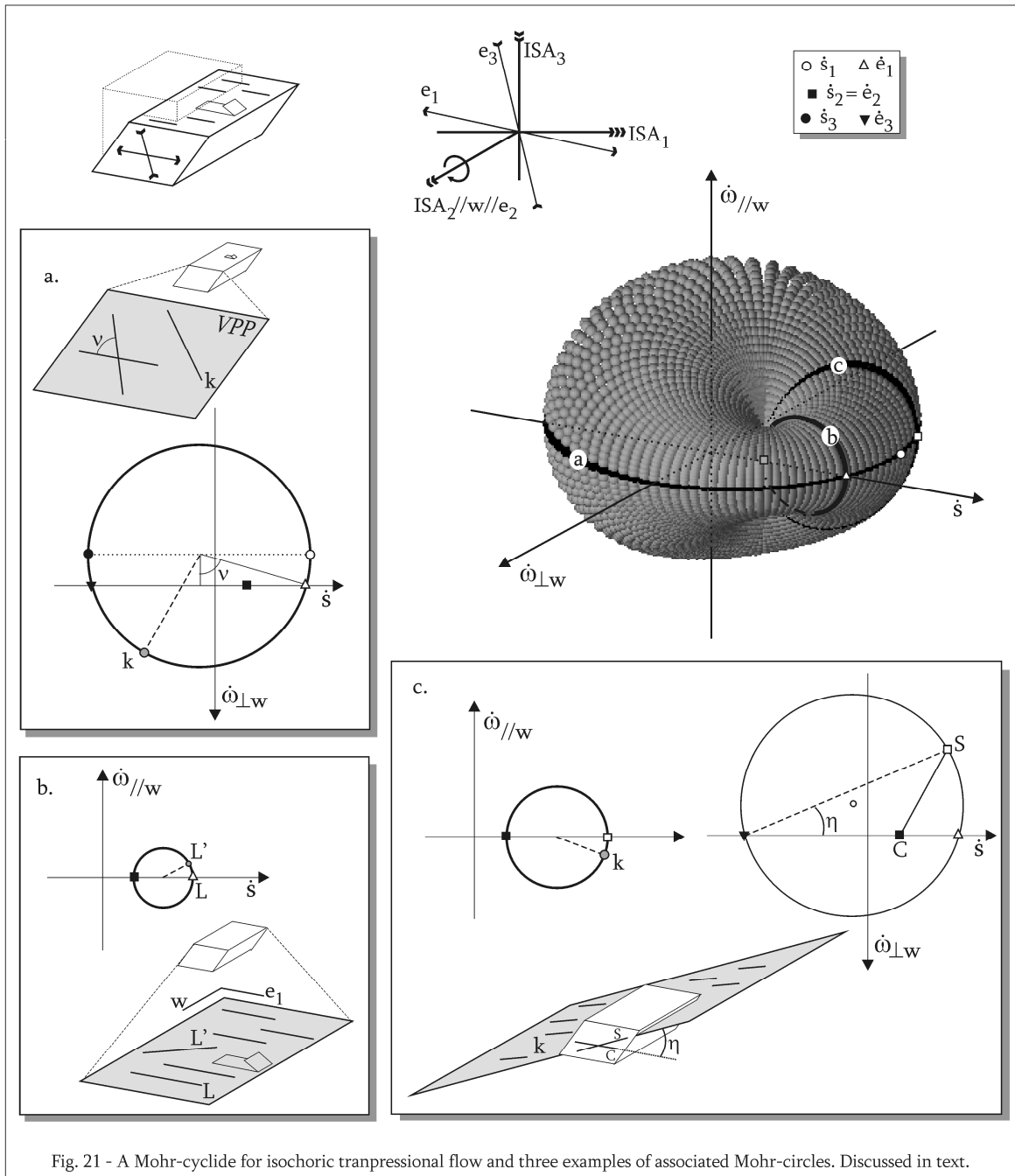


Fig. 21 - A Mohr-cyclide for isochoric transpressional flow and three examples of associated Mohr-circles. Discussed in text.

From  $\mathbf{L}_{ij}$  components it is possible to deduce that:

- a)  $\dot{s}_z < \dot{s}_x < \dot{s}_y$ , which means that ISA<sub>1</sub> is parallel to the  $yy$ -axis in the reference frame, ISA<sub>2</sub> to the  $xx$ -axis and ISA<sub>3</sub> to the  $zz$ -axis.
- b) Since  $\dot{s}_x = \dot{s}_y + \dot{s}_z$ ,  $T_k = -A_k$ , and the flow is isochoric.
- c) The vorticity vector is defined by a negative component and is parallel to ISA<sub>2</sub> at  $xx$ ; shear sense is dextral since  $W_k < 0$ ; the vorticity profile plane (VPP) lies at ISA<sub>1</sub>ISA<sub>3</sub>.
- d) The relative magnitude of the principal stretching rates suggests that an area decrease in the VPP is compensated by extension in the direction of ISA<sub>2</sub>.
- e) a-d) characterise a *transpressional dextral flow*.
- f) Quick calculation of the eigenvectors of  $\mathbf{L}_{ij}$  shows that the eigenvalue parallel to vorticity is the intermediate ( $\dot{e}_2$ ); from this it follows that an eventual material line attractor (Passchier 1997) will be parallel to  $e_1$  in the VPP.

Eq. 41, applied to this example  $\mathbf{L}_{ij}$  returns the torus illustrated on Figure 21, with a converging point at  $\dot{s}_x$  ( $\dot{e}_2$ ) that represents the direction of the vorticity vector. This cyclide can be sliced in multiple circular sections, some with special significance as described above, which can be interpreted as a single Mohr-circle. Three of these sections are:

Figure 21a shows the vorticity profile plane (VPP) corresponds to the basal cyclide circle, which contains the two eigenvectors and the two ISA normal to  $\vec{w}$ . This is the plane where structure asymmetry is more obvious and where shear sense should be gauged. This section of the cyclide is identical to the Mohr-circle for a 2D simplification and can be interpreted just in the same way.

Figure 21b represents the flow plane (in the sense of Passchier 1998), the eigenvector plane which contains the extensional (positive) eigenvalue. The boundary of a shear zone developed according to this flow type will lie parallel to. The flow plane can be considered, for practical reasons, the plane of foliation, where the lineation L can be observed and measured in the field. An eventual second lineation L', will plot as a line in this section of the Mohr-cyclide.

Figure 21c illustrates a plane which contains the vorticity vector, but lies at an angle with the eigenvectors and instantaneous stretching axes. This plane can represent, for instance, an “S-foliation” in a C+S pair, which can be used for shear sense determination. Sometimes it is possible to observe striations in these planes (eg Lin et al. 1998) that can give additional kinematic information. Such lines can also be represented in the Mohr-cyclide.

In summary, Mohr-cyclides, since they are not limited to 2D as Mohr-circles, allow the representation of multiple structural features in the same diagram. These may include different planes with geological meaning (or not), and all types of lineations included in them.

## 4. Mohr-cyclides for deformation

### 4.1. Deformation tensors

Deformation in rocks can be described as the combined effect of two different mechanisms: distortion or strain and rigid rotation (Fig.22a). Considering a material line  $k$ , distortion will produce a change in length, named *stretch*  $S$ , defined as (eg Ramsay and Huber, 1983):

$$S = \frac{k_f}{k_0} \quad (\text{Eq.32})$$

where  $k_f$  and  $k_0$  are the final and original lengths of  $k$ . The stretch of a line can be normalised to unit length, resulting in *elongation*  $\hat{\epsilon}$ :

$$\hat{\epsilon} = \frac{k_f - k_0}{k_0} = S - 1 \quad (\text{Eq.33})$$

which, in turn, can be used to define the *quadratic elongation*  $\lambda$ :

$$\lambda = \left( \frac{k_f}{k_0} \right)^2 = S^2 = (\hat{\epsilon} + 1)^2 \quad (\text{Eq.34})$$

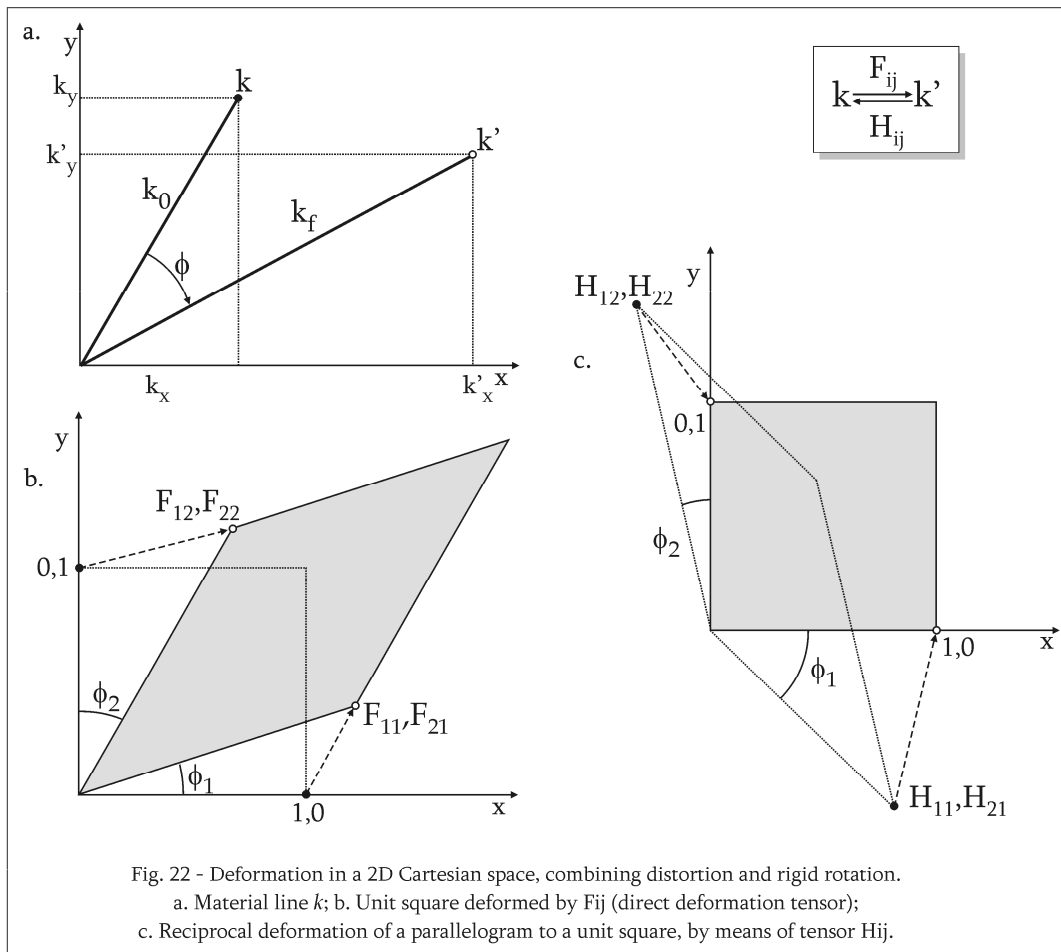
The combined effects of distortion and rotation of lines can be presented in a single operation by the *deformation tensor*  $\mathbf{F}_{ij}$ , also known as the displacement gradient tensor, which describes the transformation of a continuum from an undeformed to a deformed state (eg Ramsay 1967, Means et al. 1980, Ramsay and Huber 1983). Thus, any homogeneous two-dimensional deformation can be described as (Fig.22b):

$$k' = \mathbf{F}_{ij} \cdot k$$

$$\begin{cases} k'_x = F_{11}k_x + F_{12}k_y \\ k'_y = F_{21}k_x + F_{22}k_y \end{cases} \quad (\text{Eq.35})$$

In other words, deformation of a unit square, with sides parallel to the reference coordinate axes, transforms it to a parallelogram defined by the tensor operation. In this context, vertices originally at (1,0) and (0,1) acquire coordinates equal to  $\mathbf{F}_{ij}$  components, following Eq.35. Area change is gauged by the determinant of  $\mathbf{F}_{ij}$  ( $\det F$ ) as demonstrated, for instance, by Ramsay (1967), with  $\det F = 1$  implying constant area deformation. Note that if the determinant is negative, the deformed unit square, besides

normal deformation, also undergoes a mirror-image transformation. When  $\det F = 0$ , the unit square suffers an extreme area reduction to become a material line. Tensor operations do not account for translation, and, therefore, the particle at the origin of the coordinate system in the undeformed state remains at that location with progressive deformation.



For all deformations with  $\det F \neq 0$ , it is possible to define an inverse deformation, also of use in geological problems since it transforms the deformed state into the original undeformed state (Fig.22c). The tensor for this operation is  $\mathbf{H}_{ij}$ , the *reciprocal deformation tensor*. Reciprocal deformation can be described in a way analogous to Eq.35:

$$\begin{aligned}
 k &= H_{ij} \cdot k' \\
 \begin{cases} k_x = H_{11}k'_x + H_{12}k'_y \\ k_y = H_{21}k'_x + H_{22}k'_y \end{cases} & \quad (\text{Eq.36})
 \end{aligned}$$

$\mathbf{F}_{ij}$  and  $\mathbf{H}_{ij}$  are inverse of each other and are related by the expression:

$$H_{ij} = \begin{bmatrix} H_{11} & H_{12} \\ H_{21} & H_{22} \end{bmatrix} = F_{ij}' = \begin{bmatrix} F_{22}/\det F & -F_{12}/\det F \\ -F_{21}/\det F & F_{11}/\det F \end{bmatrix} \quad (\text{Eq.37})$$

The parameters used to describe reciprocal deformation are, therefore, inverse to the ones defined in Eqs.32-34.

Besides  $\mathbf{F}_{ij}$  and  $\mathbf{H}_{ij}$ , it is possible to define more deformation tensors, but two have special significance. The Green tensor ( $\mathbf{G}_{ij}$ ) is defined by (eg Spencer 1980):

$$G_{ij} = F_{ij}^T \cdot F_{ij} \quad (\text{Eq.38})$$

and gives the quadratic elongation  $\lambda$  of any unit line  $k$ , following a deformation described by  $\mathbf{F}_{ij}$ .  $\mathbf{G}_{ij}$  is, per its definition, always a symmetrical tensor and, it turns out, a very useful one: the eigenvectors and eigenvalues of  $\mathbf{G}_{ij}$  give the directions and magnitudes of the maximum and minimum quadratic elongations induced by the deformation. In other words,  $\mathbf{G}_{ij}$  fully describes the strain ellipse (or ellipsoid). The Cauchy tensor  $\mathbf{C}_{ij}$  is obtained in a similar way:

$$C_{ij} = H_{ij}^T \cdot H_{ij} \quad (\text{Eq.39})$$

and gives the reciprocal quadratic elongations  $\lambda'$  of any line  $k$ , following a reciprocal deformation  $\mathbf{H}_{ij}$ .  $\mathbf{C}_{ij}$  can be interpreted in an analogous way, with respect to the reciprocal strain ellipse (or ellipsoid).

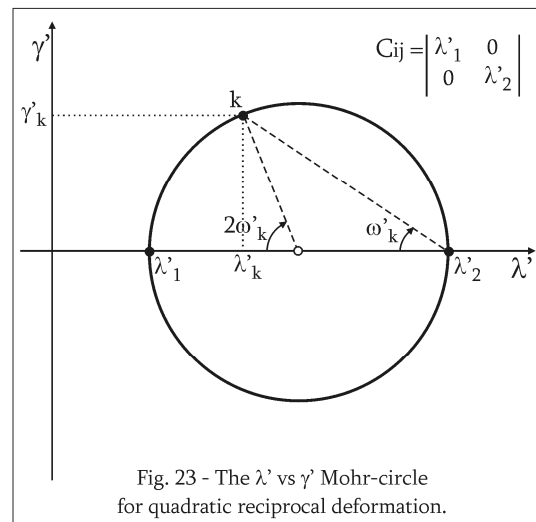
## 4.2. Mohr-circles for deformation

### 4.2.1. The $\lambda$ vs. $\gamma$ plots

The concept of Mohr-circles was first adapted for deformation tensors by Nadai (1950), who introduced plots for direct and reciprocal deformation, plotting quadratic elongation vs. shear strain ( $\lambda$  vs.  $\gamma$ ), or the reciprocal quadratic elongation vs. gamma prime ( $\lambda'$  vs.  $\gamma'$ ; Fig.23).  $\gamma$  is the shear strain of a line and *gamma prime*  $\gamma'$  combines the effect of length and angular change in deformation:

$$\gamma' = \frac{\gamma}{\hat{e}} \quad (\text{Eq.40})$$

The  $\lambda'$  vs.  $\gamma'$  plot is the most used in structural geology since it uses data from deformed markers, such as fossils (for examples see for instance Ramsay and Huber 1983). Treagus (1986) expanded the idea to three-dimensional strain ellipsoids.



These types plots are related, respectively, with the Green and Cauchy deformation tensors. The construction of Mohr-circles for reciprocal strain starts with the definition of a circle of radius  $r$ , centred at  $c$  in the  $xx$ -axis of a coordinate reference frame, and defined by the following equations:

$$\begin{aligned} x &= c - r \cos \alpha \\ y &= r \sin \alpha \end{aligned} \quad (\text{Eq.41})$$

With the same reasoning, coordinates of line  $k$  on a Mohr-circle in a  $\lambda'$  vs.  $\gamma'$  space are expressed by:

$$\begin{aligned} \lambda'_k &= \frac{\lambda'_1 + \lambda'_2}{2} - \frac{\lambda'_2 - \lambda'_1}{2} \cos 2\omega_k \\ \gamma'_k &= \frac{\lambda'_2 - \lambda'_1}{2} \sin 2\omega_k \end{aligned} \quad (\text{Eq.42})$$

where  $\omega_k$  is the angle between  $k$  and the maximum reciprocal stretch ( $\lambda'_1$ ) (Fig.23). Alternatively, the  $\mathbf{G}_{ij}$  tensor can be plotted directly via the Means (1982) plotting scheme. The Lagrangian plot  $\lambda$  vs.  $\gamma$  and  $\mathbf{G}_{ij}$  follows the same rules.

#### 4.2.2. Mohr-circle for stretch

The second type of Mohr-circle for deformation is the *polar Mohr diagram* or *Mohr diagram for stretch*, introduced by Means (1982). This construction makes use of calibrated coordinate axes, assigned to  $F_{ii}$  and  $F_{ij}$  components of  $\mathbf{F}_{ij}$ . The deformation tensor  $\mathbf{F}_{ij}$  is plotted as described in section 1.2. (Fig.1 and 24a). Points with coordinates  $F_{11}, -F_{21}$  and  $F_{22}, F_{12}$  represent the orientation of material lines parallel to the  $xx$ - and  $yy$ -axis and are useful as a reference to describe other elements of deformation. The length of lines  $S_x$  and  $S_y$  represent the amount of stretch that these lines experienced during deformation. Change of orientation of lines is quantified by angles  $\phi_x$  and  $\phi_y$ . Maximum and minimum principal stretches (principal axes of the deformation ellipse),  $S_1$  and  $S_2$ , are the points in the Mohr circle furthest and closest, respectively, from the origin. They are located in a diameter centred in the origin of the coordinate system (Fig.24b), which is appropriate because the lines parallel to  $S_1$  and  $S_2$  are orthogonal in real space. In the case of non-rotational deformation, where the principal axes of the deformation ellipse do not rotate in the external reference frame,  $S_1$  and  $S_2$  represent the eigenvalues of  $\mathbf{F}_{ij}$  and plot on the horizontal  $xx$ -axis. The Mohr diagram allows to determine the orientation of  $S_1$  and  $S_2$  relative to the reference axes ( $F_{11}, -F_{21}; F_{22}, F_{12}$ ), with angles  $\theta$  ( $\wedge xx$ ) and  $\nu$  ( $\wedge yy$ ). In Fig.24b, only  $\theta$  is illustrated, but since both sets of lines are orthogonal,  $\nu$  is easily obtainable for both  $S_1$  and  $S_2$ . The idea can be generalised for deformed lines  $j, k$ , knowing their undeformed orientation  $j, k$  (Fig.24c). The Mohr-circle is especially useful for this analysis, because it predicts stretch ( $S_j, S_k$ ) and amount of rotation ( $\phi_j, \phi_k$ ) experienced by  $j, k$  in the deformation framework defined by tensor by  $\mathbf{F}_{ij}$ .

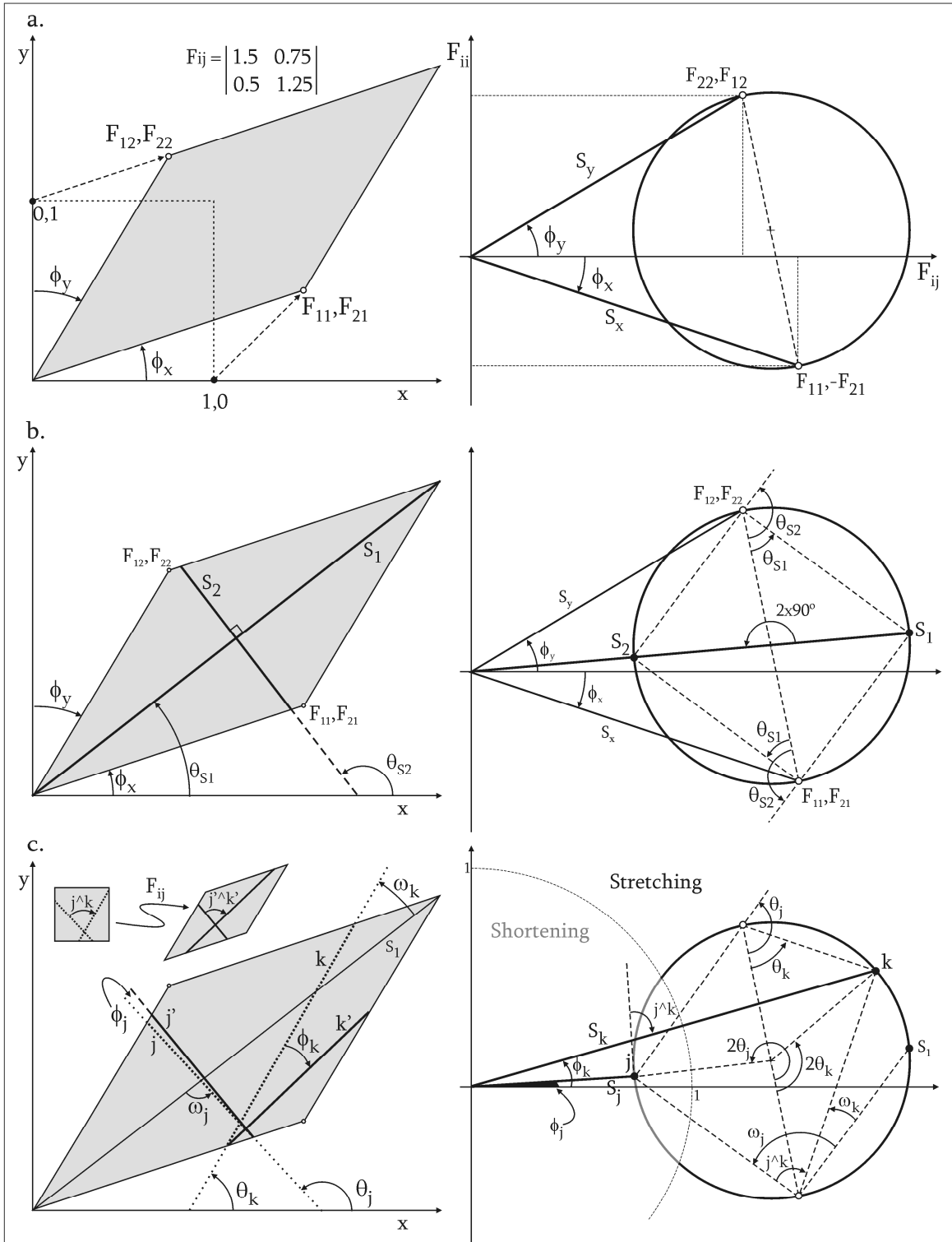


Fig. 24 - The polar Mohr diagram for deformation. a, Projection of tensor  $F_{ij}$ ; b, Principal stretches  $S_1$  and  $S_2$  in real and Mohr space; c, Undeformed (dashed) and deformed (solid) material lines  $j$  and  $k$  in real and Mohr space and their angular relationships.

Angles between an undeformed line and the maximum stretch direction ( $\omega_j$ ,  $\omega_k$ ) are found graphically, by taking  $F_{11}$ ,  $F_{21}$  as reference. Although this point was chosen for convenience, any point can be used for measuring angles because the Mohr diagram is a circle in 2D and, thus, subject to the circular theatre rule. Following the same principle, it is also possible to find angles between lines and coordinate axis ( $\theta_j$ ,  $\theta_k$ ) and between the lines themselves, in both deformed and undeformed states. It is important to note that inside the Mohr-circle (using its centre as reference), all these angles are measured as double angles. Another information that is readily available in a Mohr-circle is the distribution of line stretching and line shortening fields, based on a circle of radius 1. This imaginary circle intercepts the Mohr-circle at the points related where  $S=1$ , ie, no change in length. Points that plot inside this circle border represent shortening lines ( $S<1$ , grey in Fig.24c); points that plot outside represent lines which underwent an increase in length ( $S>1$ , black in Fig.24c).

The Mohr diagram for the reciprocal deformation  $\mathbf{H}_{ij}$  can be constructed and interpreted with the same principles. Since  $\mathbf{H}_{ij}$  is the inverse of  $\mathbf{F}_{ij}$  (Eq.37), the Mohr diagrams for the two tensors are mirror images of each other, for constant area deformations. The principal stretches are also inversely related.

### 4.3. Plotting procedures

Mohr-cyclides can be derived for the two varieties of Mohr-circles for deformation: the  $\lambda$  vs.  $\gamma$  plots proposed by Nadai (1950) and the stretching plots of Means (1982). Since they are based in different principles, the plotting procedure for the respective Mohr-cyclides will be equally distinct.

The  $\lambda$  vs.  $\gamma$  and  $\lambda'$  vs.  $\gamma'$  Mohr-circles are based, respectively, on the Green and Cauchy tensors. This means that both are symmetrical and they do not account for rotation, only strain.. The plotting rules and interpretation will, thus, be very similar to the situation described above for stress. Making the appropriate variable substitutions, this type of Mohr-cyclides can be plotted with Eqs. 7 and 10. Mohr-diagrams for stretch, on the other hand, are based on  $\mathbf{F}_{ij}$  and allow tensor asymmetry. The following discussion, in many ways similar to what was described for monoclinic tensors, focuses on monoclinic deformation tensors, and can also be applied straightforward also to  $\mathbf{H}_{ij}$  tensors.

The orientation of line  $k'$  following a finite deformation defined by  $\mathbf{F}_{ij}$  is given by Eq.36 (Fig.25a):

$$k' = F_{ij} \cdot k \quad (\text{Eq.36})$$

If  $k$  is a unit line, the stretch of  $k'$  is given with the Pythagoras theorem by:

$$S_k = \sqrt{k_x^2 + k_y^2 + k_z^2} \quad (\text{Eq.43})$$

The rotation of  $k$ ,  $\phi_k$ , by:

$$\cos \phi_k = \frac{k_x k'_x + k_y k'_y + k_z k'_z}{S_k} \quad (\text{Eq.44})$$

$\delta$  is the angle between  $U$ , the pole of rotation of lines  $k$  and  $k'$ , and the eigenvector of  $\mathbf{F}_{ij}$  which is parallel to one of the reference axis,  $e_i$ .

$$\cos \delta = \frac{U_x e_{ix} + U_y e_{iy} + U_z e_{iz}}{\bar{U} \cdot \bar{e}_i} \quad (\text{Eq.45})$$

$U_i$  components are obtained with the cross-product of  $k$  and  $k'$ :

$$k \times k' = \det \begin{vmatrix} U_x & U_y & U_z \\ k_x & k_y & k_z \\ k'_x & k'_y & k'_z \end{vmatrix}, \text{ where}$$

$$\begin{aligned} U_x &= k_y k'_z - k_z k'_y \\ U_y &= k_z k'_x - k_x k'_z \\ U_z &= k_x k'_y - k_y k'_x \end{aligned} \quad (\text{Eq.46})$$

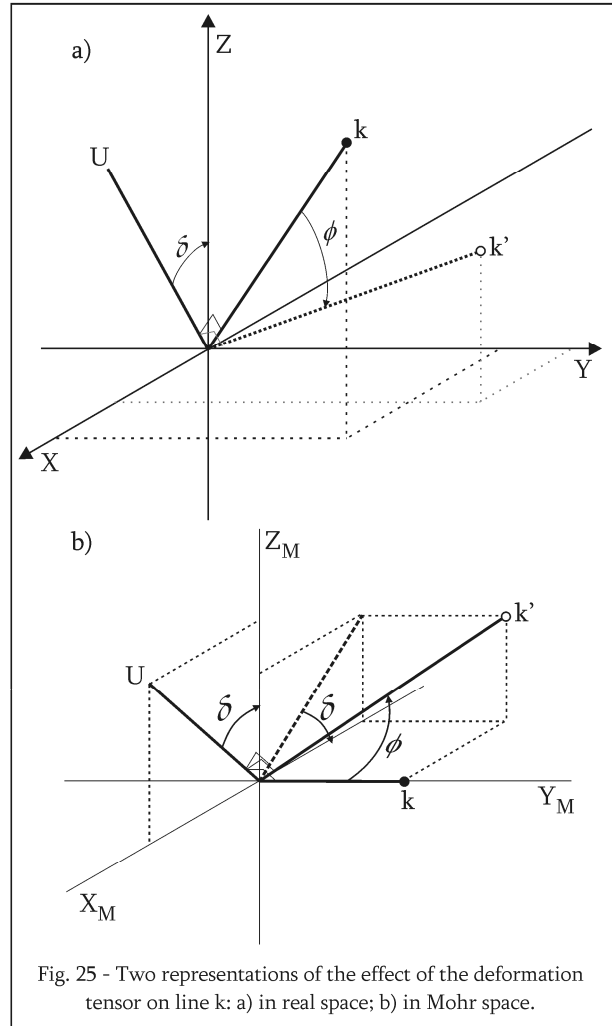


Fig. 25 - Two representations of the effect of the deformation tensor on line  $k$ : a) in real space; b) in Mohr space.

The Mohr-cyclide can now be plotted with the following polar coordinates (Fig.25b):

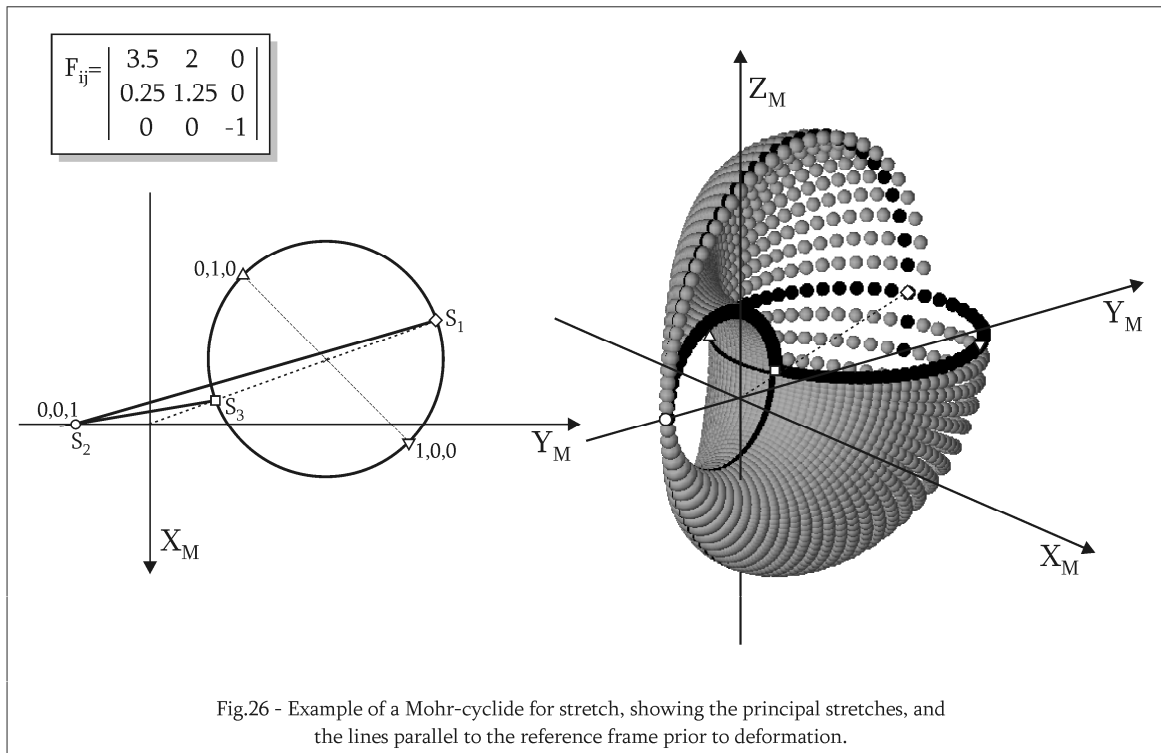
$$\begin{aligned} X_M &= S_k \cdot \sin \phi \cdot \cos \delta \\ Y_M &= S_k \cdot \cos \phi \\ Z_M &= S_k \cdot \sin \phi \cdot \sin \delta \end{aligned} \quad (\text{Eq.47})$$

Mohr-cyclides for deformation tensors can also be described with parametric equations, based on the cyclide general formulas (Eq.1 and 2). The procedure and resulting formulas are similar to what was described for monoclinic flow.

#### 4.4. Interpretation

Mohr-cyclides for monoclinic deformation, defined by  $\mathbf{F}_{ij}$  or  $\mathbf{H}_{ij}$ , are geometrically identical to Mohr-cyclides for flow, and can be interpreted in the same way, in terms of angles and special sections, noting that the undeformed coordinate axes plot with coordinates:  $\{1,0,0\} \rightarrow \{F_{21}, F_{11}, 0\}$ ;  $\{0,0,1\} \rightarrow \{0,0, F_{33}\}$ ;

$\{0,1,0\} \rightarrow \{-F_{12}, F_{22}, 0\}$  (Fig.26). There are, however, some important differences where interpretation is concerned.



The first major difference between these two types of Mohr-diagram is the use of reference axes. In flow, axes are labelled and points in the diagram can be read as Cartesian coordinates with a physical meaning (stretching rate or angular velocity). The Mohr-diagram for  $\mathbf{F}_{ij}$ , on the other hand, is defined by a calibrated coordinate system with no particular significance and can be interpreted only in terms of polar coordinates (Means 1982). Contrary to diagrams for flow, negative and positive values on the Mohr-scale have no special meaning, because what is important for interpretation is the stretch value, always calculated via Pythagoras theorem and, therefore, always positive.

The second difference is related to the ellipsoids that  $\mathbf{F}_{ij}$  and  $\mathbf{L}_{ij}$  represent. The flow tensor can be used to determine the instantaneous stretching ellipsoid and its principal axes the ISA (Fig.18), whereas  $\mathbf{F}_{ij}$  represents the finite strain ellipsoid. The principal axes of this ellipsoid are the principal stretches, the directions which observe maximum, intermediate and minimum finite stretches ( $S_1, S_2, S_3$ ). The absolute value of the principal stretches can be found with the eigenvalues of the Green tensor (Eq.38); in the Mohr-cyclide they are represented by three points (Fig.26):

a) Two of them plot in opposing ends of the diameter parallel to the line, which connects the centre of the basal circle of the cyclide to the origin of the coordinate system. This is similar to the method used to find maximum and minimum stretches in the Mohr-circle for stretch.

b) The third principal stretch plots at the eigenvalue related with the eigenvector used as a reference for the Mohr-cyclide. This coincidence is forced upon the cyclide by the assumption of a deformation with monoclinic geometry.

c) The condition  $S_1 \perp S_2 \perp S_3$  is respected since the principal stretches plot at opposite points of circular sections within the Mohr-cyclide, which can be interpreted as Mohr-circles and, therefore, obey the double angle rule.

It is important to mention that all the principal stretches may occur in any of the orientations described in a), depending of the components of  $\mathbf{F}_{ij}$ . Another relevant comment is that the points which correspond to  $S_1, S_2, S_3$  do not have any special meaning in the Mohr-cyclides for flow. However, the ISA can be represented in a Mohr-cyclide for a deformation defined by tensor  $\mathbf{F}_{ij}$ , keeping their original meaning, if steady-state deformation is assumed. The difference in interpretation between cyclides for  $\mathbf{F}_{ij}$  and  $\mathbf{L}_{ij}$  also implies that the basal section of a cyclide for deformation cannot be used to estimate flow parameters (as in Fig.17a).

$\mathbf{F}_{ij}$  is also very distinct from  $\mathbf{L}_{ij}$  in its nature as a tensor operator.  $\mathbf{L}_{ij}$ , applied to a position vector  $k$ , does not produce a second position vector, but a velocity vector, labelled above as  $\dot{d}$ . If  $\dot{d}$  is infinitesimally small, its magnitude  $d \rightarrow 0$ , which means that there is no displacement. The Mohr-cyclide for  $d \rightarrow 0$  is, thus, infinitesimally centred around the origin, as was shown for Mohr-circles by Passchier (1988). This is in sharp contrast with Mohr-cyclides for deformation.  $\mathbf{F}_{ij}$ , applied to a material line  $k$  (which can be described with a position vector), defines a new material line  $k'$ , deformed by rotation  $\phi_k$  and stretch,  $S_k$ . For the first increment of deformation, where the components of  $\mathbf{F}_{ij}$  are infinitesimally small,  $\phi_k \rightarrow 0$  and  $S_k \rightarrow 1$  (cf. Eq.32). Mohr-cyclides for incremental deformation are, thus, centred around 1.

What happens afterwards? Incremental deformation is described by  $\mathbf{F}_{ij}'$ , the incremental deformation tensor, defined as the integration of a flow tensor with respect to time:

$$F_{ij}' = \int L_{ij} dt + c \quad (\text{Eq.48})$$

where  $c$  is an integration constant that can be written as  $\mathbf{I}_{ij}$ , an identity matrix. For a flow tensor in the form of Eq.29, for instance, the result of Eq.48 yields:

$$F_{ij}' = \begin{vmatrix} s_x \Delta t + 1 & -w_z \Delta t / 2 & 0 \\ w_z \Delta t / 2 & s_y \Delta t + 1 & 0 \\ 0 & 0 & s_z \Delta t + 1 \end{vmatrix} \quad (\text{Eq.49})$$

$\Delta t$  is a time increment and tends to zero. Note that the dots above the “s” are gone, because integration transforms stretching rates along a particular axis into stretches. Finite deformation can be described as the sum of  $n$  time increments. The finite deformation tensor,  $\mathbf{F}_{ij}^*$ , is thus the result of  $n$  multiplications of  $\mathbf{F}_{ij}'$ :

$$F_{ij}^* = (F_{ij}')^n \quad (\text{Eq.50})$$

Like any other tensor, the several steps of  $\mathbf{F}_{ij}^*$  can be represented graphically with Mohr-cyclides. Figure 27 illustrates three of these steps, with  $n=1$ ,  $n=5$  and  $n=9$  for an incremental deformation tensor defined by integration of flow tensor:

$$L_{ij} = \begin{vmatrix} -2 & 0.75 & 0 \\ -0.75 & 0.25 & 0 \\ 0 & 0 & 1 \end{vmatrix}$$

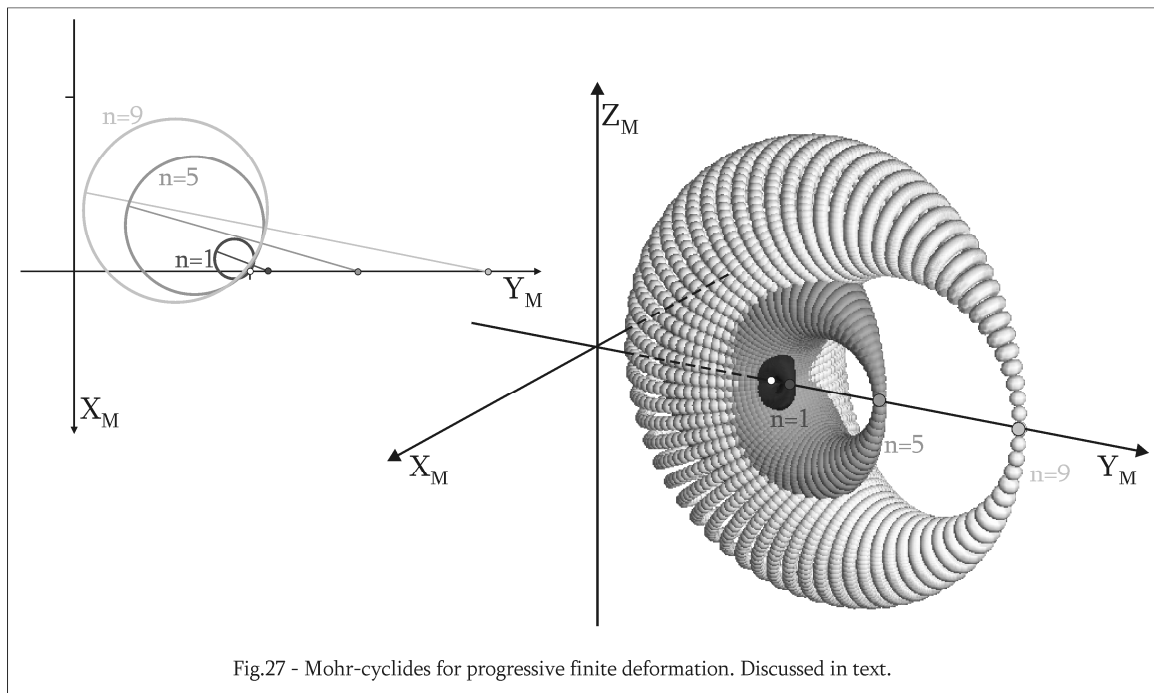


Fig.27 - Mohr-cyclides for progressive finite deformation. Discussed in text.

The figure allows the following observations:

a) The very first increment, with  $\Delta t \rightarrow 0$ , produces a cyclide so small that can be represented by a point at coordinates  $\{0,1,0\}$ . Ideally, subsequent steps should also follow the  $\Delta t \rightarrow 0$  condition, but this makes the visualisation and calculation of Mohr-cyclides quite difficult. Instead, I considered

$\Delta t = 0.1$ , which is still small enough to be considered an increment, although sufficient to produce visible changes in a reasonable amount of steps.

b) The successive Mohr-cyclides for different steps in progressive deformation keep their original geometry, which is the same as the flow tensor used to derive them. In the case of Figure 28, this geometry is a positive single-crescent cyclide.

c) As the number of steps increases, the relative size of the Mohr-cyclides also increases.

## 5. Mohr-cyclides for unspecified tensors

The previous sections of this chapter deal with the application of the concept of Mohr-cyclides to three different types of geological tensors. Mohr-space, however, is not the private feud of stress, flow and deformation. I see it as a general property of all tensors, regardless of physical meaning. This section offers a solution to build “blank” Mohr-cyclides for an unspecified tensor, with the experience assembled from geological tensors. The only necessary condition is monoclinic or higher tensor symmetry.

Any unspecified tensor  $\mathbf{T}_{ij}$  in  $\mathfrak{R}^3$  space transforms a vector  $v$  in a second vector  $v'$ , according to:

$$v'_i = T_{ij}v_j \quad (\text{Eq.51})$$

which can be expanded to:

$$\begin{cases} v'_x = T_{11}v_x + T_{12}v_y + T_{13}v_z \\ v'_y = T_{21}v_x + T_{22}v_y + T_{23}v_z \\ v'_z = T_{31}v_x + T_{32}v_y + T_{33}v_z \end{cases} \quad (\text{Eq.52})$$

Mohr-cyclides are defined by the properties of  $v'$ , namely its magnitude  $\bar{v}$  and orientation in space.  $\bar{v}$  is given by simple application of the Pythagoras theorem:

$$\bar{v} = \sqrt{v_x'^2 + v_y'^2 + v_z'^2} \quad (\text{Eq.53})$$

The orientation of  $v'$  can be defined in many ways, but for Mohr-cyclide purposes, two angles alone are necessary,  $\phi$  and  $\delta$ .  $\phi$  can be defined as the angle between  $v$  and  $v'$  and is given by the dot-product:

$$\cos\phi = \frac{v_x v'_x + v_y v'_y + v_z v'_z}{\bar{v}} \quad (\text{Eq.54})$$

The definition of  $\delta$  is less intuitive. First, a third vector,  $U$ , must be introduced as the pole of the plane defined by  $v$  and  $v'$ . The components of  $U$  can be obtained with the cross-product of  $v$  and  $v'$ :

$$v \times v' = \det \begin{vmatrix} U_x & U_y & U_z \\ v_x & v_y & v_z \\ v'_x & v'_y & v'_z \end{vmatrix}, \text{ where}$$

$$\begin{aligned} U_x &= v_y v'_z - v'_y v_z \\ U_y &= v_z v'_x - v'_z v_x \\ U_z &= v_x v'_y - v'_x v_y \end{aligned} \quad (\text{Eq.55})$$

$\delta$  will be the angle between  $U$  and  $e$ , one of the eigenvectors of  $\mathbf{T}_{ij}$ . It is possible to choose any of the eigenvectors, according to the purpose of the work. However, it *must* be an eigenvector of  $\mathbf{T}_{ij}$ , not of any other tensor defined with, by or through it, unless they are identical. Failure to respect this rule results in hilarious but otherwise useless graphs of undetermined geometrical pedigree.  $\delta$  can then be calculated with

$$\cos \delta = \frac{U_x e_x + U_y e_y + U_z e_z}{\bar{U} \cdot \bar{e}} \quad (\text{Eq.56})$$

where  $\bar{e}$  is the corresponding eigenvalue.

Subsequently, the Mohr-cyclide for  $\mathbf{T}_{ij}$  can be plotted with the following polar coordinates:

$$\begin{aligned} X_M &= \bar{v} \cdot \sin \varphi \cdot \cos \delta \\ Y_M &= \bar{v} \cdot \cos \varphi \\ Z_M &= \bar{v} \cdot \sin \varphi \cdot \sin \delta \end{aligned} \quad (\text{Eq.57})$$

Table 7 shows how these principles can be applied to the tensors studied in this chapter.

It is also possible to define parametric equations the Mohr-cyclide of an unspecified tensor. Before proceeding, it is useful to remember that this discussion is based on monoclinic tensors, characterised by at least one eigenvector parallel to one of the axes of the reference frame. This condition imposes some restrictions on the components of  $\mathbf{T}_{ij}$ , which can be written in three different ways:

$$\text{a) } T_{ij} = \begin{vmatrix} a & b & 0 \\ c & d & 0 \\ 0 & 0 & f \end{vmatrix}, \quad \text{b) } T_{ij} = \begin{vmatrix} a & 0 & b \\ 0 & f & 0 \\ c & 0 & d \end{vmatrix} \quad \text{or} \quad \text{c) } T_{ij} = \begin{vmatrix} f & 0 & 0 \\ 0 & a & b \\ 0 & c & d \end{vmatrix} \quad (\text{Eq.58})$$

Letters are preferred here, instead of the usual tensor components, because they allow a compact solution for all three cases;  $f$  is odd in the alphabetical sequence, but necessary to avoid confusion with eigenvectors. The actual parameters used to define analytical solutions depend on the kind of surface described by the tensor. Mohr-cyclide shape is predictable by an assessment of the component's relative magnitudes, especially  $f$ , which corresponds to the eigenvalue of the eigenvector  $e$  used to define  $\delta$ :

- I) For  $f > a, d$ , the surface is a *positive single-crescent cyclide*;
- II) if  $f < a, d$ , the surface is a *negative single-crescent cyclide*, and
- III) for  $a, d < f < a, d$ , the Mohr-cyclide is a *torus*.

All these three surfaces have a converging point located at  $f$  and intersect the  $Y_M$ -coordinate axis at the points given by the eigenvalues of  $T_{ij}$ .  $A, B, C, D$  and  $E$  can now be defined with the equations of Table 6. Substituting these values on the parametric equation, for any point  $(\theta, \psi)$ , produces a system analogous to Eq.2:

$$\begin{aligned}
 X_M^\circ &= \frac{B \sin \psi (C \cos \theta - D)}{A - C \cos \theta \cos \psi} \\
 Y_M^\circ &= \frac{D(C - A \cos \theta \cos \psi) + B^2 \cos \theta}{A - C \cos \theta \cos \psi} \\
 Z_M^\circ &= \frac{B \sin \theta (A - D \cos \psi)}{A - C \cos \theta \cos \psi}
 \end{aligned}
 \tag{Eq.59}$$

Table 6 – Parameters for unspecified Mohr-cyclides

Parameter	$f > a, d$	$f < a, d$	$a, d < f < a, d$
	Positive single-crescent	Negative single-crescent	Torus with converging point
$A$	$\sqrt{(E_y - f)^2 + E_x^2}$		$\frac{\sqrt{(b+c)^2 + (a-d)^2}}{4}$
$B$	$\sqrt{A^2 - C^2}$		
$C$	$\frac{\sqrt{(b+c)^2 + (a-d)^2}}{4}$		$\sqrt{(E_y - f)^2 + E_x^2}$
$D$	$C$		$A$
$E$	$E_x$	$\frac{c-b}{2}$	
	$E_y$	$\frac{a+d+2f}{4}$	

Eqs.59 define a surface of the cyclide family but not the Mohr-cyclide for  $T_{ij}$ , because some of its properties are not accounted for. It is, thus, necessary to introduce an angle  $\rho$  to address an eventual tensor asymmetry.  $\rho$  can be defined as the angle between the negative  $Y_M$  and the cyclide vertical symmetry plane and is given by:

$$\tan \rho = \frac{c-b}{a+d+2f} \text{ if } f > E_y, \text{ or}$$

$$\tan \rho = \frac{c-b}{a+d-2f} \text{ if } f < E_y \quad (\text{Eq.60})$$

The parametric Mohr-cyclide can be obtained by the multiplication of the coordinates given in Eqs.59 by the rotation tensor  $\mathbf{R}_{ij}$ :

$$\begin{aligned} X_M &= X_M^\circ \cdot \cos \rho - Y_M^\circ \cdot \sin \rho + E_x \\ Y_M &= X_M^\circ \cdot \sin \rho + Y_M^\circ \cdot \cos \rho + E_y \\ Z_M &= Z_M^\circ \end{aligned} \quad (\text{Eq.61})$$

Alternatively, Mohr-cyclides for  $\mathbf{T}_{ij}$  can be plotted with a rule similar to the scheme proposed by Means (1982). Since there are three types of component distributions in monoclinic unspecified tensors (a-c, Eq.58), it is possible to give two alternative plotting recipes for the three circles defined by three mutually orthogonal points:

$$\begin{aligned} \text{a) } & \begin{array}{|l} \{1,0,0\} : \{-c, a, 0\} \\ \{0,1,0\} : \{b, d, 0\} \\ \{0,0,1\} : \{0,0, f\} \end{array} & \begin{array}{|l} \{1,0,0\} : \{c, a, 0\} \\ \{0,1,0\} : \{-b, d, 0\} \\ \{0,0,1\} : \{0,0, f\} \end{array} \\ \text{b) } & \begin{array}{|l} \{1,0,0\} : \{c, a, 0\} \\ \{0,1,0\} : \{0, f, 0\} \\ \{0,0,1\} : \{-b, d, 0\} \end{array} & \begin{array}{|l} \{1,0,0\} : \{c, a, 0\} \\ \{0,1,0\} : \{0, f, 0\} \\ \{0,0,1\} : \{-b, d, 0\} \end{array} \\ \text{c) } & \begin{array}{|l} \{1,0,0\} : \{0, f, 0\} \\ \{0,1,0\} : \{c, a, 0\} \\ \{0,0,1\} : \{-b, d, 0\} \end{array} & \begin{array}{|l} \{1,0,0\} : \{0, f, 0\} \\ \{0,1,0\} : \{c, a, 0\} \\ \{0,0,1\} : \{-b, d, 0\} \end{array} \end{aligned} \quad (\text{Eq.62})$$

The following applies to this plotting method:

1) for parametric equation purposes, only the circle defined by the diameter  $\{-c, a, 0\}$ - $\{b, d, 0\}$  (or  $\{c, a, 0\}$ - $\{-b, d, 0\}$ ), is a principal circle of the cyclide;

2) the two columns for each a-c case of Eq.62 represent plotting schemes for, respectively, Mohr-cyclides of the *first kind* and Mohr-cyclides of the *second kind* (cf. De Paor and Means 1984).

## 5.1. Proof

Means (1983) suggested that orthogonal lines in real space always plot as diameters of a Mohr-circle, irrespective of the components chosen to define the same tensor. In other words, considering the tensor rotation formula,

$$T'_{ij} = R_{ij} \cdot T_{ij} \cdot R_{ij}^T \quad (\text{Eq.28})$$

the Mohr-circle for  $\mathbf{T}'_{ij}$  will be the same as for  $\mathbf{T}_{ij}$ , whichever angle  $\theta$  is applied in the rotation tensor  $\mathbf{R}_{ij}$ .

Take, for instance, a tensor of the form:

$$T_{ij} = \begin{vmatrix} a & b & 0 \\ c & d & 0 \\ 0 & 0 & f \end{vmatrix}$$

Lines parallel to the  $xx$ - and  $yy$ -reference axis in the geographical space plot as described in Eq.62a (second kind) and give a circle P, defined by a centre  $Ctr$  and a diameter  $D$ :

$$Ctr_P \begin{cases} x: \frac{c-b}{2} \\ y: \frac{a+d}{2} \\ z: 0 \end{cases} \quad (\text{Eq.63})$$

$$D^2_P = (a-d)^2 + (b+c)^2 \quad (\text{Eq.64})$$

From Eq.28, we obtain alternative components for  $\mathbf{T}_{ij}$ ,

$$\begin{aligned} a' &= a \cos^2 \theta + (b+c) \cos \theta \sin \theta + d \sin^2 \theta \\ b' &= b \cos^2 \theta + (d-a) \cos \theta \sin \theta - c \sin^2 \theta \\ c' &= c \cos^2 \theta + (d-a) \cos \theta \sin \theta - b \sin^2 \theta \\ d' &= d \cos^2 \theta - (b+c) \cos \theta \sin \theta + a \sin^2 \theta \\ f' &= f \end{aligned} \quad (\text{Eq.65})$$

which define an alternative circle P'. Substituting Eqs.65 in Eqs.63, the centre of circle P' is given by:

$$Ctr_{P'} \begin{cases} x: \frac{c(\cos^2 \theta + \sin^2 \theta) - b(\cos^2 \theta + \sin^2 \theta)}{2} \\ y: \frac{a(\cos^2 \theta + \sin^2 \theta) + d(\cos^2 \theta + \sin^2 \theta)}{2} \\ z: 0 \end{cases} \quad (\text{Eq.66})$$

With the fundamental rule of trigonometry it is clear that Eqs.63 and Eq.66 are identical. The diameter of circle P', after substitution of Eq.65 on Eq.64 and rather extensive use of the associative property of multiplications, can be written as:

$$D^2_{P'} = (a - d)^2 (\cos^2 \theta + \sin^2 \theta)^2 + (b + c)^2 (\cos^2 \theta + \sin^2 \theta)^2 \quad (\text{Eq.67})$$

which is equal to the unprimed diameter (Eq.64). Thus, it is safe to say that circles P and P' are one and the same, with equal diameter and centre coordinates, and that both represent a Mohr-circle.

The general proof for circles described above confirms that the basal circle in a Mohr-cyclide (eg Fig.17a) is a Mohr-circle, but cannot be applied to the whole surface, because the cyclide geometry is more complex than a circle. To prove that a cyclide can be interpreted as a Mohr-diagram, it is necessary to recall an important property: the cyclide shape is defined by its parameters  $A, B, C, D$  (Shene, 2000), as well as parameter  $E$  and angle  $\rho$  (this work). With this in mind, I can now expand Means' proof for cyclides: *A cyclide will be a Mohr-diagram for  $T_{ij}$  if and only if its parameters  $A, B, C, D, E$  and  $\rho$  remain constant whatever combination of components is chosen from the infinite possibilities available to define  $T_{ij}$* , which is equivalent to say that, *the Mohr-cyclide for  $T_{ij}$  is identical to the Mohr-cyclide for  $T'_{ij}$* .

For  $f > a, d$ , the cyclide parameters are given by the following formulas (Table 6):

$$A = \sqrt{(E_y - f)^2 + E_x^2} \quad (\text{Eq.68})$$

$$B = \sqrt{A^2 - C^2} \quad (\text{Eq.69})$$

$$C = \frac{\sqrt{(b+c)^2 + (a-d)^2}}{4} \quad (\text{Eq.70})$$

$$D = C \quad (\text{Eq.71})$$

$$E \begin{cases} E_x = \frac{c-b}{2} \\ E_y = \frac{a+d+2f}{4} \end{cases} \quad (\text{Eq.72})$$

$$\tan \rho = \frac{c-b}{a+d+2f} \quad \text{or} \quad \tan \rho = \frac{c-b}{a+d-2f} \quad (\text{Eq.73})$$

From this list, it is clear that only four parameters,  $A, C, E$  and  $\rho$ , are independent and necessary to prove the condition.

I) *Parameter C*. Simple inspection of Eq.70 shows that  $4C$  is given by an equation identical to the diameter of a circle (Eq.64). Substituting Eq.65 in Eq.70 yields a result identical to Eq.67 and, thus:

$$4C = 4C'$$

II) *Parameter E*. Substituting Eq.65 in Eq.72 gives:

$$E \begin{cases} E_x = \frac{c(\cos^2 \theta + \sin^2 \theta) - b(\cos^2 \theta + \sin^2 \theta)}{2} \\ E_y = \frac{a(\cos^2 \theta + \sin^2 \theta) + d(\cos^2 \theta + \sin^2 \theta) + 2f}{4} \end{cases} \quad (\text{Eq.74})$$

Thus,  $E=E'$

III) *Parameter A*. From II) and Equation U18, and taking into account that  $f = f'$  (Eq.65), it is clear that  $A=A'$ .

IV) *Angle  $\rho$* . Substituting Eq.65 in Eq.60 yields:

$$\tan \rho' = \frac{c(\cos^2 \theta + \sin^2 \theta) - b(\cos^2 \theta + \sin^2 \theta)}{a(\cos^2 \theta + \sin^2 \theta) + d(\cos^2 \theta + \sin^2 \theta) + 2f} \quad \text{or}$$

$$\tan \rho' = \frac{c(\cos^2 \theta + \sin^2 \theta) - b(\cos^2 \theta + \sin^2 \theta)}{a(\cos^2 \theta + \sin^2 \theta) + d(\cos^2 \theta + \sin^2 \theta) - 2f} \quad (\text{Eq.75})$$

And, therefore,  $\rho=\rho'$ .

From I) to IV), it is possible to conclude that the cyclide parameters are independent from any rotation applied to  $\mathbf{T}_{ij}$ . Thus, the cyclide remains the same whether defined by  $\mathbf{T}_{ij}$  or  $\mathbf{T}'_{ij}$  and can be interpreted as a Mohr-diagram. This is also consistent with the definition of a tensor as a mathematical entity independent of reference frame.

## 6. Summary

**a)** The graphical representation of second-rank tensors in three-dimensional Mohr-space are surfaces from the cyclides family, just as Mohr-circles for second-rank tensors in 2D.

**b)** The geometry of Mohr-cyclides is independent of reference frame and, therefore, these surfaces can be interpreted as Mohr diagrams.

**c)** For any  $\mathbf{T}_{ij}$  tensor, it is possible to define the same Mohr-cyclide from two independent approaches: analytical polar coordinates (Table 7) or via parametric equations.

**d)** Mohr-cyclides are defined with respect to  $e_i$ , one of the eigenvectors of  $\mathbf{T}_{ij}$ ; the relative magnitude of its eigenvalue defines the general shape of the surface, all of them with a converging point at  $e_i$ : i)  $e_i > e_j, e_k$  - positive single-crescent cyclide; ii)  $e_i < e_j, e_k$  - negative single-crescent cyclide; iii)  $e_j, e_k > e_i > e_j, e_k$  - torus with a converging point.

e) The  $X_M, Y_M, Z_M$  axes in 3D Mohr-space are interpreted as:  $\tau_{(\sigma^1)}$ ,  $\sigma_n$ ,  $\tau_{(\perp\sigma^1)}$ , for stress; and  $\dot{\omega}_{(\perp\mathbf{w})}$ ,  $\dot{s}$ ,  $\dot{\omega}_{(\mathbf{w})}$ , for flow. In the case of deformation, axes are calibrated but not specified.

f) A Mohr-cyclide is a collection of Mohr-circles, corresponding to different orientations in space that may define a plane.

Table 7 – Summary of the parameters used for determining polar coordinates of a cyclide for stress, flow or deformation. Symbols as in Table 1.

$\mathbf{T}_{ij}$	$\mathbf{S}_{ij}$	$\mathbf{L}_{ij}$	$\mathbf{F}_{ij}$
Effect of $\mathbf{T}_{ij}$	$\sigma_p = S_{ij} N_p$	$v_i = L_{ij} \vec{m}$	$k' = F_{ij} \cdot k$
$\bar{v}$	$\sigma$	$\bar{d}$	$S_k$
$\mathbf{U}$	$N_s$ (pole of $\sigma - \sigma_n$ )	$\mathbf{U}$ (pole of $\dot{d} - \vec{m}$ )	$\mathbf{U}$ (pole of $k - k'$ )
$e$	$\sigma_1$ (or $\sigma_2, \sigma_3$ )	$\vec{w}$	$e$
$\phi$	$\sigma \wedge \sigma_n$	$\dot{d} \wedge \vec{m}$	$\phi = k \wedge k'$
$\delta$	$N_s \wedge \sigma_1$ (or $\sigma_2, \sigma_3$ )	$\mathbf{U} \wedge \vec{w}$	$\mathbf{U} \wedge e$
Figure	Fig.4	Fig.14	Fig.25

## 7. Future work

*Time exists  
just on your wrist,  
so don't panic.*  
Travis

This work does not drain the topic of Mohr-cyclides, an endeavour way beyond a reasonable deadline for this dissertation. Some of the topics left behind offer interesting leads on how to proceed the idea of Mohr-cyclides further.

One of the most useful properties of Mohr-diagrams is the existence of a *pole*, a point in Mohr-circles which relates all other points to their real orientation in geographical space (Allison 1984). Finding a pole in the Mohr-cyclide would be extremely useful, especially in the case of stress, because it would allow an immediate correlation between a fault plane and possible slip directions.

The general form of a tensor  $\mathbf{T}_{ij}$  has nine different components and its eigenvectors (which can have three, two or one real eigenvalues) are not necessarily parallel to the reference frame – ie, the tensor has *triclinic symmetry*. Mohr-cyclides for triclinic tensors are particularly elusive and defy all attempts to breach their walls. Despite multiple efforts during my work, I was never able to find a satisfying solution for this problem. Some preliminary results, however, allow me to make some educated guesses about their general shape and properties:

a) Triclinic Mohr-cyclides are not symmetric with respect to the  $X_M Y_M$ -plane, as the diagrams for higher symmetry tensors. This is in good agreement with their low symmetry and means that, probably, they cannot be defined by simple polar coordinates as described for other tensors in this work.

b) Unfortunately, the ever popular and user friendly plotting scheme defined by Means (1982), does not work in this case, whichever sensible combinations of sign-change and coordinate inversion.

c) Triclinic Mohr-cyclides are defined, as expected, by the more complex surfaces in the cyclide family, namely double-crescent and double-singularity spindle cyclides (Table 2). This means that the Mohr-diagrams will have two converging points. In monoclinic cyclides, the single converging point corresponds to the eigenvector which is parallel to the reference frame (and for flow tensors, to the vorticity vector). In triclinic cyclides, one of the converging points is the eigenvector used as reference; the meaning of the other converging point is obscure. For triclinic flow tensors, it is probably the vorticity vector itself.

## References

- Allen, S., Dutta, D., 1997. Cyclides in pure blending I. *Computer Aided Geometric Design* 14, 51-75
- Allison, I., 1984. The pole of the Mohr circle. *Journal of Structural Geology* 6, 331-333.
- Angelier, J. 1979. Determination of the mean principal directions of stresses for a given fault population. *Tectonophysics* 56, T17-T26
- Brace, W.F., 1961. Mohr construction in the analysis of large geological strain. *Bull. Geol. Soc. Am.* 71, 1059-1080.
- Bobyarchick, A.R., 1986. The eigenvalues of steady state flow in Mohr space. *Tectonophysics* 122, 35-51.
- Cuttler, J., Elliott, D., 1983. The compatibility equations and the pole to the Mohr circle. *Journal of Structural Geology* 5, 287-297.
- Delaney, P.T., Pollard, D.D., Zioney, J.I., MacKee, E.H., 1986. Field relations between dikes and joints: Emplacement processes and paleostress analysis. *Journal of Geophysical Research* 91, 4920-4938.
- De Paor, D.G., Means, W.D., 1984. Mohr circles of the First and Second Kind and their use to represent tensor operations. *Journal of Structural Geology* 6, 693-701.
- Dupin, C. P., 1822. *Application de Géométrie et de Mécanique à la Marine, aux Ponts et Chaussées, etc.* Bachelier, Paris.
- Drucker, D.C., 1967. *Introduction to the Mechanics of Deformable Solids.* Mc-Graw-Hill. New York.
- Etchecopar, A., Vasseur, G., Daignieres, M., 1981. An inverse problem in microtectonics for the determination of stress tensors from fault striation analysis. *Journal of Structural Geology* 3, 51-65
- Iacopini, D., Passchier, C.W., Caruso, E., Köhn, D., 2007. Fabric attractors in triclinic flow systems and their application to high strain shear zones: A dynamical system approach. *Journal of Structural Geology* 29, 298-317
- Jolly, R.J.H., Sanderson, D.J., 1997. A Mohr circle construction for the opening of a pre-existing fracture. *Journal of Structural Geology* 19, 887-892.
- Lin, S., Jiang, D., Williams, P.F., 1998. Transpression (or transtension) zones of triclinic symmetry: natural example and theoretical modelling. In: Holdsworth, R.E., Strachan, R.A., Dewey, J.F. (Eds.), *Continental Transpressional and Transtensional Tectonics.* Geological Society of London, Special Publication 135, 41-57.
- Lisle, R.J., 1979. The representation and calculation of the deviatoric component of the geological stress tensor. *Journal of Structural Geology* 1, 317-321.
- Lisle, R.J., Ragan, D.M., 1988. Strain from three stretches – a simple Mohr circle solution. *Journal of Structural Geology* 10, 905-906.
- Lister, G.S., Williams, P.F., 1983. The partitioning of deformation in flowing rock masses. *Tectonophysics* 92, 1-33.
- Means, W.D., 1982. An unfamiliar Mohr circle construction for finite strain. *Tectonophysics*. 89, T1-T6.
- Means, W.D., 1983. Application of the Mohr-circle construction to problems of inhomogeneous deformation. *Journal of Structural Geology* 5, 279-286.
- Means, W.D. 1992. How to do anything with Mohr circles (except fry an egg). Unpublished manual of the short course presented at the Geological Society of America Meeting in Cincinnati, Ohio (October 1992).

- Mohr, O., 1882. Über die Darstellung des Spannungszustandes und des Deformation-zustandes eines Körperelementes und über die Anwendung derselben in der Festigkeit-slehre. *Civilingenieur* 28, 113-115.
- Nadai, A., 1950. *Theory of Flow and Fracture of Solids*. McGraw-Hill. New York.
- Passchier, C.W., Urai, J.L., 1988. Vorticity and strain analysis using Mohr diagrams. *Journal of Structural Geology* 10, 755-763.
- Passchier, C.W., 1986. Flow in natural shear zones – the consequences of spinning flow regimes. *Earth and Planetary Science Letters* 77, 70-80.
- Passchier, C.W., 1987. Efficient use of the velocity gradient tensor in flow modelling. *Tectonophysics* 136, 159-163.
- Passchier, C.W., 1988. The use of Mohr circles to describe non-coaxial progressive deformation. *Tectonophysics* 149, 323-338.
- Passchier, C.W. 1990a. A Mohr circle construction to plot the stretch of material lines. *Journal of Structural Geology* 12, 513-515.
- Passchier, C.W. 1990b. Reconstruction of deformation and flow parameters from deformed vein sets. *Tectonophysics* 180, 185-199.
- Passchier, C.W., 1991. The classification of dilatant flow types. *Journal of Structural Geology* 13, 101-104.
- Passchier, C.W., 1993. The sliding-scale Mohr diagram. *Tectonophysics* 218, 367-373.
- Pratt, M.J., 1990. Cyclides in computer aided geometric design, *Computer Aided Geometric Design* 7, 221-242.
- Ragan, D., 1973. *Structural Geology: An Introduction to Geometric Techniques*. Wiley, New York.
- Ramberg, H., 1975. Particle paths, displacement and progressive strain applicable to rocks. *Tectonophysics* 28, 1-37.
- Ramsay, J.G., 1967. *Folding and Fracturing of Rocks*. McGraw-Hill. New York.
- Ramsay, J.G., Huber, M.I., 1983. *The Techniques of Modern Structural Geology - Volume 1: Strain Analysis*. Academic Press.
- Ramsay, J.G., Lisle, R.J., 2000. *The Techniques of Modern Structural Geology - Volume 3: Applications of continuum mechanics in structural geology*. Academic Press.
- Robin, P.-Y., Cruden, A.R. 1994. Strain and vorticity patterns in ideally ductile transpression zones. *Journal of Structural Geology* 16, 447-466.
- Sanderson, D.J., Marchini, W.R.D., 1984. Transpression. *Journal of Structural Geology* 6, 449-458.
- Shene, C.-K., 2000. Do blending and offsetting commute for Dupin cyclides? *Computer Aided Geometric Design* 17, 891-910.
- Simpson, C., De Paor, D.G., 1993. Strain and kinematic analysis in general shear zones. *Journal of Structural Geology* 15, 1-20.
- Spencer, A.J.M., 1980. *Continuum Mechanics*. Longman. London and New York.
- Treagus, S.H., 1983. A theory of finite strain variation through contrasting layers, and its bearing on cleavage refraction. *Journal of Structural Geology* 5, 351-368.
- Treagus, S.H., 1986. Some applications of the Mohr diagram for three-dimensional strain. *Journal of Structural Geology* 8, 819-830.

- Treagus, S.H., 1990. The Mohr diagram for three-dimensional reciprocal stretch vs. rotation. *Journal of Structural Geology* 12, 383-395.
- Truesdell, C., 1954. *The Kinematics of Vorticity*. Indiana University Press.
- Vissers, R.L.M., 1994. Finite strain in simple shear, inspected with Mohr circles for stretch. *Journal of Structural Geology* 16, 1723-1726.
- Wallis, S.R., 1992. Vorticity analysis in a metachert from the Sambagawa Belt, SW Japan. *Journal of Structural Geology* 14, 271-280.
- Zhang, J., Zheng, Y., 1997. Polar Mohr constructions for strain analysis in general shear zones. *Journal of Structural Geology* 19, 745-748.

# Lebenslauf

---

August 24<sup>th</sup> 1976 – Born in Lisboa, Portugal

1982-1986 – Escola Primária A Voz do Operário (Gründschule)

1986-1988 – Escola Preparatória Marquesa de Alorna

1988-1994 – Liceu Maria Amália Vaz de Carvalho (Gymnasium)

1994-1999 – Undergraduate student at the Departamento de Geologia, Universidade de Lisboa

– Graduated in July 1999

2000-2002 – MSc. student at the Departamento de Geologia, Universidade de Lisboa

– MSc. defended in July 2002

2003-2007 – Ph.D. student at the Institut für Geowissenschaften, Johannes-Gutenberg-Universität,  
Mainz